DISSERTATION

THE RESPONSE OF A SPHERICAL TISSUE-EQUIVALENT PROPORTIONAL COUNTER TO IRON PARTICLES FROM 200-1000 MEV/NUCLEON

Submitted by

Brad B. Gersey

Department of Environmental and Radiological Health Sciences

In partial fulfillment of the requirements
For the Degree of Doctor of Philosophy
Colorado State University
Fort Collins, Colorado
Fall 2006

COLORADO STATE UNIVERSITY

October 20, 2006

WE HEREBY RECOMMEND THAT THE DISSERTATION PREPARED UNDER OUR SUPERVISION BY BRAD B. GERSEY ENTITILED *THE RESPONSE OF A SPHERICAL TISSUE-EQUIVALENT PROPORTIONAL COUNTER TO IRON PARTICLES FROM 200-1000 MEV/NUCLEON* BE ACCEPTED AS FULFILLING IN PART REQUIREMENTS FOR THE DEGREE OF DOCTOR OF PHILOSOPHY.

Committee on Graduate Work

(Please print name under signature)

Eleanor A. Blakely
ELEANOR A. BLAKELY

John L Hartou
JOHN L HARTOU

John D. Zimbrick
JOHN D. ZIMBRICK

Thomas B Borak
Advisor THOMAS B BORAK

John D. Zimbrick
Department Head/Director

ABSTRACT OF DISSERTATION

THE RESPONSE OF A SPHERICAL TISSUE-EQUIVALENT PROPORTIONAL COUNTER TO IRON PARTICLES FROM 200-1000 MEV/NUCLEON

The radiation environment aboard the space shuttle and the International Space Station includes high-Z and high-energy (HZE) particles that are part of the galactic cosmic radiation (GCR) spectrum. The ^{56}Fe ion is considered to be one of the most biologically important parts of the GCR spectrum. Tissue-equivalent proportional counters (TEPC) are used as active dosimeters on manned space flights. These TEPC's are further used to determine average quality factor for each space mission. A TEPC simulating a 1-μm diameter sphere of tissue was exposed as part of a particle spectrometer to ^{56}Fe at energies from 200-1000 MeV/nucleon. The response of TEPC in terms of mean lineal energy $\overline{y}_F$, and dose mean lineal energy, $\overline{y}_D$, as well as energy deposited at different impact parameters through detector was determined for six different incident energies of ^{56}Fe in this energy range. Calculations determined that charged particle equilibrium was achieved for each of the six experiments. Energy depositions at different impact parameters were calculated using the spatially restricted LET model, a radial dose distribution model. Energy deposition at one impact parameter (0-mm) was calculated with a track structure

model code called BTC4. Results from these three model calculations were compared to experimental data.

Brad B. Gersey
Environmental and Radiological
Health Sciences Department
Colorado State University
Fort Collins, CO 80523
Fall 2006

TABLE OF CONTENTS

ABSTACT OF DISSERTATION iii

TABLE OF CONTENTS v

CHAPTER I - INTRODUCTION 1

CHAPTER II - REVIEW OF LITERATURE 4
- Space Radiation Environment 4
  - I Trapped Particle Radiation 4
  - II Solar Particle Radiation 6
  - III Galactic Cosmic Radiation 7
- Radiological Risks of GCR 9
- Space Radiation Exposure for Different Mission Scenerios 12
  - I Low Earth Orbit 12
  - II Geostationary Orbit 13
  - III Mission to Mars 13
- Radiation Protection Standards for Astronauts 14
- Radiation Shielding 16
- Radiation Dosimetry 18
  - I Passive Dosimetry 18
  - II Active Dosimetry 19
- Modeling of Radiation Transport 21
  - I Large Scale Modeling 21
  - II Small Scale Modeling 21
- Experiments Characterizing Dosimetry Devices 23
- Contributions from This Work 28

CHAPTER III – MATERIALS AND METHODS 30

CHAPTER IV – RESULTS 44
- Experimental Results 44
- Modeling Results 55

CHAPTER V – DISCUSSION 63
- Particle Events with Impact Parameter Equal to 0-mm 63
  - I Radial Dose Model 63
  - II Spatially Restricted LET Equation 65
  - III BTC4 Code 67
- Particle Events at All Impact Parameters 69
  - I Distribution of TEPC Energy Response 69
  - II Explanation of TEPC Energy Response Distribution Anomalies 72
  - III Absorbed Dose Determination 76
  - IV Average Values of TEPC Energy Deposition

Response Functions 77
V Quality Factor Determination 79
CHAPTER VI – CONCLUSIONS 81
REFERENCES 84
APPENDICES 89
Appendix A Health Physics and Microdosimetry Terminology ... 89
Appendix B Spatially Restricted LET Equation 100
Appendix C Radial Dose Model 107
Appendix D BTC4 Model 113
BTC4 Model Assumptions 114
Models Used in BTC4 Model 116
I Rudd Model 116
II Secondary Electron Angular Ejection Distribution Model 118
III Electron Energy Deposition Model 119
Appendix E Beam Normalization and Determination of Charged Particle Equilibrium (CPE) in TEPC 121
Beam Normalization 121
Charged Particle Equilibrium Determination . 123
I Utilization of the Response Function for the Spherical TEPC to Calculate Absorbed Dose 123
II Utilization of the Assumption of CPE in the TEPC to Calculate Absorbed Dose 123
III Formula to Calculate Λ 124
Appendix F Timing and Signal Pathway 128
Appendix G Response Functions of TEPC 134

CHAPTER I - INTRODUCTION

It has been estimated that during a three-year mission to Mars, an astronaut would receive a radiation dose equivalent of 1 Sv (NCRP, 1989). During space travel outside of the geomagnetosphere, the main source of chronic radiation exposure is from galactic cosmic radiation (GCR). Approximately 87% of the particles in the GCR spectrum are protons, 12% are helium nuclei and 1% are particles heavier than helium, often referred to as high-Z and high-energy (HZE) particles. The heaviest biologically important of these HZE particles is iron because of its relatively large contribution to radiation dose and its high LET (NCRP, 1989; NCRP, 2000).

Currently, tissue equivalent proportional counters (TEPC) are flown aboard the Space Shuttle and International Space Station as area monitors to characterize the radiation field inside the spacecraft (Badhwar et al., 1997; Badhwar et al. 1994a; Badhwar et al., 1992). Energy deposition spectra produced by a TEPC can be used to calculate absorbed dose and estimate the average quality of radiation during the mission (Badhwar et al.,1992). In the past, it has been assumed that lineal energy, y, is numerically equivalent to LET. The measured distribution f(y) was assumed to be a direct measurement of the LET distribution, f(L), of the incident particles (Badhwar et al., 1994b; Badhwar et al., 1996). However, recent comparisons of measurements

of f(y) with a TEPC and f(L) using a particle spectrometer indicate that there are significant differences between the two distribution (Doke et al., 2001). This can cause large uncertainties in the corresponding estimates of quality factor. The objective of this work was to carefully measure the response of a TEPC to ^{56}Fe particles for a range of energies across the peak of the GCR fluence vs. energy spectrum.

Previous measurements of TEPC response have used particle accelerators to produce HZE radiation of energies similar to those found in the GCR spectrum. An experiment performed by Rademacher et al. used a solid walled 12.7-mm diameter TEPC that was exposed to 1.05 GeV/ nucleon ^{56}Fe particles (Rademacher et al., 1998). The detector response as a function of impact parameter was measured using two X-Y pairs of PSDs (one upstream and one downstream of the TEPC).

In the present series of experiments, data were obtained at ground based accelerator facilities that produced beams of ^{56}Fe with kinetic energies between 200 and 1000 MeV/nucleon ($\beta = v/c = 0.56 - 0.88$). Specifically, a spherical TEPC was exposed to ^{56}Fe beams at energies spanning the peak of the GCR Fe spectrum. In each case a particle spectrometer measured the charge and position of each incident particle both upstream and downstream of the TEPC. With this experimental arrangement, the trajectory of the particle through the TEPC could be reconstructed and related to the energy deposition recorded by the detector. Frequency distributions of energy deposition (i.e., response functions) were determined for uniformly incident beams of Fe, and these distributions were used to compute absorbed dose as well as average values of lineal energy, y.

To better understand the mechanisms of energy deposition by ^{56}Fe particles in the TEPC, track structure modeling calculations were performed. A radial dose distribution model was used to calculate energy deposition of ^{56}Fe particles traversing different chordlengths through the TEPC active volume. A spatially restricted LET equation was applied to calculate energy deposition of ^{56}Fe particles for these same chordlengths through the TEPC, and further used to construct a calculated response function of the TEPC. To model energy deposition by high energy heavy ions in the TEPC for the restricted case where the particle traverses the entire diameter of the TEPC, three track structure models were used in a computer code named BTC4.

CHAPTER II – REVIEW OF THE LITERATURE

Space Radiation Environment

The radiation environment in space is a complex mix of many different types of ionizing and nonionizing radiation. The space radiation environment can be resolved into three broad categories (NCRP, 1989; NCRP 2000). These categories are: trapped particle radiation, solar particle radiation and galactic cosmic radiation (GCR)

I. Trapped Particle Radiation

Trapped particle radiation refers to charged particles (predominantly protons and electrons) that are trapped in paths that follow the earth's magnetic field lines. Trapped particle radiation can be divided into two regions (Fig. 2-1).

The first is the inner belt region, which is composed primarily of protons with energies ranging from 0.3 MeV to 500 MeV. This inner belt region extends to approximately 17,800 km above the surface of the Earth as measured at the equator. The radiation in the inner belt is an important contributor to absorbed dose for

astronauts in low earth orbit (LEO). Absorbed dose, D, is the quotient of $d\bar{\varepsilon}$ by dm, where $d\bar{\varepsilon}$ is the mean energy imparted by ionizing radiation to matter of mass dm (ICRU, 1993). The name for the unit of absorbed dose is gray (Gy).

$$D = \frac{d\bar{\varepsilon}}{dm} \qquad \text{Unit: J kg}^{-1} \qquad \text{Equation 2.1}$$

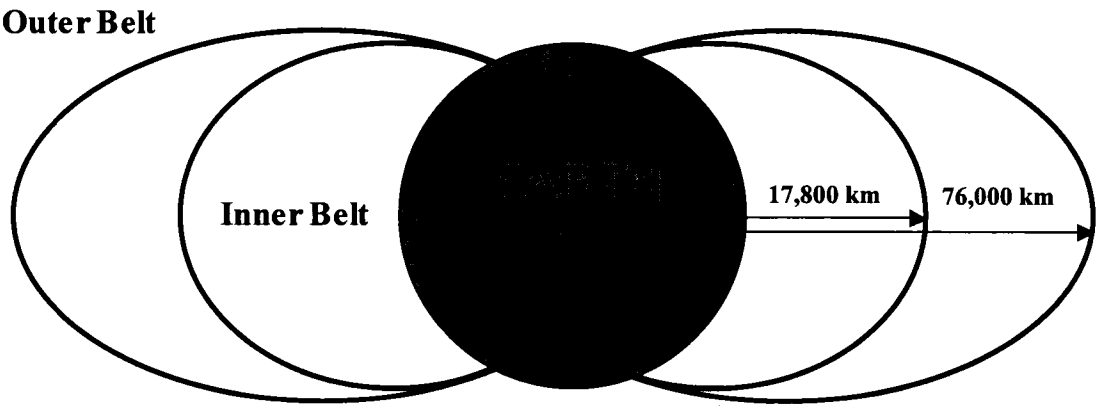

Figure 2-1. Diagram representing the Earth surrounded by magnetic field lines of the inner and outer radiation belts.

A specific area of the inner belt called the South Atlantic Anomaly (SAA) is the largest contributor to the absorbed dose for astronauts when the orbital trajectory of the spacecraft passes through it. The SAA is not an actual anomaly of the inner belt; it is merely a region where the inner belt dips to an altitude that is low enough that space craft in LEO intersect the magnetic field lines. The SAA results from the

fact that the poles of the Earth's magnetic field lines are off axis from the geographical poles.

The second is the outer belt region, which is composed primarily of electrons. The outer belt extends from approximately 17,800 km to 76,000 km above the earth at the equator. Electron energies in the outer belt region are less than 7 MeV.

II. Solar Particle Radiation

Solar particle radiation is a mixture of protons, alpha particles, and heavier elements that originate in our sun. It has historically been assumed that these particles were produced from the sun during solar flares (NCRP, 1989). The flares that produce solar particle radiation are called solar particle events (SPE). Solar particle events vary greatly in particle fluence and duration. Fluence (Φ) is defined as the quotient of dN by da, where dN is the number of particles incident on a sphere of cross-sectional area da (ICRU, 1993).

$$\Phi = \frac{dN}{da} \qquad \text{Units: } cm^{-2} \qquad \text{Equation 2.2}$$

Anomalously large SPEs may produce proton fluences on the order of $1E10^{10}$ cm^{-2} as measured in the region of the Earth's distance from the Sun and during a time period of several days. Ordinary SPEs produce proton fluences that are much lower. It has been estimated that the total fluence from all ordinary SPE during a 90-day

mission would be equivalent to 3% of the fluence of an anomalously large SPE (NCRP, 1989). New evidence suggests that only 50% of solar particle radiation present at the distance of the earth's orbit from the sun is produced in this manner. The remainder of solar particle radiation is formed by the acceleration of particles by the shocks formed from coronal mass ejections (NCRP, 2000; Rust, 1982).

III. Galactic Cosmic Radiation

Galactic cosmic radiation (GCR) is the third type of radiation. GCR originates outside of our solar system (Badhwar, 1997), and it isotropically incident upon our solar system. The exact origins of GCR are unknown at the present time. GCR is composed primarily of protons (85.3%) and helium (11.8%) with a small fraction of GCR being made up of electrons and positrons (2.0%) and elements heavier than helium (0.9%). The fractional abundances of the protons, helium and heavier elements are shown in Figure 2-2. The GCR spectrum is similar to the SPE spectrum except that GCR includes a larger fraction of elements higher in atomic number (Z) than helium, and these elements are higher in energy. The fluence rate of GCR is greatest in the energy range between 100 MeV per nucleon and 10 GeV per nucleon. High-energy charged particles with an atomic number greater than 2 are referred to as high-Z, high-energy (HZE) particles.

Although elements as heavy as uranium are found in the GCR spectrum, the fractional abundances of elements heavier than Fe are orders of magnitude diminished and are not shown in Figure 2-2.

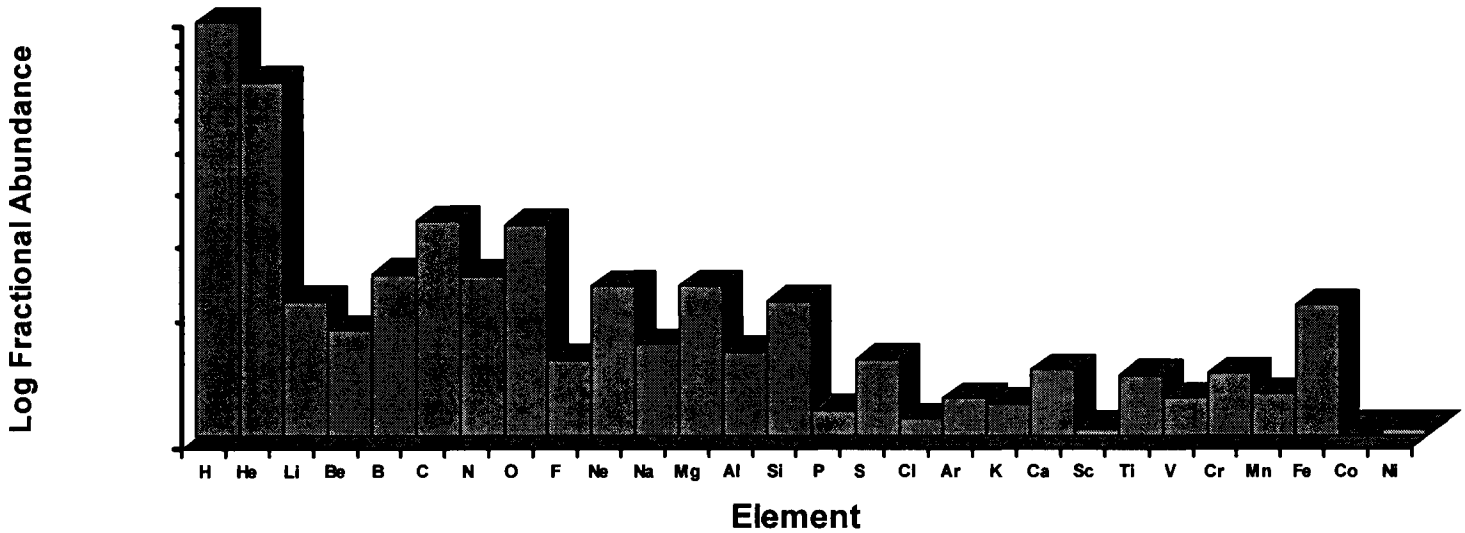

Figure 2-2. The fractional abundance of elements present in the galactic cosmic radiation spectrum.

Elements heavier than helium make up less than 1% of the GCR spectrum (Figure 2-3), but this does not mean that the heavy elements are an unimportant portion of the GCR spectrum from a radiation protection point of view.

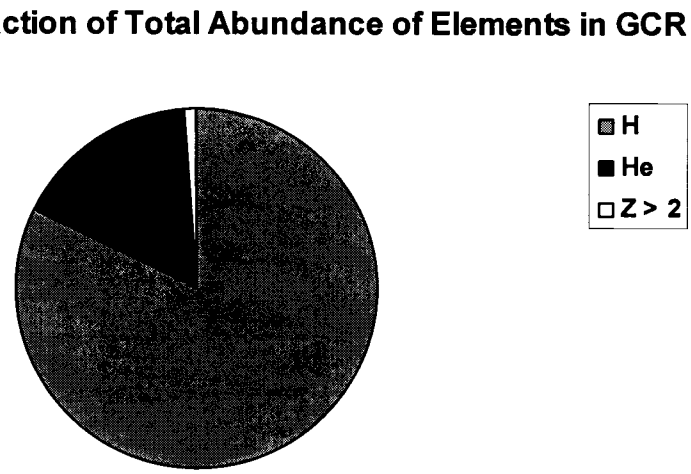

Figure 2-3. Pie chart showing fraction of total abundance of elements hydrogen, helium, and addition of all elements higher in Z than helium in the GCR spectrum.

Radiological Risk of GCR

When the fractional abundance of elements with Z greater than two are considered in terms of the radiological risk of human exposure to these particles, the relative importance of these categories is different. The dose from charged particles is related to the linear energy transfer (LET) of the particles (Turner, 1992). LET or unrestricted stopping power of charged particles in a medium is defined as the mean

energy lost per unit distance traversed by the particle (ICRU, 1970). The LET for a charged particle traversing a medium such as tissue can be calculated using the Bethe-Bloch formula.

When the target material that the charged particles are traversing is held constant (e.g. human tissue), the only changing variables in the Bethe-Bloch formula are the Z of the particles and the velocity of the particles as a fraction of the velocity of light. Therefore according to the Bethe-Bloch formula, for charged particles of a given velocity but with different Z, the relative contribution to dose from each charged particle is a function of Z^2. When the fractional abundance of elements as seen in Figure 2-3 are scaled by the Z^2 of each element, the HZE particles in the GCR spectrum contribute a large fraction of total dose (Figure 2-4). The largest single contributor to dose by HZE particles is Fe (22% of HZE dose). In addition, Fe is considered to be the most biologically important HZE element in the GCR (NCRP, 1989; NCRP, 2000).

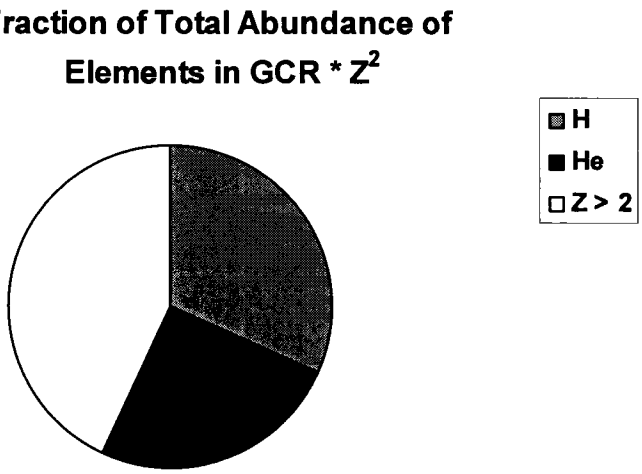

Figure 2-4. Pie chart showing fraction of total abundance of elements hydrogen, helium, and sum of all elements higher in Z than helium in the GCR spectrum with each scaled by the Z^2 of the respective elements.

Absorbed dose is a useful concept for radiation protection, but it does not take into account the fact that different types of ionizing radiation have different biological effects (and associated risks) for a given absorbed dose. To take into account these different biological effects, the concept of dose equivalent, gray equivalent, and equivalent dose were introduced. The SI unit of absorbed dose (D) is the Gray (Gy). The gray equivalent has an SI unit of gray equivalent and is denoted G_T. The SI unit for dose equivalent (H) is the Sievert (Sv). The SI unit for effective dose (E) is also the Sievert (Sv). Detailed definitions of these quantities are found in Appendix A.

Space Radiation Exposure for Different Mission Scenarios

I. Low Earth Orbit

Different mission scenarios involve different potential exposures of astronauts to space radiation. In LEO, the average predicted absorbed dose to the blood forming organs (BFO) of personnel aboard the space shuttle is 0.86 mGy per day, and this absorbed dose translates to a dose equivalent of 1.09 mSv per day. In order to convert absorbed dose to dose equivalent, an average quality factor of 1.3 was assumed. Approximately 8% of this dose equivalent is due to GCR with the remainder coming from trapped protons.

The amount of absorbed dose received by astronauts in LEO is dependent on the inclination of the orbit for each particular mission. Orbital inclination is defined as the acute angle that the trajectory of an orbit makes with the Earth's equator (NCRP, 2000). A low inclination orbit (near the Earth's equator) exposes the astronauts to less radiation than a high inclination orbit (near the Earth's poles). This is due to several factors. Space craft in high inclination orbits (especially those near the polar regions) pass closer to the magnetic field lines and hence to the trapped radiation. This effect is most pronounced for polar orbits and high inclination orbits that pass through the SAA. The International Space Station (ISS) orbits at an inclination of 51.6 degrees and an altitude of approximately 400 kilometers. The orbit of the ISS intersects the SAA, and it is estimated that half of the dose from ionizing radiation received by astronauts occurs during the passage through the SAA. Also, in low

inclination orbits the Earth's magnetic field lines are almost parallel with the Earth's surface. This results in trapping or deflecting of all but the most energetic of the GCR spectrum. In high inclination orbits, more of the lower energy GCR is able to intersect spacecraft resulting in a larger absorbed dose by this radiation.

II. Geostationary Orbit

A mission to geostationary earth orbit (GEO) involves exposure to GCR and the outer-trapped particle belt as well as passage through the inner belt. An average daily dose equivalent to BFO for a 15-day mission to GEO is 4 mSv. Approximately 13% of this dose equivalent would be from GCR.

III. Mission to Mars

It has been estimated that a mission to Mars would involve three years to complete. The average estimated daily dose equivalent to BFO during this time is 1mSv. The majority of the radiation exposure in this mission scenario would be from GCR and protons and electrons from solar particle radiation.

An anomalously large SPE could potentially be fatal to humans. If an anomalously large SPE occurred while astronauts were in deep space (outside the geomagnetic field of Earth), it is possible that they would receive a dose equivalent of 800 mSv to BFO over a period of a few days.

Radiation Protection Standards for Astronauts

All government agencies are required to comply with the Occupational Safety and Health Act (OSHA) regulations (and subsequent amendments) found in the Code of Federal Regulations for Occupational Safety and Health. One of the amendments to this set of regulations allowed government agencies to petition OSHA for permission to have supplementary standards for radiation protection purposes. NASA successfully petitioned OSHA for supplementary radiation protection standards. The primary motivations for this petition were explained in NCRP Report 98 Guidance on Radiation Received in Space Activities (NCRP, 1989):

> "Given the exceptional nature of the occupation, and the great difficulty of reducing exposures in space beyond a certain extent, it seems unreasonable to confine the radiation exposures of crews of space vehicles to the average of the exposure experience of radiation workers on the ground."

The career limits were age and gender dependent, and were based on limiting the increase in the probability of an individual developing fatal cancer to 3% above the baseline risk (Table 2-1).

In addition to career limits, NASA set shorter term radiation exposure limits (Table 2-2). These shorter term limits were developed and implemented to protect astronauts from deterministic radiation effects (NCRP, 1989).

Table 2-1
Career Exposure Limits

Age (y)	Female (Sv)	Male (Sv)
25	1.0	1.5
35	1.75	2.5
45	2.5	3.25
55	3.0	4.0

Table 2-2
Short Term Radiation Exposure Limits

Time Period	Blood-Forming Organs (Sv)	Lens of the Eye (Sv)	Skin (Sv)
Career	See Career Limit Table	4.0	6.0
1 y	0.50	2.0	3.0
30 d	0.25	1.0	1.5

Recent recommendations have been made by the National Council on Radiation Protection and Measurements for radiation protection limits that utilize units of gray equivalent (G_T) and effective dose (E) (NCRP, 2000). The recent recommendations for career limits assume potential radiation exposures over the course of a ten year career and are based on limiting the increase in the probability of an individual developing fatal cancer to 3% above the baseline risk (Table 2-3). In addition to career limits, the NCRP recommends shorter term radiation exposure limits (Table 2-4). These shorter term limits were developed and implemented to protect astronauts from deterministic radiation effects (NCRP, 2000).

Table 2-3
Ten Year Career Equivalent Dose (E) Limits

Age at Exposure (y)	*E Limit* (Sv)	
	Female	Male
25	0.4	0.7
35	0.6	1.0
45	0.9	1.5
55	1.7	3.0

Table 2-4
Recommended Gray Equivalent (G_T) Limits for Deterministic Effects

	G_T Limit (Gy-Eq)		
	Bone Marrow	Lens of the Eye	Skin
Career	---	4.0	6.0
1 year	0.50	2.0	3.0
30 day	0.25	1.0	1.5

Radiation Shielding

Effective shielding of personnel and equipment from GCR is a difficult task. Thin shielding has been shown to reduce dose equivalent as compared with no shielding. Unfortunately shielding effectiveness drops as shielding thickness increases (Badhwar et al., 2000a). This decrease in shielding effectiveness is due to

the production of secondary particles (including neutrons) in the shielding material by primary GCR particles.

For a given density thickness of shielding material, a larger reduction in dose equivalent from GCR can be achieved by using shielding composed of lower Z elements. Density thickness is defined here as the product of the density of the shielding material and the thickness of the shielding material. Common units for the density thickness of shielding materials are g/cm^2. A comparison of the dose-equivalent rates of GCR and trapped radiation as a function of shielding depth between aluminum and polyethylene concluded that the polyethylene was a much better material for reducing radiation exposure (Badhwar and Cucinotta, 2000b; Cucinotta et al., 2001). Low Z shielding materials with a high hydrogen content are capable of stopping a large part of the GCR spectrum while high Z shielding materials are effective at stopping only the highest LET component of the GCR spectrum. Furthermore, low Z shielding materials produce low LET secondary particles while high Z shielding materials produce a broad LET range of secondary particles (Wilson et al., 1995). This characteristic difference in shielding effectiveness between low Z and high Z materials is the reason for the marked difference in the ability of these materials to decrease the dose equivalent rates of GCR.

Radiation Dosimetry

I. Passive Dosimetry

Since exposure of astronauts to radiation is an inevitable consequence of space travel, NASA has used a wide variety of radiation dosimetry devices to determine the absorbed dose and dose equivalent in the space environment. Passive detectors are made of a material or composite of materials that are sensitive to radiation, and are capable of storing information concerning the amount and sometimes type of radiation that they were exposed to. These detectors integrate information while exposed to radiation until their radiation response is extracted from them. Extraction methods include heating, exposure to certain wavelengths of light, chemical developing, and etching in an acidic solution. Some of the advantages of passive dosimeters are that they tend to be small, robust, lightweight, and do not require power to operate during a space mission.

Nuclear emulsions and TLDs were among the passive detectors used during the Mercury space program (NCRP, 2000). The TLDs were used to determine absorbed dose. The nuclear emulsions provided information on the integrated absorbed dose for the space mission, and analysis of the emulsions also determined the LET distribution of the proton radiation field present during the space mission (Schaefer et al., 1970).

Beginning in the Gemini space program an attempt was made to determine the LET distribution of HZE particles present in space. Cellulose nitrate plastic was used

in conjunction with nuclear emulsions to form a passive dosimeter from which information on the fluence of both protons (from nuclear emulsions) and HZE particles (cellulose nitrate) could be determined (Benton and Collver, 1967). This technique of combining different layers of track dosimetry material later included both CR-39 and Lexan polycarbonate (Benton et al., 1977; Benton, 1986). Low energy neutron detection was accomplished using fission foils as passive dosimeters.

II. Active Dosimetry

Active radiation dosimeters are a general classification of instruments that collect charge from an interaction of radiation with part of the dosimeter. These instruments are diverse in the way that radiation interacts with their radiation sensitive regions, but they all consume power, process the charge collection signals, and store the information in some form of memory device. A significant advantage of active dosimeters aboard space flights is the ability to separate the GCR spectrum from the trapped proton spectrum during a space mission in LEO. This is important because almost all of the dose received from trapped protons during a LEO space mission occurs during the traversal of the SAA, while GCR is present at all times during the mission. Passive dosimeters such as the Lexan and CR-39 stacks and TLD's integrate information on the radiation environment during the entire space mission (or until they are analyzed). Active dosimeters are capable of storing information on the radiation fields along with the time in which the exposure took place. Active dosimeters store (and can display) dose and dose equivalent information

every minute of operation, although in some instruments this time resolution can be as small as every four seconds. This is especially useful from a radiation protection standpoint in the event of a rapid change in the radiation field in space (such as would occur during an SPE).

Several types of active dosimeters have been used during space flights. During the Mercury space program personal ionization chambers were worn by astronauts to estimate their absorbed dose received during the mission.

Particle spectrometers containing lithium drifted silicon detectors have been used to estimate the LET spectrum of both GCR and trapped protons during space missions. The Proton Heavy-Ion Detection Experiment (PHIDE) and the Real-time Radiation Monitoring Device (RRMD-III) are particle spectrometers that use several position sensitive silicon detectors stacked on top of one another (Badhwar et al., 1995; Sakaguchi et al., 1999). These spectrometers track individual charged particles as the particles pass through the silicon stack. Information including the particles mass, energy and LET are determined from the resulting data.

Another type of active dosimeter is the tissue equivalent proportional counter (TEPC). TEPC's have been used during space flights to determine the absorbed dose and dose equivalent (as well as the rates of each of these quantities) of the space radiation environment (Badhwar et al., 1992). The active volumes of these TEPC's simulate a small volume of tissue (with dimensions on the order of microns) by use of a low-pressure tissue equivalent gas. The data recorded by the TEPC (and its associated electronics) is a spectrum of the energy deposited in the active volume.

This spectrum is converted into a lineal energy spectrum and used to determine the absorbed dose and dose equivalent (Appendix A).

Modeling of Radiation Transport

I. Large Scale Modeling

Modeling the radiation transport of a mixed radiation field is also used to calculate an estimate of the dose and dose equivalent in space. The heavy ion transport code HZETRN uses the Boltzmann transport equation to propagate high-energy heavy ions through various media. HZETRN uses the galactic heavy ion transport code GCRTRN to model the GCR spectrum that is assumed to be incident upon the area of interest. HZETRN further uses the nucleon transport code BRYNTRN to calculate details of the heavy ion transport in matter. Interaction cross sections and slowing down approximations of these ions with intervening media are used to determine the ion spectrum and energy spectrum of the ions at points along the straight ahead trajectory. The resultant spectrum is used to calculate dose and dose equivalent at a chosen point along the particles' track (Wilson et al., 1991).

II. Small Scale Modeling

Calculations of the dose and dose equivalent by HZE particles are not the only modeling applications used in space radiation research. To understand the potential

risks of the exposure of human cells to HZE radiation, track structure models are applied to volumes that approximate that of a human cell. Two of these models are the spatially restricted LET equation (Xapsos, 1992) and the heavy ion radial dose model (Cucinotta et al., 1995).

The spatially restricted LET equation calculates the energy deposited in a specified volume by an HZE particle. The dimensions and geometry of the volume of interest provide the input to the model for how the LET of the HZE particle is spatially restricted. Other inputs to the model are the energy of the particle, LET of the particle and the mean excitation energy of the medium (Appendix B). One application of this model has been to calculate the energy deposition response function of TEPCs to particle irradiation (Shinn et al., 1999b).

The heavy ion radial dose distribution model has input parameters of the energy, charge number and mass number of the HZE particle of interest. The output of this model is in the form of dose to water (Gy) at 100 discrete radial distances from the HZE track (Appendix C). One of the applications of this model has been to calculate the radial dose from HZE particle tracks to different materials that are found aboard spacecraft.

The dominant mechanism for energy transfer between high-energy ions and the surrounding medium are tracks from secondary electrons that were ejected from the primary particle track (Cucinotta et al., 2000). The Rudd model is a simple analytical equation that calculates the spectrum of electron energies ejected from a high-energy ion track per unit track length (Rudd, 1989) (Appendix D).

After these secondary electrons are ejected from the particle track, they deposit energy in the surrounding medium. The Kobetich and Katz model for electron energy dissipation calculates the distribution of energy dissipation of these electrons as a function of distance that they travel (Kobetich and Katz, 1969).

Experiments Characterizing Dosimetry Devices

In order to test models involving high-energy ions as well as characterize the response of different radiation detectors to these same ions, experiments are conducted at particle accelerator facilities. At these facilities particles are accelerated to energies similar to those found in the GCR spectrum. There are many facilities around the world that are capable of accelerating ions to high-energies. The following facilities are mentioned because they are the accelerators most commonly used by the NASA-funded space radiation community.

The proton synchrotron at Loma Linda Medical University is capable of producing protons with energies up to 250 MeV. The Heavy Ion Medical Accelerator (HIMAC) at the National Institute of Radiological Sciences in Chiba, Japan can accelerate various ions from protons to iron up to energies in the 100's of MeV/n. The Alternating Gradient Synchrotron (AGS) at Brookhaven National Laboratory in Upton, New York accelerates iron particles and a number of other heavy ions to energies exceeding 1000 MeV per nucleon. Brookhaven National Laboratory houses the NASA Space Radiation Laboratory (NSRL). The NSRL particle beam line was built to extract ions from the booster synchrotron that feeds ions into the AGS. This

synchrotron can deliver the same ions as the AGS, but at energies ranging from below 100 MeV/n to 1000 MeV/n.

Computations done using the HZETRN computer code have been subject to extensive testing at particle accelerator facilities. One of the goals of the development team of HZETRN is a final code for shielding from GCR that has been validated by controlled laboratory experiments (Wilson et al., 1991).

Track dosimeters and TLDs have been calibrated using particle accelerator facilities for many years (Benton et al., 1977, Yasuda et al., 2000). Track dosimeters were calibrated using particles with known energies and LET (Benton and Collver, 1967). Different etching or developments processes were also tested on track etch stacks after exposure to different high-energy ions in order to improve the accuracy of their radiation response. The response of TLDs to high-energy ions is known to be dependent on the incident particle atomic number and energy. TLDs are therefore carefully calibrated using a particle beam. High-energy ions of a known energy and LET are incident upon both TLD material and precision ion chambers (PIC) in order to characterize the response of the TLDs to different levels of absorbed dose (as measured by the PIC) (Yasuda et al., 2000).

Previous measurements of TEPC response have used particle accelerators to produce HZE radiation of energies similar to those found in the GCR spectrum. Table 2-5 summarizes some of these experiments. Glass and Braby exposed a wall-less microdosimeter to a broad beam of alpha particles (Glass and Braby, 1969). In this experiment comparisons were made between the detector energy deposition response and a calculated theoretical response function.

Table 2-5
Previous Experiments with HZE Particle Beams Using A TEPC

Reference	*TEPC Type*	*Particle Species*	*Particle Beam Energy (MeV/nucleon)*	*Position and Particle Identification*
Glass and Braby 1969	Spherical wall-less	He	1.125	None
Rodgers et al. 1973	Spherical walled,Spherical wall-less	N	3900	None
Kliauga et al. 1978	Spherical wall-less	C, Ar	400, 450	None
Luxton and Fessenden 1979	Spherical walled	He, C, Ne	230, 400, 400	None
Dicello et al. 1980	Spherical walled	π^-	167	None
Ito and Henkelman 1988	Spherical walled	π^-	180	Time-of-flight velocity determination
Metting et al. 1988	Cylindrical wall-less	Fe	600	One dimensional positional and species determination by PSD
Dicello and Wasiolek 1991	Spherical walled, cylindrical wall-less	Fe, Ar, Ne, C	535, 570, 557, 400	None
Rademacher et al. 1998	Spherical walled	Fe	1050	Two dimensional positional and species determination by PSD's

. In a series of experiments by Rodgers et al. both a walled and wall-less microdosimeter simulating a 2-μm diameter sphere of tissue were exposed to 3.9 GeV Nitrogen ions.(Rodgers et al., 1973). Event distributions were determined for both counters at various depths in a water and plastic phantom. Measurements were made to compare the response of the walled and wall-less detectors under identical irradiation conditions. Kliauga et.al. performed a series of irradiations exposing two wall-less microdosimeters to 400 MeV/nucleon ^{12}C and 450 MeV/nucleon ^{40}Ar beams (Kliauga et al., 1978). A ridge filter was used to spread out the Bragg peaks of the incident ions. Energy response spectra of the wall-less microdosimeters were taken at several points along these Bragg peaks. Luxton and Fessenden irradiated a 12.7-mm diameter TEPC with a 2.5-mm tissue equivalent (TE) wall (Luxton and Fessenden, 1979). This TEPC simulated a 2-μm diameter sphere of tissue using a TE gas at a pressure of 67 torr in the active chamber volume. This series of experiments found values for the dose-averaged lineal energy of carbon, helium and neon at initial energies of 400 MeV/nucleon, 230 MeV/nucleon and 400 MeV/nucleon respectively. Dose-averaged lineal energy values were also taken for these three particle beams as each beam was modified with a variable thickness water column. Dicello and Wasiolek compared measurements of microdosimetric spectra for energetic ion beams using a spherical walled detector and a cylindrical wall-less detector (Dicello and Wasiolek, 1991). They observed a large range of energy depositions including very large events, but could only speculate on reasons for the shape of the distributions because they did not have precise information on the type (i.e. incident

ion or fragment) or location of the particles as they entered the detector. Dicello et al. also compared measurements of the microdosimetric spectra from a TEPC simulating a 2-μm diameter of tissue with that from a 0.1-cm radius lithium drifted silicon detector (Dicello 1980). Both of these instruments were exposed to a negative pion beam. Metting et al. determined energy deposition in a wall-less microdosimeter as a function of impact parameter for 600 MeV/ nucleon ^{56}Fe particles (Metting et al., 1988). They were able to measure energy deposition as a function of radial distance from the track. This provided information concerning the dimensions of the track as well as characteristics of energy deposition as a function of radius. Ito and Henkelmen irradiated a 12.7-mm diameter microdosimeter simulating a 2-μm diameter sphere of tissue with a pion beam (Ito and Henkelmen 1980). This experiment incorporated a time of flight (TOF) technique that allowed the separation of the pion particles from other particles in the beam. Energy deposition spectra were obtained for the microdosimeter at 17 positions in a water phantom. An experiment performed by Rademacher et al. used a solid walled 12.7-mm diameter TEPC that was exposed to 1.05 GeV/ nucleon ^{56}Fe particles (Rademacher et al., 1998). The detector was part of a particle spectrometer consisting of thin Si detectors that could identify the type and position of incident particles upstream and downstream of the TEPC. They measured the patterns of energy deposition as a function of trajectory through the detector and made a quantitative assessment of how the wall affects this response.

Contributions From This Work

In this work, data were obtained at ground based accelerator facilities that produced beams of ^{56}Fe with kinetic energies between 200 and 1000 MeV/nucleon ($\beta = v/c = 0.56 - 0.88$). Specifically, a spherical TEPC was exposed to ^{56}Fe beams at energies spanning the peak of the GCR Fe spectrum. In each case a particle spectrometer measured the charge and position of each incident particle both upstream and downstream of the TEPC. With this experimental arrangement, the trajectory of the particle through the TEPC could be reconstructed and related to the energy deposition recorded by the detector. Frequency distributions of energy deposition (i.e., response functions) were determined for uniformly incident beams of Fe, and these distributions were used to compute absorbed dose as well as average values of lineal energy, y (Appendix E). These frequency distributions were also used to calculate average quality factors for each experiment using the method found in Appendix A.

The response of the TEPC to Fe particles was modeled using three track structure models. The spatially restricted LET equation (Xapsos, 1992) and the heavy ion radial dose model (Cucinotta et al., 1995) were used to calculate energy deposition by Fe particles in the TEPC for different particle trajectories. These two models were further used to calculate frequency distributions of energy deposition by a uniform irradiation of Fe particles. A code was developed to calculate energy deposition in the TEPC by high-energy particles having the condition that they

traversed the entire diameter of the TEPC. The Rudd, and Kobetich and Katz models were used in this code along with a distribution for angular ejection of electrons from a particle track (Cucinotta et al., 1995). This code was written in the PERL programming language and was named BTC4.

CHAPTER III – MATERIALS AND METHODS

Six experiments were performed, four with the Alternating Gradient Synchrotron (AGS) at Brookhaven National Laboratory in Upton, NY, and two at the Heavy Ion Medical Accelerator (HIMAC) at the National Institute of Radiological Sciences in Chiba, Japan. Features of the six experiments are summarized in Table 3-1.

Table 3-1
Properties of the ^{56}Fe Beams Used in the Experiments.

Experiment Name	Extracted Beam Energy (MeV/nucleon)	Energy at Entrance to TEPC Gas Cavity (MeV/nucleon)	Velocity of ^{56}Fe (β)	Maximum Energy of Electron Ejected From ^{56}Fe Track (MeV)
HIMAC00	250	200	0.57	0.48
HIMAC99	400	360	0.69	0.93
BNL97_1	600	540	0.77	1.51
BNL98	1087	700	0.82	2.09
BNL97_2	1087	790	0.84	2.44
BNL99	1087	1000	0.87	3.33

For each experiment, calculations were performed to determine the energy of the Fe particles after passing through the vacuum window, and through the experimental apparatus upstream of the TEPC. During the experiment BNL97_2, 8.2-cm of polyethylene was placed in the particle beam upstream of all experimental apparatus to reduce the energy of the primary beam. During the BNL98 experiment, this procedure was repeated with 12.5-cm of polyethylene in the beam. Data for the experiment were taken only for Fe particles that entered the experimental apparatus. Data was not taken for Fe particles that fragmented in the polyethylene. The process of data collection is explained in detail later in this section and in Appendix F.

The same spherical TEPC[1] was used in all six experiments. The TEPC had an active volume 12.7-mm in diameter and a tissue equivalent wall 2.54-mm thick (Fig. 3-1). The active volume was filled with a propane-based tissue equivalent gas at a pressure of 33 torr, simulating a sphere of tissue having a diameter of 1-μm (Appendix A). An anode wire ran the full diameter of the active volume and this anode wire was surrounded by an anode helix. The purpose of the anode helix was to form a uniform electric field between itself and the anode wire. The region between the anode wire and the anode helix is where electron multiplication occurs of the initial ionization electrons. The uniform electric field in this region insures uniform multiplication of these electrons. Calibration was accomplished using an internally mounted ^{244}Cm alpha particle source that was mounted with a gravity-controlled gate. When the TEPC was inverted from its operational orientation, the gate opened and

[1] Far West Technologies, Inc. Goleta, CA.

alpha particles emanating from the source deposited 84.15 keV in the TEPC gas cavity.

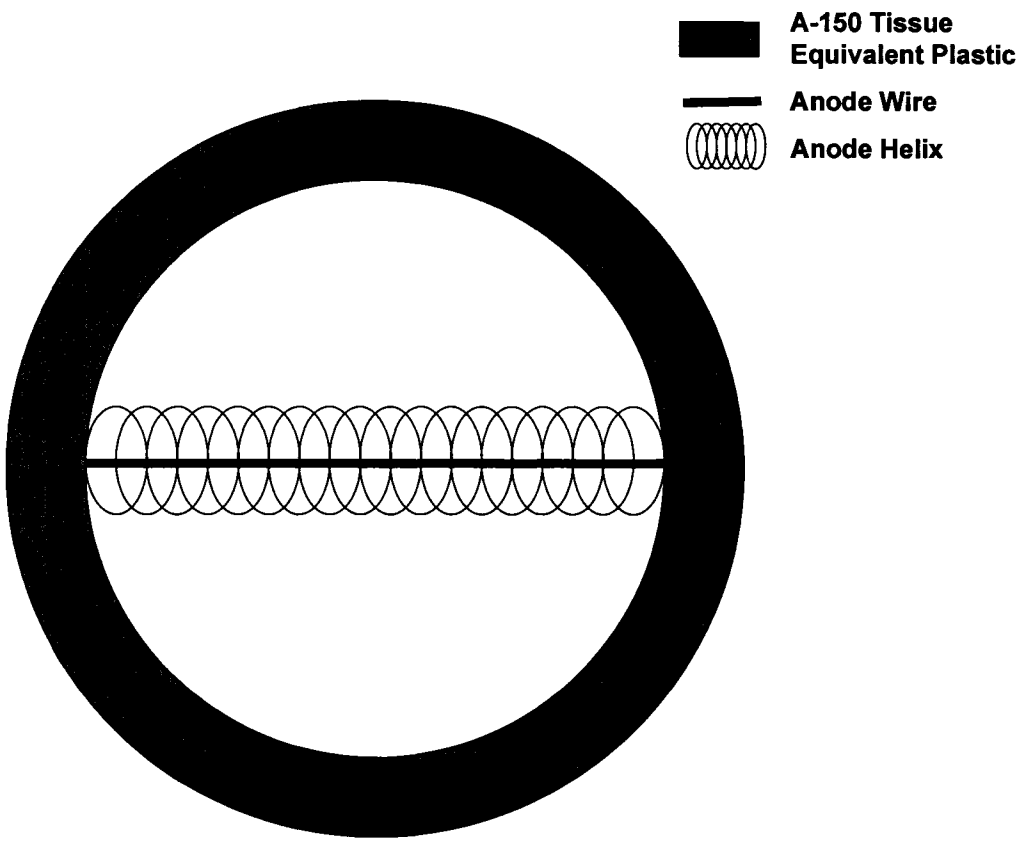

Figure 3-1. Diagram of the TEPC.

In each of the six experiments, the energy signal from the TEPC was sent to an EG&G Ortec [2] charge sensitive preamplifier, the output of which went to two separate EG&G Ortec shaping amplifiers. The gains of the two shaping amplifiers were set so that the difference in amplification was approximately a factor of 12.

The TEPC was positioned within a particle spectrometer (Fig. 3-2) that measured individual particle events during the experiment. Four pairs of PSDs (denoted PSD1-PSD4 in Fig. 3-2) were used to track both the position and the energy of each particle as it passed through the apparatus. An individual PSD measured a single Cartesian coordinate (X or Y). Thus each pair determined the position of each particle in the transverse plane. The PSDs were lithium-drifted silicon detectors fabricated in the shape of circular disks, with radii of 20-mm and thickness between 800-μm and 1050 -μm. The total charge collected, Q, on one side of the detector, was proportional to the total amount of energy deposited in the PSD by the particle. On the other side of the detector, charge was divided between the top (q_1) and bottom (q_2) of a PSD (for the Y coordinate), or left (q_1) and right (q_2) of a PSD (for the X coordinate PSD). The amounts of charge collected in q_1 and q_2 can be related to the X or Y position of the incident particle (Wong et al., 1990). One X and one Y PSD were used in each PSD pair as seen in Fig. 3-2. One 3-mm thick lithium drifted silicon detector was placed downstream of the PSDs to provide additional energy deposition information for each particle.

The data acquisition system was triggered by a coincidence between the TEPC signal and one of the PSD signals upstream of the TEPC. Data were recorded on an event-by-event basis (Appendix F). For each experiment, data for a minimum of 2 million triggers were recorded. Iron ions can fragment into lighter ions as they

[2] EG&G Ortec, Oak Ridge, TN

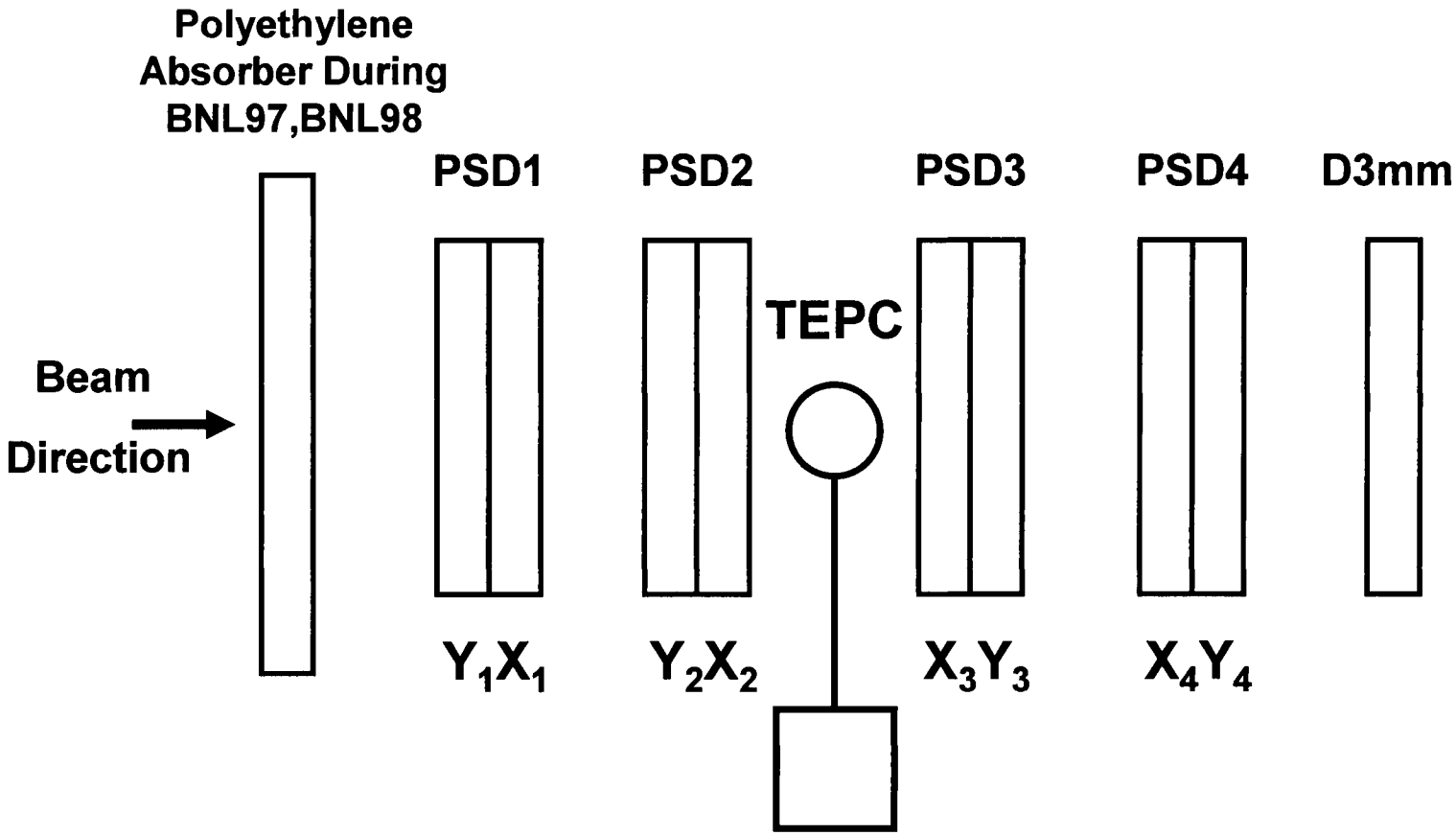

Figure 3-2. The experimental apparatus, showing the position of the TEPC within the particle spectrometer.

pass through materials. The trigger threshold in the PSD was set so that only primary beam ions and fragments within a few charge units of the primary fired the trigger.

The data recorded during the experiment were subject to extensive refinement during offline analysis. For this analysis, energy deposition signals from PSDs both upstream and downstream of the TEPC were used to select events corresponding to the passage of Fe through the TEPC, thereby giving a clean sample of events.

The two signals q_1 and q_2 produced by each PSD were related to either the X or the Y coordinate of the traversing particle. In certain regions of the PSDs, positions as calculated by the nominal method (Wong et al., 1990) are systematically in error; the errors are smallest near the center of the detectors and increase towards the edges. During offline analysis, a calibration procedure was used to correct for these distortions, yielding improved accuracy in the position determination. A mask was fabricated, consisting of a thick (2.54 cm) brass plate with holes 0.8-mm in diameter drilled through it. The holes were spaced 6-mm apart in a radial pattern. During the experiments, dedicated data-taking runs were performed with the mask aligned and upstream of a PSD pair. The brass plate was thick enough to stop Fe particles, so that only particles passing through the holes were registered in the PSD (Figure 3-3). The procedure was repeated for each PSD pair.

The data were used to obtain a transformation from q_1 and q_2 into the corresponding position (X,Y). This alignment was achieved by performing univariate

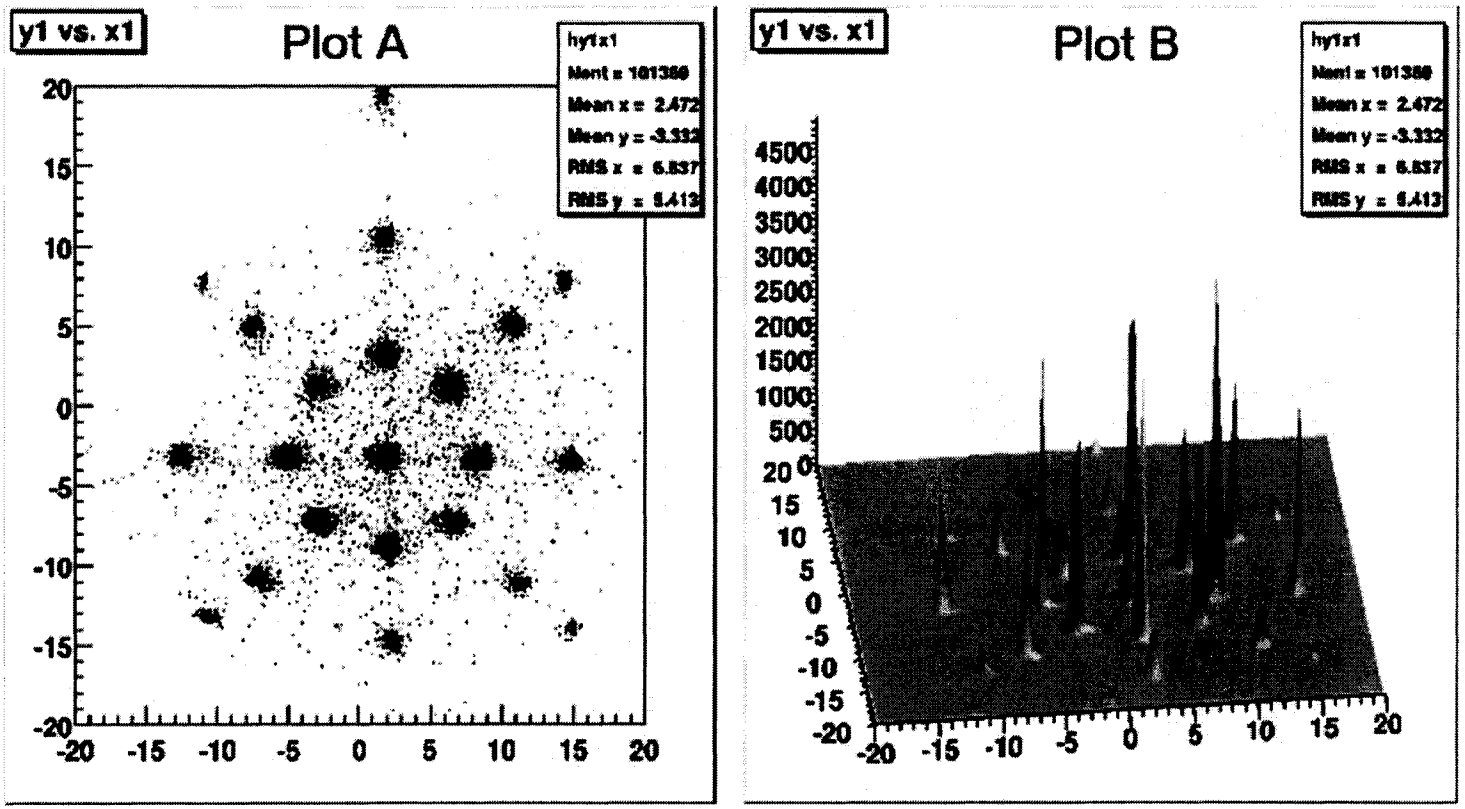

Figure 3-3: Plot A: Scatter plot of original uncorrected data coordinates of particles that penetrated the brass masking plate during 200 MeV per nucleon Fe mask data run. Plot B: 3-D histogram of data from Plot A. Z-axis is number of particles.

multiple regressions on the PSD response data similar to the method described by Wong et al. and Chapman (Wong et al. 1990; Chapman, 2000). The known coordinate (Y and X) of each of the 17 holes that were drilled into the brass mask, and the coordinates of the original data position derived from q_1 and q_2 (called u and v) were used in this multiple regression. The regression model used to transform the data for point number 1 in the brass mask (center data point in Figure 3-3) is shown below.

$$X_1 = A + Bu_1 + Cu_1^2 + Dv_1 + Ev_1^2$$
$$Y_1 = F + Gu_1 + Hu_1^2 + Iv_1 + Jv_1^2$$

Equation 3.1

Each of the 17 known values of Y and X had a regression model with a form that was identical to the Y_1 and X_1 models shown above. The X models and the Y models were regressed separately. The regression model of the X coordinates data points in Figure 3-3 yielded a resulting R-Square value of 0.999 and a Sum or Squares error of 0.593. Inspection of the studentized residuals vs. predicted values plot indicated that there was no violation of the assumption of homogeneity of variance for this model.

During offline data analysis the parameters obtained from the regression equation were then used to transform all u and v data points into X and Y corrected coordinates. The transformed coordinates were then used in all further data analysis. Figure 3-4 illustrates the true coordinates of each hole in the mask as well as the uncorrected data point and the corrected data point.

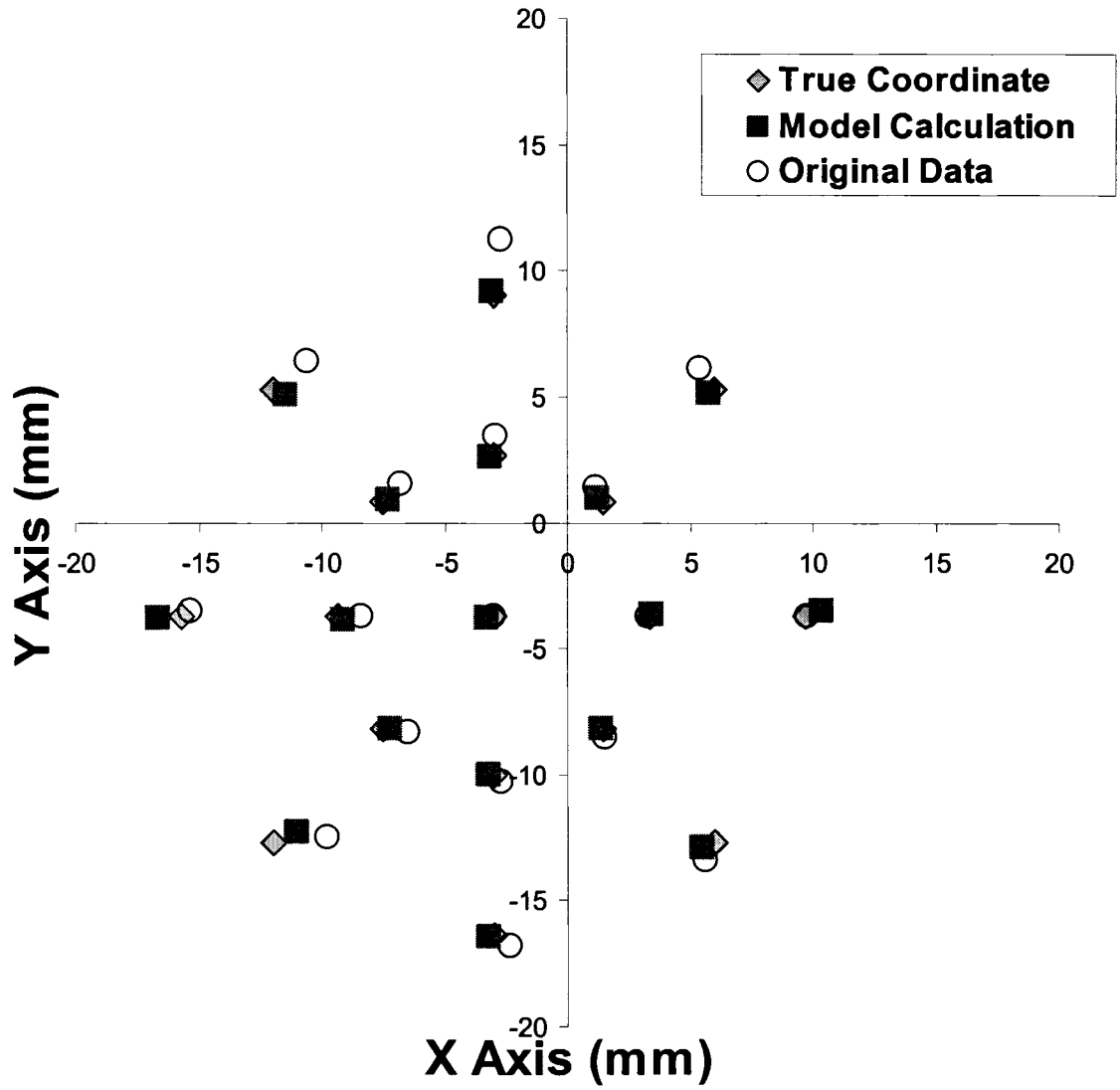

Figure 3-4. Scatterplot of true coordinate (gray triangles), univariate regression model calculation (gray square), and original data from dedicated data run (open circle). These data were taken from the 200 MeV per nucleon Fe experiment.

The magnitude of the total-charge signal Q from each PSD was proportional to the amount of energy deposited in the PSD by the traversing particle. The energy deposition spectrum for each PSD had a prominent peak corresponding to

the primary Fe, and distinct peaks corresponding to particles with charges less than that of the primary particles. Peaks with energy deposition higher than the Fe peak were also present. These peaks were caused by multiple particles striking the PSD in a short enough time frame that the energy deposition for each particle was integrated by the data taking system. Because the forward-going projectile fragments continue with velocities close to that of the incident beam, the energy deposition is approximately proportional to the square of the fragment charge. In the offline analysis, this information was used to select only those events where the incident Fe did not fragment in the TEPC or elsewhere. The resulting data set was then used in all subsequent analysis.

In the data analysis, the X, Y and Z positions of a particle were defined relative to the center of the active volume of the TEPC, using information from PSD2. The Z-axis is defined to be the primary beam direction; X and Y represented orthogonal coordinates in the transverse plane. The impact parameter is defined as the radial distance in millimeters from the center of the TEPC, so that particles traversing the full diameter of the active volume of the TEPC had impact parameters near 0-mm. Particles that traversed the TEPC at the interface between the active volume and wall had impact parameters equal to 6.35-mm. Particle events that grazed the outside edge of the wall had impact parameters equal to 8.89-mm.

There was no attempt to actively suppress electronic noise in the TEPC and amplifiers. During each run random triggers were supplied to the data acquisition system. These events were easily recognized in the analysis as having an energy signal from the TEPC but with no energy deposited in the PSDs. The distribution of

the TEPC signals on these events indicated that energy depositions below 3 keV could not be distinguished from noise.

Many events that satisfied the Fe selection criteria in the PSDs had energy depositions below 3 keV in the TEPC. Virtually all of these events had impact parameters greater than 8.9-mm, which meant that they missed the TEPC altogether. Fig. 3-5 shows the energy deposition distribution for these events. The primary graph in Fig. 3-5 is the complimentary cumulative distribution of events when the impact parameter was greater than 8.9-mm. The insert in Fig. 3-5 is a histogram (i.e. density distribution) of the number of these same events versus energy deposition in the TEPC. This Figure illustrates that there are occasional high-energy deposition events that occur at impact parameters greater than 8.9-mm. A comparison of the data found in Fig. 3-5 and the distribution of random-trigger events concluded that these two spectra were virtually identical. In both spectra, 99% of the events had energy deposition of less than 3 keV.

A scatter plot of energy deposition in the TEPC versus impact parameter for impact parameters greater than or equal to 8.9-mm is shown in Fig. 3-6. A chi-squared test of independence was performed on the events shown in Fig. 3-6. The chi-squared test was constructed to determine if there was a correlation between the energy deposited in the TEPC and the impact parameter of the event.

The results of this test concluded that there was no statistical basis for any correlation between the energy deposited in the TEPC and the impact parameter of these events ($p = 0.62$). A chi-squared test of independence performed on events from the same experiment with impact parameters less than 8.9-mm showed that there was

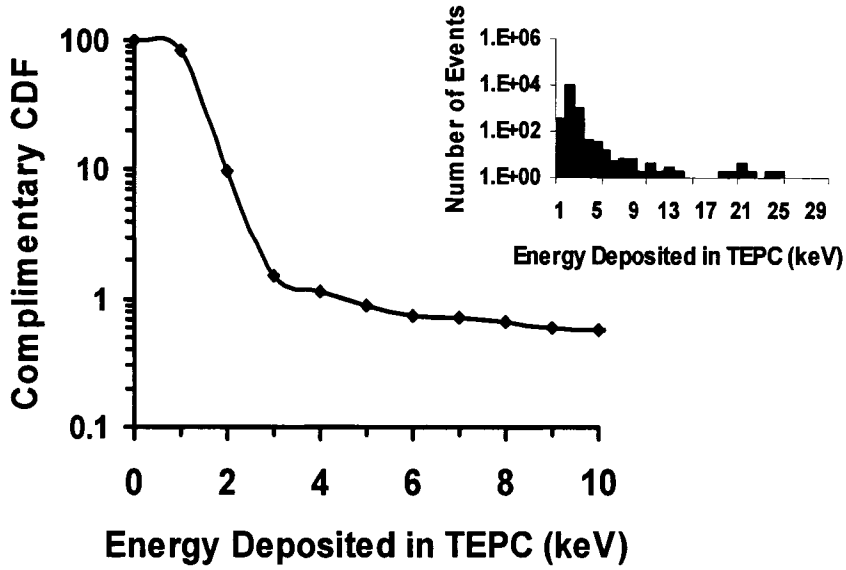

Figure 3-5. Distribution of energy deposition in the TEPC by 200 MeV/n Fe particles with impact parameters greater than 8.9-mm. Density distribution of same events shown in insert.

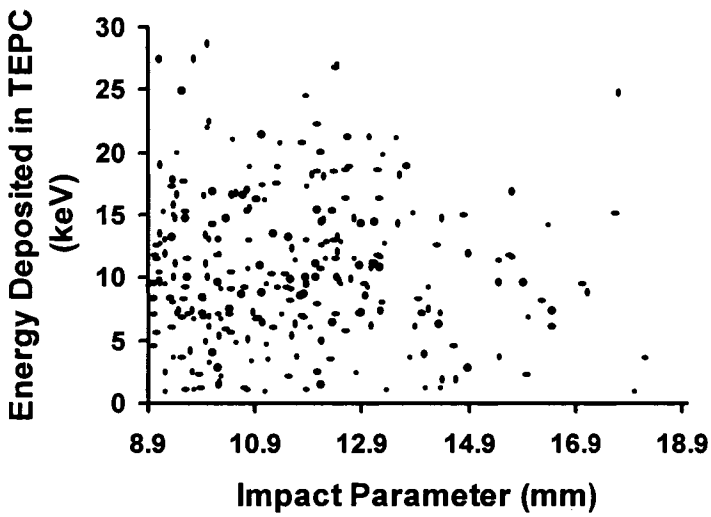

Figure 3-6. Scatter plot of energy deposition in the TEPC vs. impact parameter for 200 MeV/n Fe particles with impact parameters greater than 8.9-mm.

a strong dependence between energy deposited and impact parameter. ($p < 0.001$). We conclude that the energy deposition in the TEPC by particle events with impact parameters greater than 8.9-mm were consistent with electronic noise. These events were therefore excluded from further offline analysis.

The fluence of Fe ions through the TEPC was not spatially uniform. In order to obtain the complete response of the TEPC for a uniform beam, the data for all incident Fe particles were separated into a grid with a resolution of 1-mm x 1-mm. The corresponding event size distributions for each grid were normalized to one incident particle and the spectra for each grid combined to form the response for uniformly incident Fe ions (Appendix E). This distribution is referred to as the response function for the spherical TEPC. The response function for a given experiment was used to obtain average values corresponding to absorbed dose, frequency averaged lineal energy, $\overline{y}_f$, and dose averaged lineal energy, $\overline{y}_D$. In addition, the response function for a given experiment was used to determine whether charged particle equilibrium (CPE) existed in the TEPC during that experiment. Details concerning the method used to determine whether CPE existed in the TEPC for a given experiment may be found in Appendix E. This method was used to calculate a parameter, Λ, for each experiment. Under conditions of CPE, the calculated value for Λ would be equal to the LET of the incident particles used in that experiment (Appendix E).

A radial track structure model developed by Cucinotta et al. and the spatially restricted LET equation developed by Xapsos were used to compute energy depositions in spherical volumes for comparison with the measured data (Cucinotta et

al., 1995; Xapsos 1992). The outputs from these models (in the form of energy deposition in tissue) were superimposed on a sphere simulating incident ^{56}Fe particles at different impact parameters (Appendix B, Appendix C). These distributions were further used to calculate a response function of energy deposition for a uniform irradiation of sphere.

The BTC4 code was used to calculate energy deposition in the TEPC by high-energy particles having the condition that they traversed the entire diameter of the TEPC. Calculations from this code were compared with experimental data.

CHAPTER IV – RESULTS

Experimental Results

Figure 4-1 shows the distribution of energy deposited in the TEPC by 360 MeV per nucleon Fe particles with impact parameters of less than 0.5-mm, i.e., particles passing through the center of the detector. The path length of particles through the active volume of the spherical TEPC changes by less than 2% as the impact parameter of the particle changes from 0-mm to 1-mm. Since the estimated uncertainty in the position measurement of the particles was less than 0.5-mm, the particle path lengths through the detector for events in this distribution were therefore known to within a 2% uncertainty (Gersey et al., 2002). The mean of the distribution is 173 keV (FWHM 16%). The variance in the energy deposition in the main peak of this distribution is almost entirely attributable to variations due to energy-loss straggling and gas multiplication within the TEPC. The LET of a 360 MeV/nucleon ^{56}Fe ion is 214 keV/μm. Therefore on average 81% of the LET of this ion (with an impact parameter of 0-mm) was deposited in the TEPC active volume. Delta rays are produced by the ion in the front wall of the detector and some of these delta rays enter the TEPC active volume. Delta rays are also produced by the ion in the gas inside the TEPC active volume. It is assumed that some of these energetic delta rays escape the

TEPC active volume, and this escape reduced the amount of energy deposition recorded by the TEPC to a fraction of the LET of the incident particle. Similar results were observed for all incident energies and are summarized in Table 4-1 (see Appendix G for energy distributions).

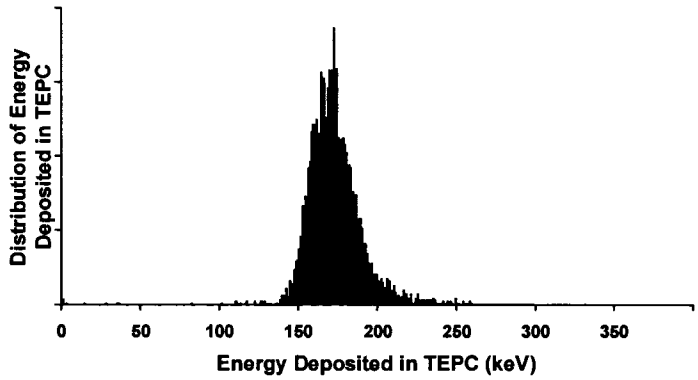

Figure 4-1. Distribution of energy deposited in the TEPC by 360 MeV per nucleon Fe particles with impact parameters less than 0.5-mm.

Table 4-1
Summary of Data Calculations for ^{56}Fe.

^{56}Fe Beam Energies (MeV/nucleon)	LET of ^{56}Fe Particles (keV/μm)	Energy Deposited for Events with Impact Parameter = 0-mm (keV)	$\bar{y}_f$	$\bar{y}_D$	Λ
		Data Mean (FWHM)	(keV/μm)		
200	302	254 (35)	199	328	309
360	214	173 (28)	146	216	227
540	179	136 (24)	134	173	178
700	163	127 (19)	125	159	N/A
790	157	117 (13)	118	153	N/A
1000	149	116 (12)	106	147	154

Figure 4-2 shows the complete response of the spherical TEPC for a uniformly incident beam of 360 MeV per nucleon Fe particles. There is a broad distribution of energy deposition, with a peak near 160 keV, and a large number of events with very small energy depositions, continuing below 50 keV. As described earlier, these are significantly above the electronic noise (99% of which is below 3 keV), and the number of events does not correspond to the expected chord length distribution for a uniformly incident beam of particles incident upon a sphere (i.e., μ-randomness) (Appendix A). There is also a long tail of events with very large energy depositions above 200 keV. Some of these events deposit more than twice the energy expected for a particle with this LET having the maximum trajectory through the sphere. Data from the other experiments have shown that the shape of the response functions were similar for all energies (Appendix G).

In order to understand the shape of the response function, the energy deposition distribution was separated into three regions, A, B and C, as shown in Fig. 4-2. The X and Y coordinates of the incident particles in each region were plotted in a three dimensional histogram with the base of the histogram corresponding to the X-Y coordinate when Z = 0 (i.e. center of the sphere in the direction of the beam). The results for all three regions are shown in Fig. 4-3.

Events in region A are due to ions that pass through the center of the detector. Events in the broad peak from 50 to 200 keV correspond to particles passing through the sensitive volume of the TEPC (Figure 3-1). The small energy

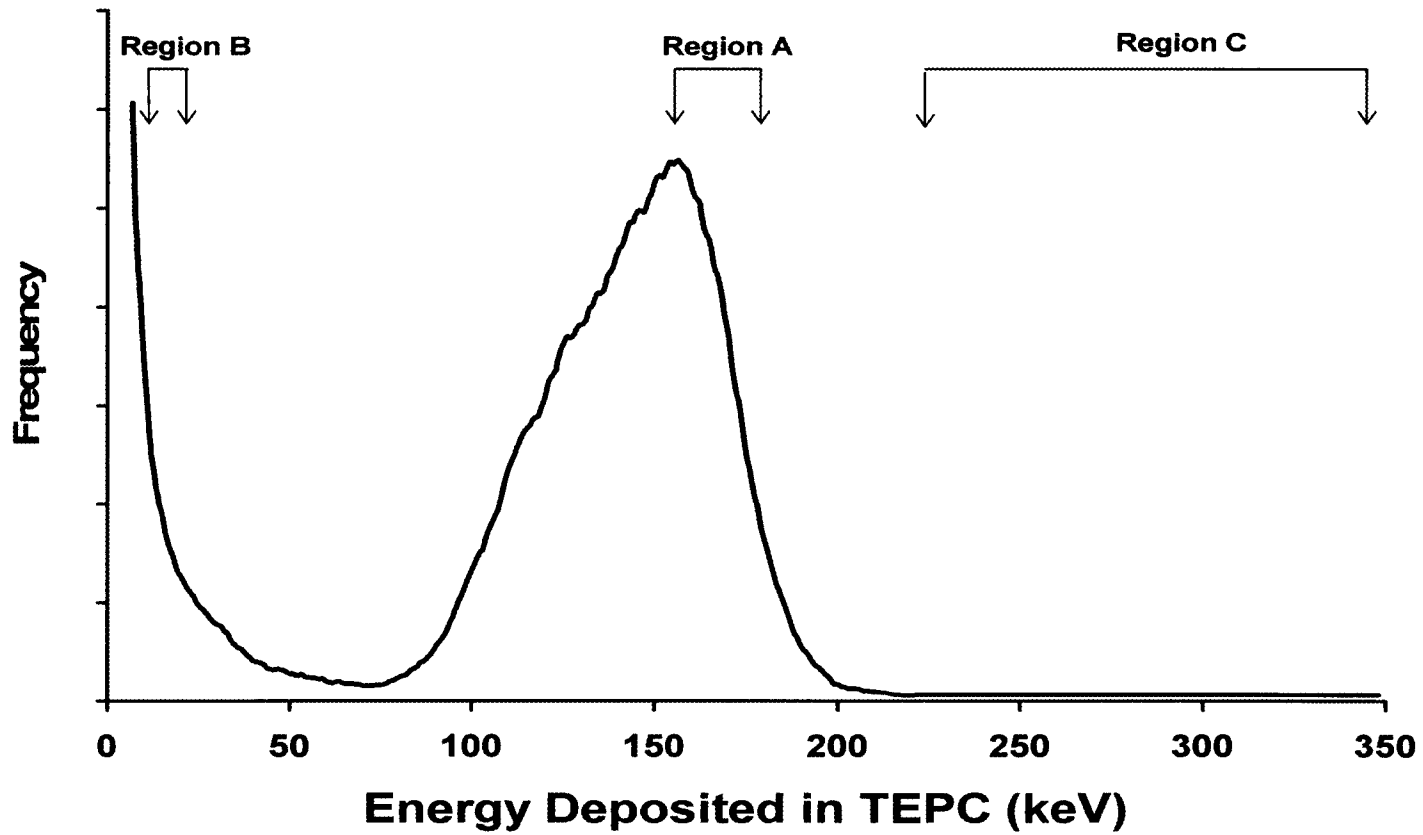

Figure 4-2. Probability density distribution (i.e. Response Function) of energy deposited in the TEPC by a uniform beam of Fe particles at 360 MeV/n. Three regions of energy deposition are indicated as A, B, and C.

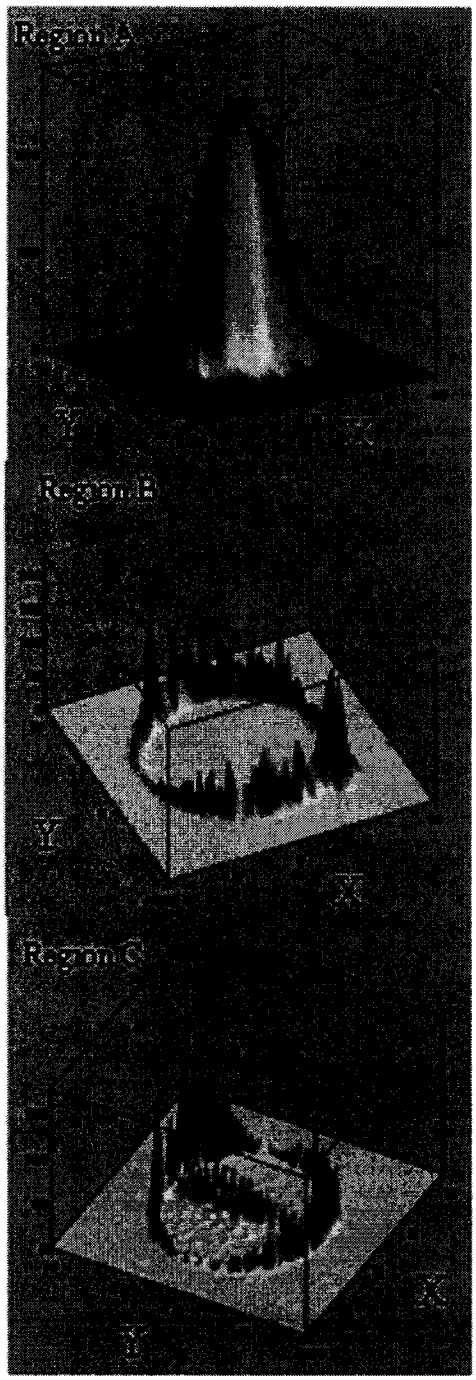

Figure 4-3. Three-dimensional histograms of the three regions of energy deposition selected in Figure 4-2. The X and Y-coordinates represent the particle location in the plane normal to the beam axis. Z-coordinates represent frequency of particle events.

depositions in region B are from particles that pass through an annular area corresponding to the dimensions of the plastic wall of the TEPC. Electrons that originate in the wall and manage to penetrate into the sensitive volume cause these events. The very large energy depositions in region C also have an annular pattern, as well as a cluster of events along a line through the detector. The events in this annulus have a mean impact parameter that is very near the diameter of the sensitive volume. Thus when a Fe ion grazes the inside edge of the wall, a large number of soft delta rays penetrate into the sensitive volume and create a large pulse that resembles the passage of a very high LET particle through the gas volume. The events along the centerline are generated when the Fe particle passes through the sensitive volume and strikes the anode or helix wires. These wires are very thin (45-um) with high density ($\rho = 7.8$ g cm^{-3}). The resulting burst of electrons from the wire produces a large pulse comparable to that generated by the passage of a very high LET particle.

Energy deposition as a function of impact parameter was calculated for each ^{56}Fe beam energy. Figure 4-4 shows the results for 360 MeV/nucleon. The black circles correspond to the mean energy deposited for the corresponding trajectory. The combined uncertainty in the estimated impact parameter and mean energy deposition is on the order of the symbol size. The procedure for determining the mean energy deposited was similar to that used by Rademacher et al. (Rademacher et al., 1998).

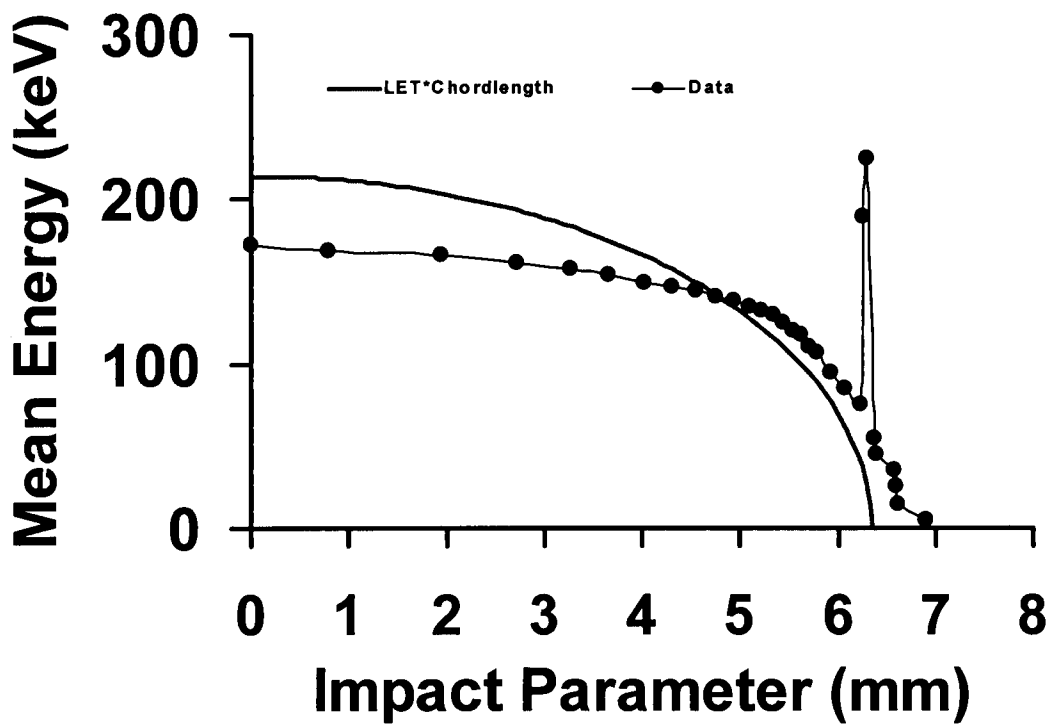

Figure 4-4. Energy deposition as a function of impact parameter for 360 MeV/nucleon Fe. Black filled circles: Mean energy deposited by 360 MeV/n Fe particles as a function of impact parameter. The line through the circles is to guide the eye. Black line: results obtained by multiplying the LET of 360 MeV/n ^{56}Fe ions by the chord length through the detector volume at the given impact parameter.

The solid black line represents a calculation where the energy deposition is given by (LET • chord length), where the chord length is a simple geometric function of impact parameter. In this calculation, energy deposition is maximal when the particle passes through the center of the sphere, and goes to zero when the impact parameter is equal to the radius of the sphere. For impact parameters near zero, the data show an average energy deposition that is about 20% less than this simple LET approximation. As the impact parameter increases, the data show greater energy deposition than this calculation yields, with a narrow peak just as the particle passes through the inside edge of the wall of the TEPC. Similar results were observed by Rademacher et al. for 1050 MeV/nucleon Fe (Rademacher et al., 1998).

As shown above, charged particle equilibrium was not achieved for Fe particles passing through the center of the TEPC. The data were analyzed to determine if energy deposition integrated over the complete response function was sufficient to provide a correct estimate of absorbed dose. This analysis was performed by calculating a parameter, Λ, for each experiment. Under conditions of CPE, the calculated value for Λ would be equal to the LET of the incident particles used in that experiment (Appendix E). This calculation took into account the projected surface area of the complete detector (cavity plus wall) rather than just the cavity, since there were many recorded events from particles that missed the cavity but passed through the wall. If Λ was equal to LET then the TEPC provided an accurate estimate of absorbed dose. The results shown in Table 4-1 and Fig. 4-5 indicate that Λ was within 6% of the numerical LET (Appendix E).

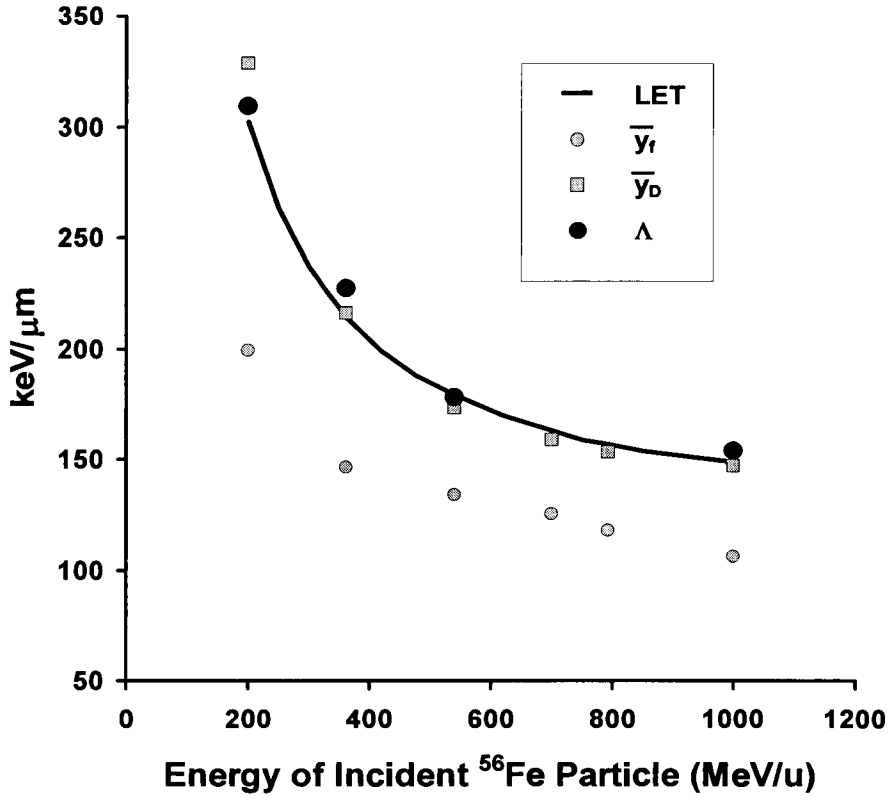

Figure 4-5. LET, mean lineal energy, $\overline{y}_f$, dose mean lineal energy, $\overline{y}_D$, LET computation results, Λ, for Fe particles at 200, 360, 540, 700, 790, 1000 MeV/n.

The energy deposition patterns in a TEPC are related to the LET of the incident heavy ions in a very complicated way. Using a TEPC to estimate quality factors has always been a desirable feature when applied to radiation protection dosimetry. To investigate this, the response functions were converted into distributions of lineal energy and used to determine frequency averaged lineal energy, $\overline{y}_f$, and dose averaged lineal energy, $\overline{y}_D$. The results are shown in Table 4-1 and Fig. 4-5. For the ideal case where energy deposition is (LET • chord length), $\overline{y}_f$, should be identical to LET. It can be seen that for Fe at these energies, measured values of $\overline{y}_f$ are consistently lower than LET due to the escape of electrons from the sensitive volume. However, $\overline{y}_D$ is always within 8% of LET (Appendix A).

We have computed a quality factor using the known LET of the monoenergetic ^{56}Fe beams (referred to as the *true* value in this work). We have also computed quality factors using data from the TEPC. In one case the quality factor, Q(L=y), was computed using the assumption that the distribution of LET was identical to the measured distribution f(y). In the second case, $Q(L=\overline{y}_D)$ was determined from only a single value of L assumed to be equal to $\overline{y}_D$ obtained from f(y). These results are shown in Fig. 4-6. For monoenergetic beams, Q(L=y) overestimated the true quality factor be as much as 20% whereas $Q(\overline{y}_D)$ was always within 4% of the true quality factor. The same computation was performed assuming a uniform mixture of ^{56}Fe particles at each of the six energies. For this case, Q(L=y) overestimated Q by 18% and $Q(\overline{y}_D)$ underestimated Q by 3% (Appendix A).

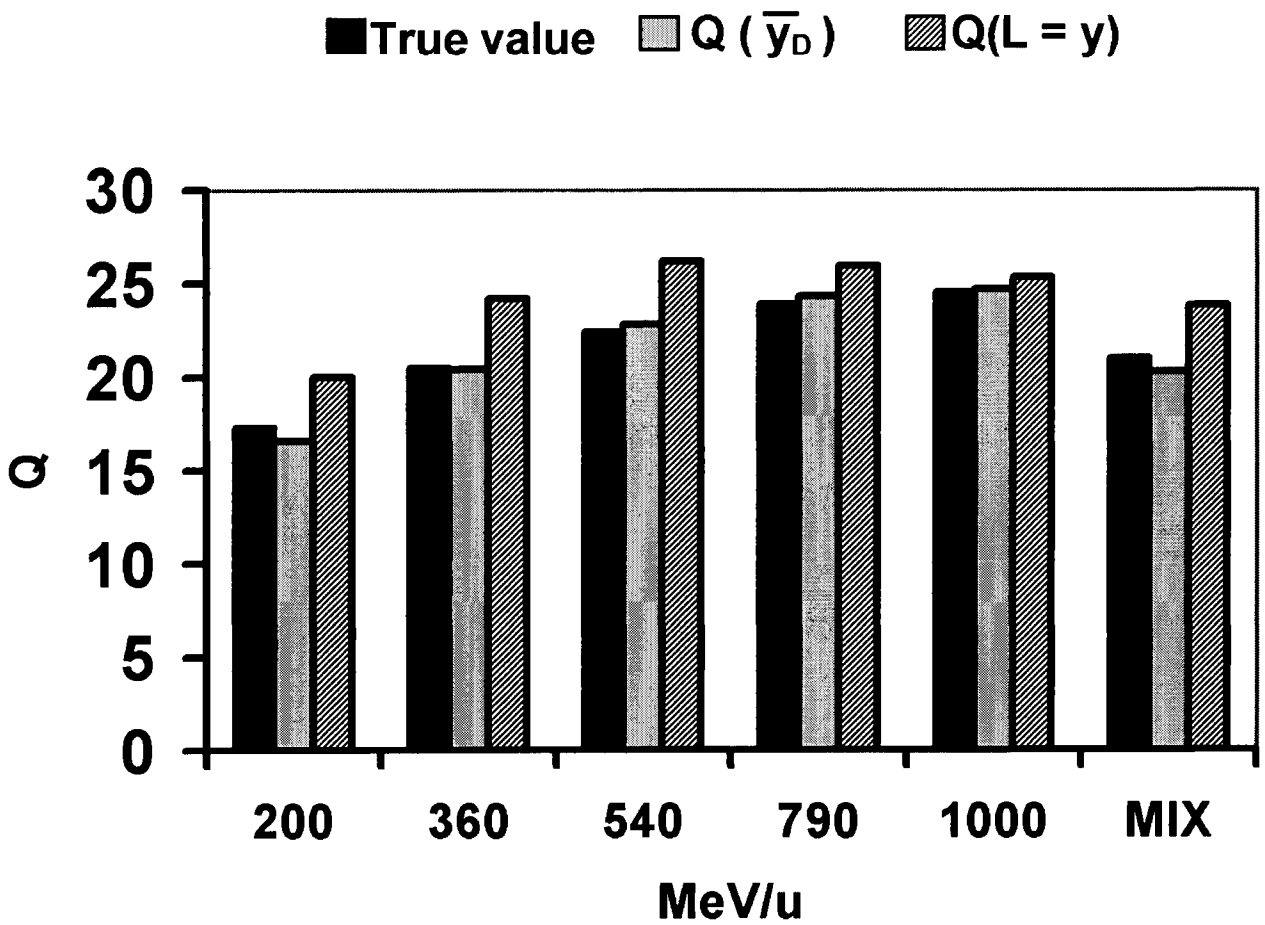

Figure 4-6. Bar graph showing true quality factor Q in black, results of calculations assuming Q(L=$\overline{y}_D$) in gray, and results of calculations assuming Q(L=y) in stripes for six energies of Fe.

Modeling Results

Figure 4-7 contains the same information as Figure 4-4, but in addition it contains modeling results. The dashed gray line in Fig. 4-7 shows a calculation of energy deposition in a homogeneous medium using the radial track model of Cucinotta et al (Cucinotta et al., 1995). The model calculates that for zero impact parameter, more than 50% of the energy transferred by the ^{56}Fe ion escapes the 1-μm diameter sphere; in strong contrast to the data, which show about 20% losses.

The solid gray line in Fig. 4-7 represents energy deposition using the radial dose model for the heterogeneous geometry that takes into account the difference in density between the gas and the wall that surrounds the gas cavity. The spatial density of electrons generated in the wall is much higher than that of electrons generated in the gas, but the radial dimensions of the track are also reduced. The results of the model are similar to the homogenous case for small impact parameters, but the heterogeneous model calculates an enhancement in energy deposition near the edge of the sensitive volume, similar to that seen in the data. This analysis was repeated for all energies and the results are summarized in Table 4-2.

The spatially restricted LET equation was applied to calculate energy deposition by ^{56}Fe particles having impact parameter equal to zero (Xapsos, 1992). This model requires homogeneous conditions between the volume of interest and the surrounding medium. These conditions were not present in the series of experiments described in this paper. However, the model was applied as if the wall of the

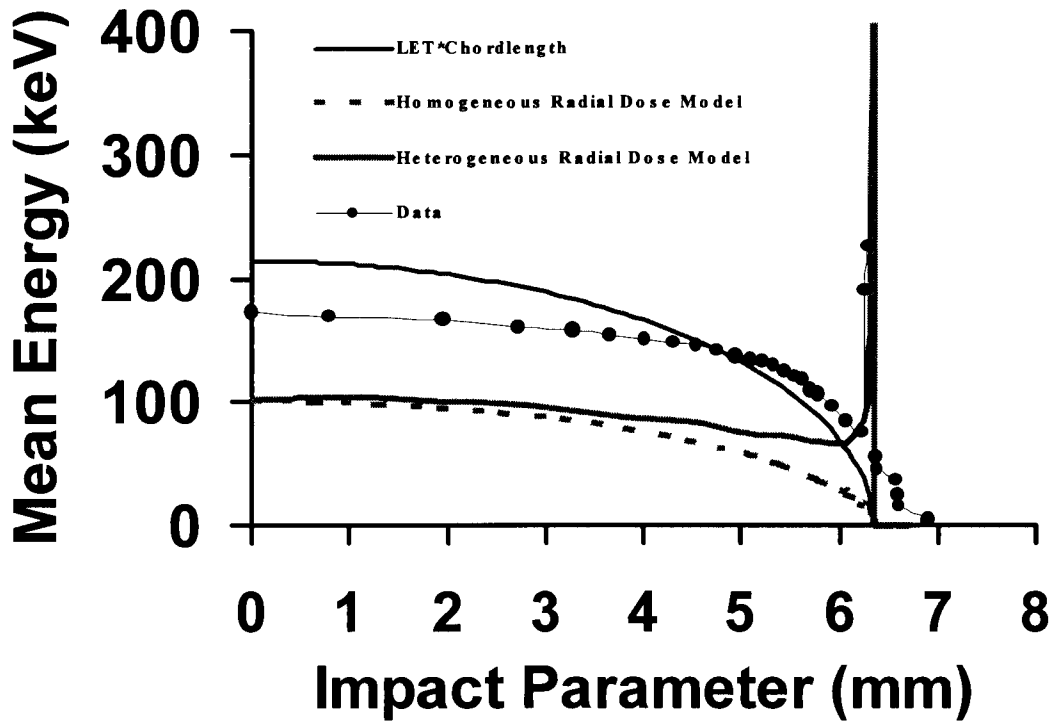

Figure 4-7. Further calculations of Energy deposition as a function of impact parameter for 360 MeV/nucleon Fe. Black filled circles: Mean energy deposited by 360 MeV/u Fe particles as a function of impact parameter. The line through the circles is to guide the eye. Dashed gray line: results of calculations performed using the radial dose model (17) assuming homogeneous conditions between the TEPC cavity and wall. Solid gray line: results of calculations performed using the radial dose model assuming heterogeneous conditions existing between the TEPC cavity and wall. Black line: results obtained by multiplying the LET of 360 MeV/u ^{56}Fe ions by the chord length through the detector volume at the given impact parameter.

Table 4-2

Summary of Data and Model Calculations for ^{56}Fe.

^{56}Fe Beam Energies (MeV/nucleon)	LET of ^{56}Fe Particles (keV/μm)	Energy Deposited for Events with Impact Parameter = 0-mm (keV)			
		Data Mean (FWHM)	Radial Dose Model Mean	SpatiallyRestricted LET Mean	BTC4 Model Mean
200	302	254(35)	148	242	274
360	214	173(28)	101	167	176
540	179	136(24)	83	138	137
700	163	127(19)	74	124	119
790	157	117(13)	71	119	112
1000	149	116(12)	65	112	102

TEPC had the same density as the gas in the active volume of the TEPC. Results from these calculations are found in Table 4-2 and Figure 4-8. The calculated energy deposition results are within 5% of the experimental results for each of the six energies of ^{56}Fe.

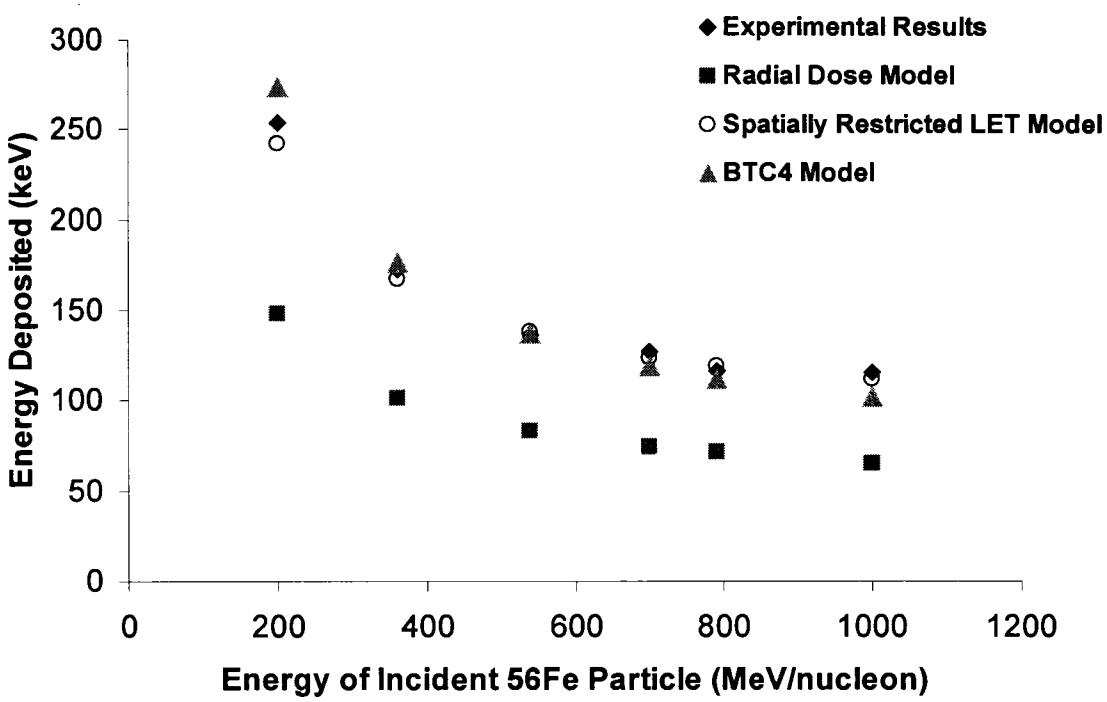

Figure 4-8. Energy deposited in TEPC by particle events with impact parameter equal to zero. Black filled diamonds: experimental results. Gray filled squares: results of radial dose model calculations. Open black circles: results of spatially restricted LET equation. Gray filled triangles: results from BTC4 code calculations.

The spatially restricted LET model also includes a means to calculate the distribution of energy deposition for particle events traversing the volume of interest. In this model, energy depositions by particle events follow a 2-parameter lognormal distribution (Appendix B). The results of the calculation for energy deposition with

the associated distribution for 360 MeV per nucleon Fe events with impact parameter equal to zero are found in Figure 4-9. This distribution is compared to the experimental results of energy deposited in the TEPC by 360 MeV per nucleon Fe particles found in Figure 4-1.

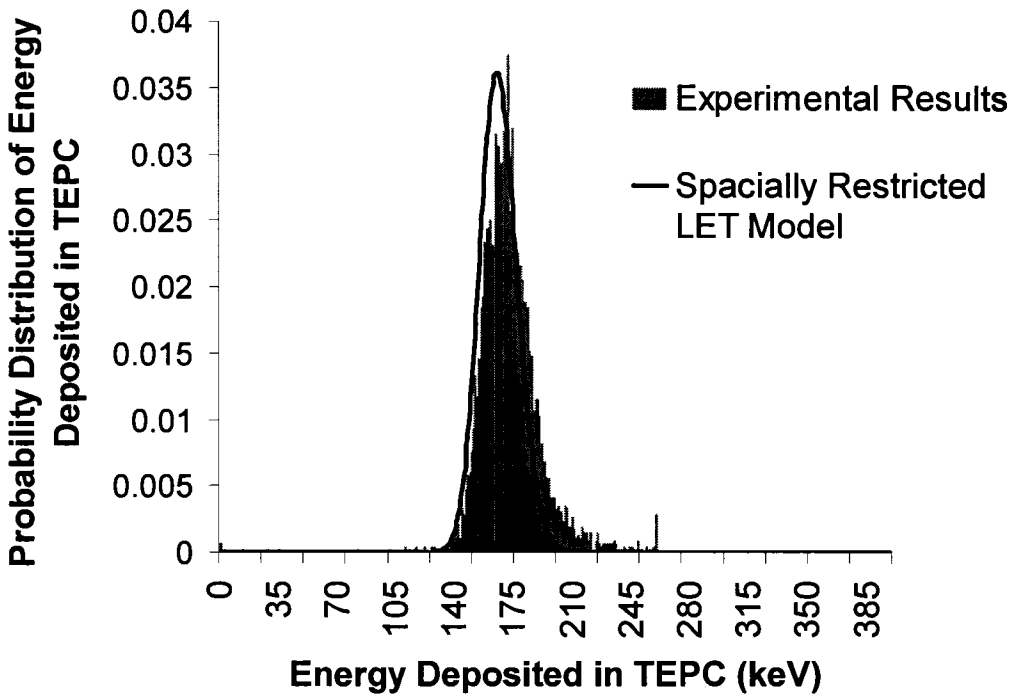

Figure 4-9. Gray bars: distribution of energy deposited in the TEPC by 360 MeV/n Fe particles with impact parameters less than 0.5-mm. Black line: distribution of energy deposited in the TEPC by 360 MeV/n Fe particles with impact parameters equal to 0-mm as calculated by the spatially restricted LET equation.

Track structure models were combined in a computer code named BTC4. This code was designed to calculate the mean energy deposition in the TEPC of a particle event with impact parameter equal to zero. Details of the track structure models used and the calculation itself are found in Appendix D. This code was specifically

designed to take into account the heterogeneity of densities between the TEPC wall and the TEPC gas cavity (active volume). Results from this set of calculations are found in Table 4-2 and Figure 4-8. The model calculates energy deposition to within 13% of the experimental results for each of the six energies of ^{56}Fe.

The spatially restricted LET equation can be used to calculate energy deposition (along with an associated distribution of energy deposition) for any particle traversal through the active volume of the TEPC. Energy deposition distributions were calculated corresponding to a uniform irradiation of the TEPC active volume. These distributions were then combined to form a probability distribution of energy deposited in the TEPC for a uniform irradiation by ^{56}Fe particles at six energies. The details of these calculations are found in Appendix B. Figure 4-10 shows the results of this calculation for 360 MeV per nucleon Fe particles superimposed on the experimental results shown in Figure 4-2. These probability distributions were used to calculate $\overline{y}_f$ and $\overline{y}_D$ values and the results are summarized in Table 4-3. The spatially restricted LET values for $\overline{y}_f$ and $\overline{y}_D$ are within 19% of the experimental results in all cases.

The results from the spatially restricted LET equation differ noticeably from the experimental results in Figure 4-10. An explanation of these differences is found in Chapter 5 and Appendix B.

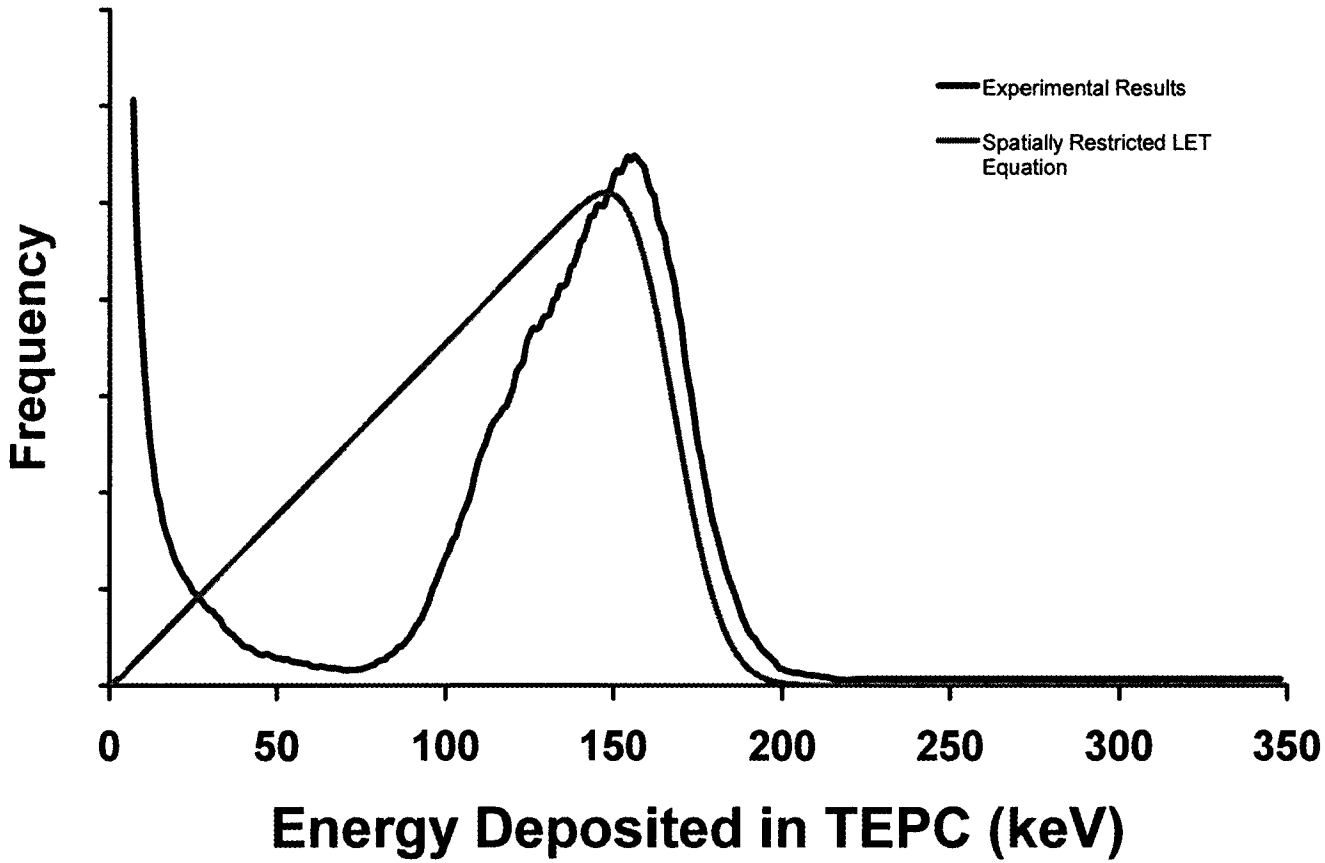

Figure 4-10. Black line: probability distribution of energy deposited in the TEPC by 360 MeV/n Fe particles. Gray line: probability distribution of energy deposited in the TEPC by 360 MeV/n Fe particles as calculated by the spatially restricted LET equation.

Table 4-3
Comparison of Data Calculations for ^{56}Fe with Model Calculations

^{56}Fe Beam Energies (MeV/nucleon)	LET of ^{56}Fe Particles (keV/μm)	Data		Spatially Restricted LET Equation	
		$\bar{y}_f$	$\bar{y}_D$	$\bar{y}_f$	$\bar{y}_D$
200	302	199	328	245	276
360	214	146	216	170	191
540	179	134	173	140	158
700	163	125	159	126	143
790	157	118	153	121	137
1000	149	106	147	113	129

CHAPTER V – DISCUSSION

Particle Events with Impact Parameter Equal to 0-mm

I. Radial Dose Model

Experiments were performed at particle accelerator facilities that provided an exposure of a ½" TEPC simulating a 1-μm diameter sphere of tissue to ^{56}Fe particles at six different energies. Plots of energy deposition in the TEPC by ^{56}Fe particles as a function of impact parameter were calculated for these experiments. As shown in Figure 4-7 (calculated from 360 MeV per nucleon Fe data), particle events with an impact parameter of zero deposited approximately 81% of what would be expected if there were no radial energy lost in the TEPC active volume (LET = 214 keV/μm). The radial dose distribution model calculation (Figure 4-7, Table 4-2) result determined that the particles would deposit 50% of LET in the chamber. This difference may be attributable to delta rays generated in the front wall of the detector that enter the sensitive volume and contribute to the measured energy distribution – the radial model does not include this forward component of electrons (Figure 5-1). If this is the case, it follows that the enhancement of delta rays from the forward wall

does not fully compensate for the delta rays that escape the sensitive volume. Thus for these events, charged particle equilibrium is not achieved.

Two other models were used to calculate energy deposition in the TEPC chamber by particle events with an impact parameter equal to 0-mm. They were the spatially restricted LET equation and the BTC4 code. The results from both of these model calculations agreed with the experimental results more closely than the radial dose distribution model. However, the mechanisms of energy deposition in these two models were fundamentally different.

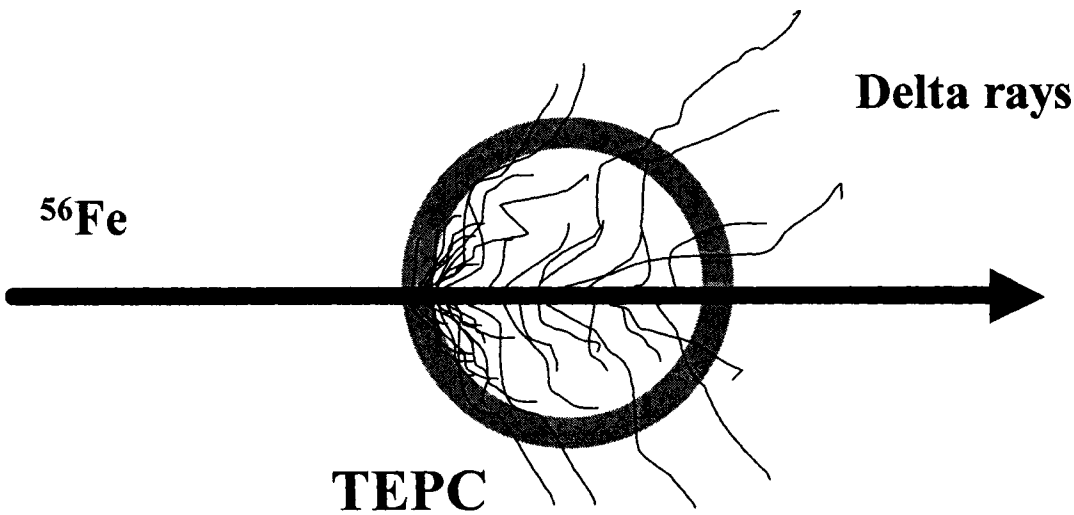

Figure 5-1. Illustration showing ^{56}Fe particle track traversing TEPC wall and cavity at impact parameter equal to 0-mm. Thin black lines illustrate electron (delta rays) tracks after the electrons were ejected from the ^{56}Fe particle track.

II. Spatially Restricted LET Equation

One model was the spatially restricted LET equation. This model was a radial energy distribution model. This model assumed homogeneous conditions surrounding the volume of interest, and it further assumed that energy was deposited from the particle track in a radial direction only. This equation calculates both the mean energy deposited for a given particle traversal of the active TEPC volume, and the distribution of this energy deposition. In the case of 360 MeV per nucleon ^{56}Fe, the mean energy deposition result underestimated the mean of the experimental results by less than 3.5% for particle events with an impact parameter of 0-mm. For each of the other five experiments, the model results were within 5% of the experimental results for particle events with an impact parameter of 0-mm. Further, the 2-parameter lognormal distribution of energy deposition of the model result follows the general trend of the data (Figure 4-9) for particle events with an impact parameter of 0-mm.

Since this model was not designed to take heterogeneous conditions between the TEPC wall and gas cavity into account, the calculations made with it were applicable to a TEPC with a wall having the same density as the gas cavity. Dosimeters with such a design are called wall-less TEPCs and have been subjected to intense experimental characterization by high-energy heavy ions. In an experiment by Rodgers et al., a wall-less TEPC was found to have a dose mean lineal energy response that was 30% less than a walled TEPC when both were exposed to a 278 MeV per nucleon Nitrogen beam (Rodgers et al., 1973). The spatially restricted LET equation calculation result for energy deposition of a particle at an impact parameter

equal to zero is identical under both walled and wall-less TEPC conditions. The model result therefore has a potential error of approximately 30% in one of the cases. These experimental results coupled with the homogeneous conditions in the model assumptions lead to the conclusion that the spatially restricted LET equation is in fact overestimating the energy deposited in a wall-less TEPC by 30%.

The 2-parameter lognormal distribution of energy deposition calculated by the spatially restricted LET equation follows the general trend of the data. This result is not at all surprising; energy loss straggling by high-energy heavy ions is frequently modeled using a lognormal distribution (Wilson and Paretzke, 1994). The reason that a lognormal distribution is applicable in this situation is that the ion loses a random fraction of the energy that it possesses during each collision in the TEPC wall and chamber. This random amount of energy loss is proportional to the amount of energy the ion possessed before the collision. Under these circumstances, energy loss may be modeled using the lognormal distribution (Shinn et al., 1999a).

Results from the spatially restricted LET equation were in close agreement to the mean energy deposited for particle events with impact parameter equal to zero in the six experiments. The 2-parameter lognormal distribution fits the distribution of the data from these six experiments well. These results might lead us to conclude that the spatially restricted LET equation can explain the energy deposition mechanisms in a walled TEPC. The reason that this would be an incorrect conclusion is that the results from this model are for homogeneous conditions existing between the TEPC wall and gas cavity. In order to conclude that the energy deposition mechanisms in this model are correct, we would have to accept the result of the model that energy

deposition in a 1-μm diameter simulated sphere of tissue by a high energy heavy ion is identical under walled and wall-less conditions. This result is clearly contradicted by experimental results.

III. BTC4 Code

Another model was the BTC4 computer code that used three track structure models to calculate the energy deposition of a heavy charged particle with an impact parameter equal to 0-mm in the TEPC. The BTC4 model was designed to only calculate energy deposition by heavy charged particles that had an impact parameter of 0-mm. This model assumed heterogeneous conditions existing between the TEPC wall and gas cavity. This model calculated the energy deposition in the TEPC active volume by heavy charged particles while the particle track was both outside and inside of the active volume (as illustrated in Figure 5-1). In the case of 360 MeV per nucleon ^{56}Fe with impact parameter of 0-mm, the mean energy deposition result overestimated the mean of the experimental results by less than 2%. For each of the other five experiments (also ^{56}Fe with impact parameter of 0-mm), the model result was within 13% of the experimental results.

Table 5-1 shows the BTC4 code results of total energy deposited in the TEPC by ^{56}Fe at six energies. Table 5-1 further contains a breakdown of the amount of energy deposited in the TEPC by the ^{56}Fe particle while the particle track was outside and inside the TEPC active volume.

The BTC4 model results indicate that 30-38% of the total energy deposited in the TEPC active volume by ^{56}Fe at these six energies was due to electrons that are generated in the wall of the TEPC. This result is in agreement with the 30% difference in dose mean lineal energy between walled and wall-less detectors as found by Rodgers et al. (Rodgers et al., 1973).

When the impact parameter of a particle is equal to 0-mm, the radial dose distribution model is defined only while the particle track is inside of the TEPC active volume. For this case, a comparison was made of the results of the radial dose distribution model, and of the BTC4 model results when the particle track was inside of the TEPC active volume (no contribution from the wall) (Table 5-1). These two sets of results agree to within 14% over the range of energies found in Table 5-1.

Table 5-1
Energy Deposited in TEPC for Events with Impact Parameter = 0-mm

^{56}Fe Beam Energies (MeV/nucleon)	BTC4: Energy Deposited in Cavity While ^{56}Fe Particle Traversing TEPC Front Wall (keV)	BTC4: Energy Deposited in Cavity While ^{56}Fe Particle Traversing TEPC Gas Cavity (keV)	Radial Dose Model: Energy Deposited in Cavity While ^{56}Fe Particle Traversing TEPC Gas Cavity (keV)
200	105	169	148
360	64	112	101
540	46	91	83
700	38	81	74
790	35	77	71
1000	31	71	65

Particle Events at All Impact Parameters

The radial dose distribution model was used to calculate the energy deposited by ^{56}Fe particle tracks at impact parameters other than zero. Figure 4-7 contains results from calculations performed with the radial dose distribution model under two different assumptions. These two assumptions were homogeneous and heterogeneous conditions surrounding active TEPC volume. The vertical difference on this graph between these two results constitutes the enhancement of energy deposition in a radial direction caused by the particle traversing the wall and ejecting delta rays into the gas cavity.

I. Distribution of TEPC Energy Response

The probability distributions of energy deposited in the TEPC had virtually identical characteristics for each of the six experiments. Figure 5-2 illustrates the six probability distributions in the form of cumulative distribution functions (CDFs).

Figure 5-3 shows the probability distribution for energy deposited in the TEPC by 360 MeV per nucleon Fe particles overlaid onto a triangular distribution. This triangular distribution is the chord length distribution of a uniform irradiation of a sphere where the chord length is multiplied by the LET of a 360 MeV per nucleon Fe particle. This resulting triangular distribution would be the energy deposition distribution for a spherical TEPC simulating 1-μm diameter of tissue if all of the energy from the particle was deposited locally (no radial loss or enhancement). The

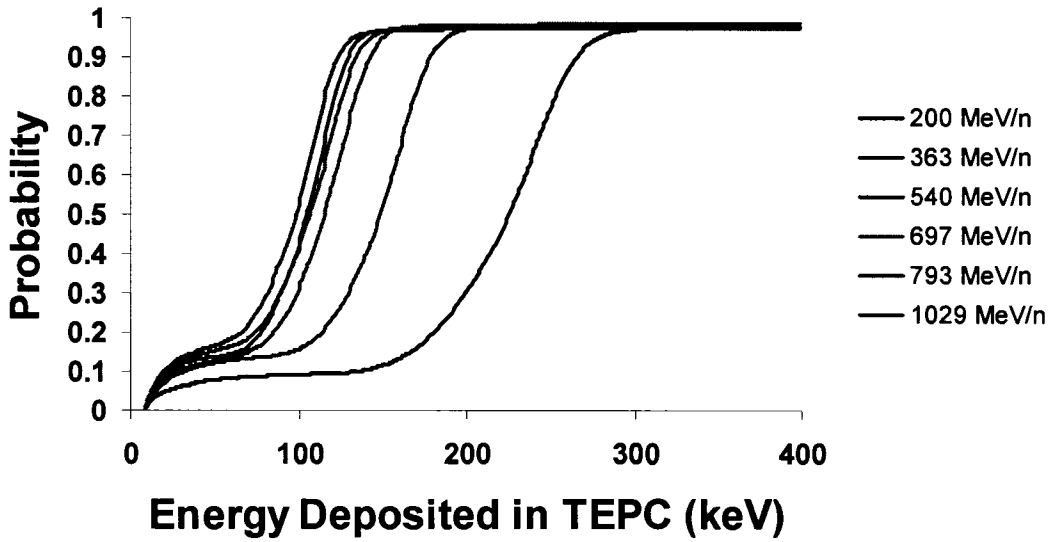

Figure 5-2. Probability distributions of energy deposited in the TEPC for six different energies of Fe. Distributions are presented in the form of Cumulative Distribution Functions (CDFs).

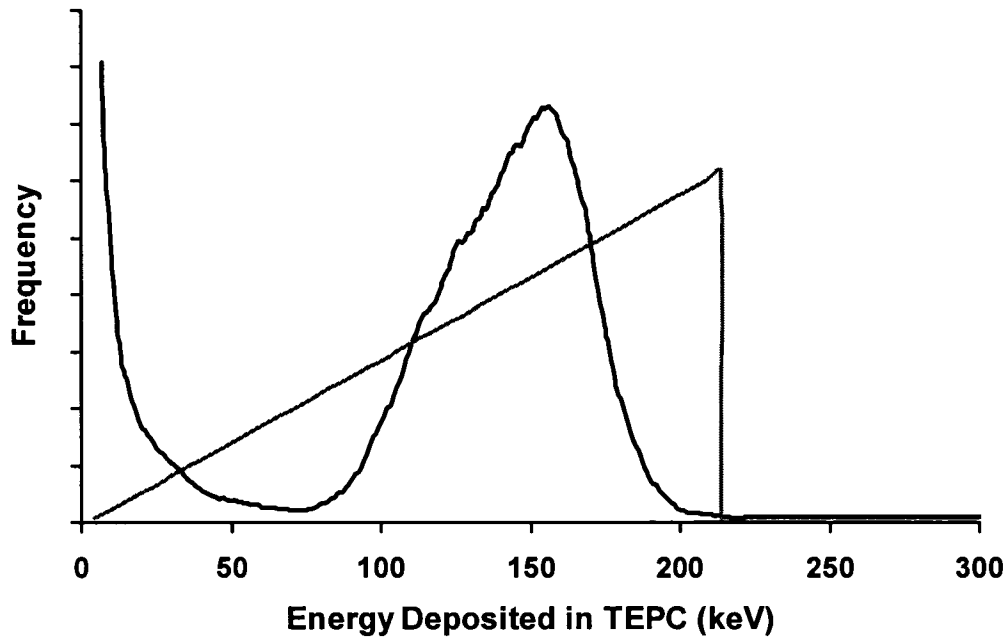

Figure 5-3. Black line: probability distribution (response function) of energy deposited in the TEPC by 360 MeV per nucleon Fe particles. Gray line: probability distribution of a μ-random irradiation of a sphere with each given chord length multiplied by the LET of 360 MeV per nucleon Fe.

distribution of the experimental data is similar to the triangular distribution, but there are marked differences.

The spatially restricted LET equation was used to model this energy deposition distribution. The results of this calculation (found in Figure 4-10) show a similarity to both the triangular distribution and the data distribution in Figure 5-3. There are noticeable differences however, between the results from the spatially restricted LET equation and the experimental results in Figure 4-10.

The spatially restricted LET equation does not calculate energy deposition by particle tracks that occur outside the active volume of the TEPC. Therefore the large numbers of low energy deposition events seen in the data distribution below 50 keV are missing in the calculated results.

In the energy deposition region above 50 keV and below 200 keV there is a clear difference in shapes of the data distribution and the calculated distribution. The spatially restricted LET equation does not calculate enhancement of the energy deposition in the TEPC active volume by particle tracks while they are traversing the front wall of the TEPC. This energy enhancement causes the slope of the data distribution to be steeper than the slope of the calculated distribution in the energy region between 50 keV and 150 keV. This same energy enhancement causes the magnitude of the data distribution to be lower than the calculated distribution in the region between 50 keV and 150 keV, and the magnitude of the data distribution to be higher than the calculated distribution in the region between 150 keV and 200 keV. This energy enhancement caused by the particle tracks while the tracks are in the

front wall of the TEPC is discussed in the following section in this chapter titled Explanation of TEPC Response Distribution Anomalies.

In the energy deposition region above 200 keV, the data distribution contains a small number of events, while the distribution calculated with the spatially restricted LET equation does not contain any. The spatially restricted LET equation does not calculate enhancement of the energy deposition in the TEPC active volume by particle tracks that either graze the TEPC wall at impact parameters near 6.35-mm, or strike the TEPC anode wire. These types of events were shown in Figures 4-2 and 4-3 to deposit energy above 200 keV in the TEPC active volume.

II. Explanation of TEPC Energy Response Distribution Anomalies

The graphs in Figures 5-4 and 5-5 are derived from data from the 360 MeV per nucleon Fe experiment. Results from each of the other five experiments are similar in the characteristics discussed below. A combination of the interpretation of experimental results and the application and interpretation of track structure modeling was used to understand the deviation of the experimental data from the idealized conditions as illustrated in Figure 5-3.

Figure 5-4 is divided into four regions: $\delta_1, \delta_2, \delta_3, \delta_4$. Figure 5-5 is also divided into four regions: $\delta_1, \delta_2, \delta_3, \delta_4$. These four regions as delineated in the graphs are related and illustrate the following findings.

In region δ_1 of Figure 5-4, the mean energy deposited in the detector by the Fe particles is consistently less than the product of the LET of the Fe particles and the

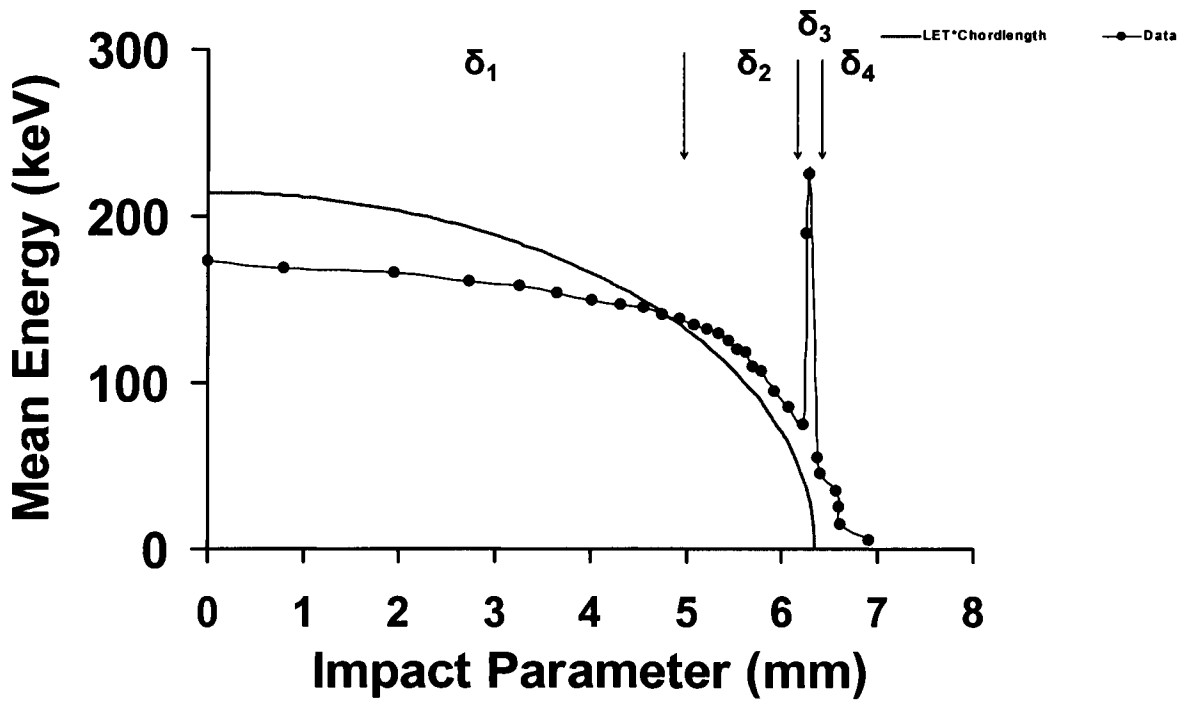

Figure 5-4. Distribution anomalies graph a. Black filled circles: Mean energy deposited by 360 MeV per nucleon Fe particles as a function of impact parameter. The line through the circles is to guide the eye. Black line: results obtained by multiplying the LET of 360 MeV/n ^{56}Fe ions by the chord length through the detector volume at the given impact parameter. The figure is divided into four regions: $\delta_1, \delta_2, \delta_3, \delta_4$. Explanation of the significance of these regions is found in the text.

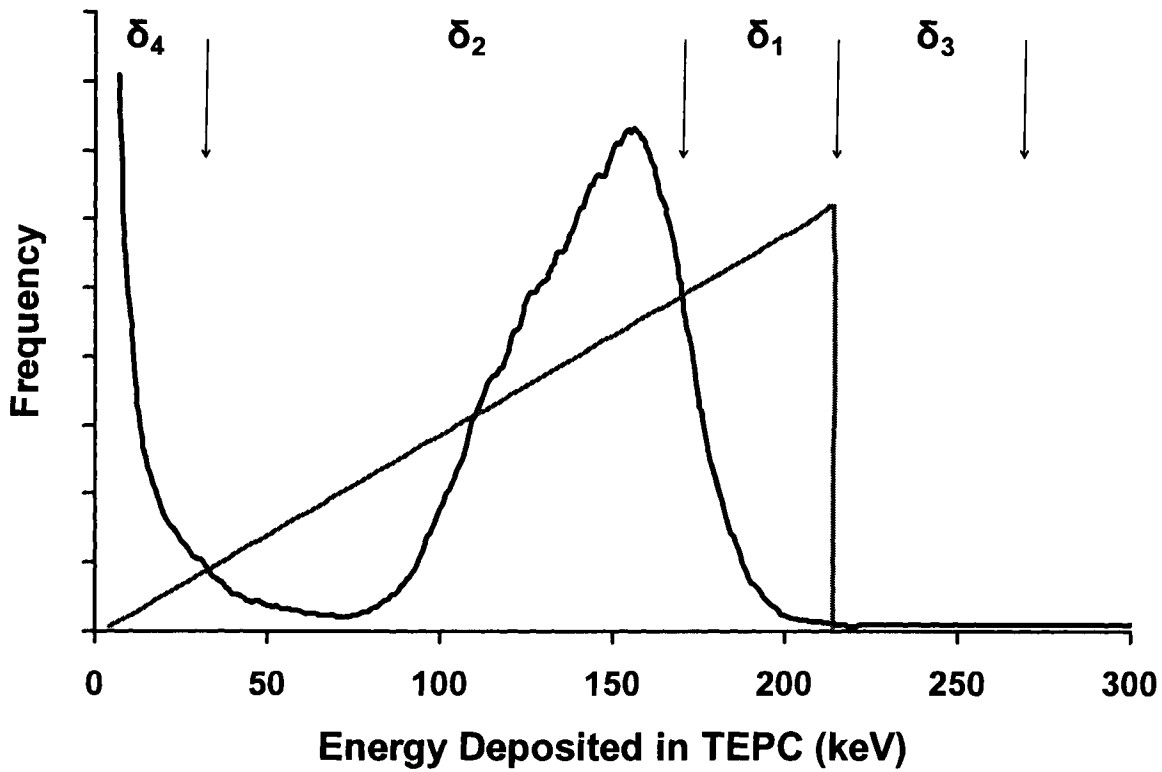

Figure 5-5. Distributions anomalies graph b. Black line: response function in the form of a probability distribution of energy deposited in the TEPC by 360 MeV per nucleon Fe particles. Gray line: probability distribution of a μ-random irradiation of a sphere with each given chord length multiplied by the LET of 360 MeV per nucleon Fe.

chordlength of the Fe particles through the detector at the given impact parameter. Modeling results by the radial dose distribution model and the BTC4 code explained this shift as being a combination of radial energy loss from the particle track (while it was in the active volume) and enhancement of energy deposition by the particle track while it was in the TEPC wall outside the active volume. In region δ_1 in Figure 5-5 this same phenomenon is illustrated by a shift down in energy of the main distribution of the experimental results as compared to the triangular distribution calculated by the product of the LET and chordlength through the detector of the Fe particles.

In region δ_2 of Figure 5-4, the mean energy deposited in the detector by the Fe particles was consistently higher than the product of the LET of the Fe particles and the chordlength of the Fe particles through the detector at the given impact parameter. Modeling results of the radial dose distribution model explained this result in this region as being caused by enhanced energy deposition by the particle track while the track was within the TEPC wall (Figure 4-7). In region δ_2 of Figure 5-5, this same effect is illustrated as a shift in the number of events from lower energies (data curve below the LET and chordlength distribution) to higher energies (data curve above the LET and chordlength distribution).

In region δ_3 of Figure 5-4 the mean energy deposited in the detector by the Fe particles was higher than the LET and chordlength value for any possible chordlength of a particle through the detector. Modeling results of the radial dose distribution model as well as Region C in Figure 4-3 showed that the results in

this region were due to Fe particles that struck the TEPC anode wire or grazed the cavity-wall interface. In region δ_3 of Figure 5-5 this effect is illustrated in the tail of the TEPC response function above the LET and chordlength triangular distribution.

Particle events in region δ_4 of Figure 5-4 had impact parameters greater than the TEPC active volume. Events in this region were shown in Figure 4-3 Region B (three dimensional histograms of data) to be particles that missed the active volume of the detector and only traversed the detector wall. In region δ_4 of Figure 5-5 these events are seen as a large number of events with low amount of energy deposition in the TEPC.

III. Absorbed Dose Determination

Important applications of TEPCs are to determine absorbed dose of the mixed radiation field found in a space vehicle during a mission. Calculations were performed to determine if the TEPC gave an accurate assessment of absorbed dose during exposure to ^{56}Fe particles at energies found in Table 5-1. The term Λ was introduced as a quantity that is equal to LET if the TEPC is accurately determining absorbed dose. It was found that Λ was within 6% of the LET value for each of the six experiments, and so it was concluded that the TEPC is indeed capable of determining absorbed dose (Appendix E).

IV. Average Values of TEPC Energy Deposition Response Functions

The energy deposition spectrum in Figure 5-3 can be converted to a lineal energy spectrum by dividing the energy value of each probability (frequency) by the average chord length through the detector (Appendix A). After conversion to a lineal energy spectrum, the frequency mean ($\overline{y}_f$) of the triangular distribution in Figure 5-3 is equal to 214 keV per μm. This is equal to the LET of the incident 360 MeV per nucleon Fe particle. Given the marked differences between the experimental data response function and the idealized triangular distribution, it is not surprising that the frequency mean $\overline{y}_f$ of the data distribution is not equal to LET. In fact, the value of $\overline{y}_f$ consistently underestimates the LET of incident particles for all six of the experiments. The dose mean lineal energy $\overline{y}_D$ value however is always within 8% of LET.

The spatially restricted LET model was used to calculate response functions for ^{56}Fe ions incident upon a spherical TEPC simulating a 1- μm diameter volume of tissue (Appendix B). Values of $\overline{y}_D$ and $\overline{y}_f$ were calculated from these response functions. Results of these calculations are found in Table 4-3. The values for $\overline{y}_f$ calculated from the model were all within 19% of the values calculated from the experimental data for each of the six experiments. The model values were consistently higher than the experimental results. The values for $\overline{y}_D$ calculated from the model were also all within 19% of the values calculated from the experimental data for each of the six experiments. The model values for $\overline{y}_D$

were consistently lower than the experimental results. Ratios of the experimental values and the model calculation values of $\overline{y}_f$ and $\overline{y}_D$ are found in Figure 5-6.

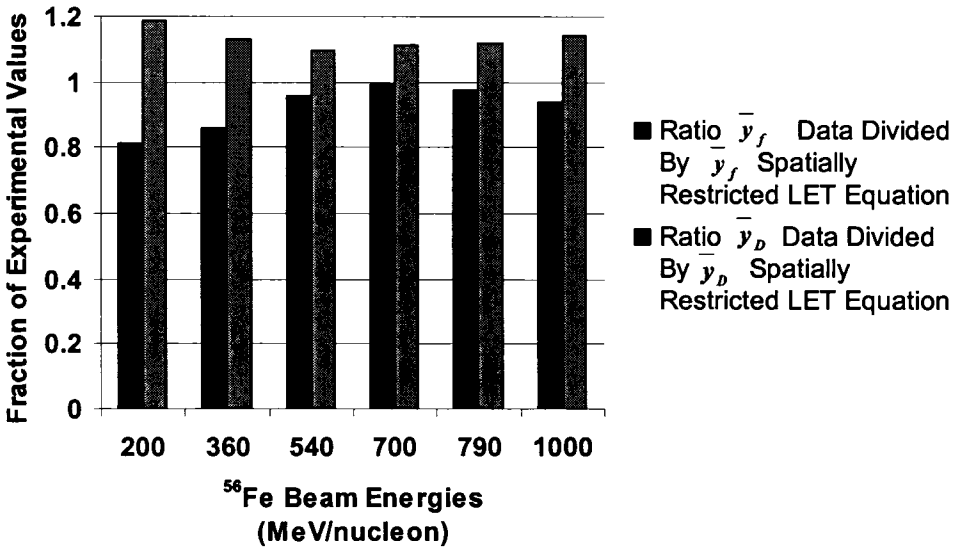

Figure 5-6. Bar graph illustrating the ratio of the experimental values and the model calculation values of $\overline{y}_f$ and $\overline{y}_D$.

Unfortunately because of the model's assumption of homogeneity between the TEPC gas cavity and the TEPC wall, as well as the fact that the model is not defined for particle track lengths outside the gas cavity there are marked differences between the model results and the shape of the experimental energy deposition spectrum.

V. Quality Factor Determination

TEPCs are used to determine an average quality factor ($\overline{Q}$) of the radiation field during space missions. This average quality factor is used to calculate the dose equivalent, and also to approximate a value of equivalent dose that is subsequently used to calculate effective dose (Appendix A). The value of the quality factor for high-energy heavy ions is dependent on the LET of the ion. When a TEPC is exposed to an unknown mixed radiation field consisting of ions that have different atomic numbers and energies, interpretation of the resulting energy deposition distribution is a complex problem. Two methods were used to determine the average quality factor of each of the six experimental energy deposition spectrums. The results from these two methods were then compared to the known quality factor that was determined using the known LET of the ^{56}Fe beam for each experiment (referred to as the *true* quality factor in this work). The method of determining average quality factor that assumed that Q(L=y) consistently overestimated the known quality factor. In one experiment, this overestimation was almost 20% above the known value. The second method for determining an average quality factor assumed that $Q(L=\overline{y}_D)$. This method was consistently within 4% of the known quality factor for each experiment (Figure 4-6).

Determination of an average quality factor for a radiation field is a critical part of the determination of the risk of exposure to radiation for astronauts. This average quality factor once determined is used to calculate a dose equivalent and an effective dose value assigned to an astronaut's dosimetry record. Any error

(too high or too low of a value) in the quality factor determination results in a change in this value of dose equivalent and effective dose. An underestimation of the dose equivalent or effective dose received by an astronaut could lead to an astronaut participating in more missions and therefore receiving more radiation exposure than is legally allowed. An overestimation of the dose equivalent or effective dose could be a factor in the premature ending of their space flight career. More research is needed in this area to insure that average quality factors calculated by the TEPC are correct.

CHAPTER VI – CONCLUSIONS

We have measured the response of a spherical tissue equivalent proportional counter to ^{56}Fe ion beams at several energies between 200 to 1000 MeV per nucleon. The experiments were performed at the AGS in Brookhaven National Laboratory in the US and at the HIMAC at the National Institute for Radiological Sciences in Japan. Particles were detected with a spectrometer that recorded the charge and position of each ion immediately upstream and downstream of the TEPC. Approximately 10^6 events were recorded for each experiment and analyzed off-line. The results reported here were for a uniform beam of Fe particles that entered and exited the detector without any charge-changing nuclear interactions. In all cases the gas pressure was regulated to simulate a sphere of tissue 1 μm in diameter.

The data at all energies indicated that track structure influences the pattern of energy deposition in the sensitive volume. For particles that pass through the center of the sphere, approximately 20% of the energy related to the LET escapes the 1μm diameter volume. A model describing the radial distribution of the track indicated that over 50% of the LET should escape this volume. This difference between the data and model is attributed to delta rays produced in the front wall of the detector that have sufficient forward momentum to enter the gas cavity and contribute to

energy deposition. Calculations performed with the BTC4 code support the hypothesis that the data contains elements of radial energy loss and energy enhancement from delta rays produced in the TEPC wall. However this delta ray enhancement from the forward wall is not sufficient to compensate for ionization electrons that escaped as the Fe particle passed through the sphere.

There is also a strong enhancement of events with very small energy depositions. These events originate from Fe particles that do not cross the sensitive volume but pass through the side-walls of the TEPC. Since the density of the wall is more than 10,000 times that of the gas cavity, there are many more electrons generated in the wall; however only a few of them have sufficient range to penetrate into the sensitive volume to produce a measurable energy deposition. Because the projected area of the wall is large, these events occur frequently and make a significant contribution to the response of the TEPC. These could easily be misinterpreted as incident particles with low LET.

When the trajectory of the Fe particle through the wall is very close to the inside boundary of the gas cavity, a large number of electrons enter the sensitive volume, producing a signal that resembles that produced by the passage of a high LET particle through the detector. Some of these events produce more than twice the energy deposited when the primary incident particle passes directly through the center of the sensitive volume. Results from the radial dose distribution model are consistent with these experimental observations.

One other class of events is generated when the incident Fe particle strikes the anode or grid wires of the TEPC. Since the high-density wires are very thin, many delta rays can escape into the gas and produce a large pulse.

In spite of the complicated response function, the detector does give a reasonably good estimate of absorbed dose. There seems to be sufficient enhancement of energy deposition from delta rays produced in the wall to compensate for high-energy delta rays that escape the spherical volume. Thus while charged particle equilibrium is not preserved on an event-by-event basis, it is preserved when the detector response is integrated over the complete response function that includes particles that do not pass through the sensitive volume.

A spherical TEPC does not make a direct measurement of LET for Fe particles at these energies and therefore such a TEPC should not be considered as an LET spectrometer. In the ideal case, the frequency-averaged lineal energy, $\overline{y}_f$, should be numerically equivalent to LET, but these data show that $\overline{y}_f$ is always significantly less than LET. However, dose averaged lineal energy, $\overline{y}_D$, does approximate LET. Computations of quality factor indicated that using the assumption that $\Phi(L)$ is identical to f(y) yields a value that overestimates the true quality factor by 20%. The quality factor determined from the dose averaged value of y, $\overline{y}_D$ is always within 4% of the true value. It could be argued that since radiation risks are not always known with high precision either method might be suitable for estimating dose equivalent. It will be necessary to collect data for other ions in order to confirm this hypothesis.

REFERENCES

Badhwar,G.D., Konradi, A. Hardy,A., Braby, L.A., Active Dosimetric Measurements On Shuttle Flights. Nucl. Tracks Radiat. Meas. 20, 13-20 1992.

Badhwar,G.D., Cucinotta, F.A., Braby, L.A., Konradi, A. Measurements on the Shuttle of the LET Spectra of Galactic Cosmic Radiation and Comparison with the Radiation Transport Model. Radiat Res. 139, 344-351 1994a.

Badhwar,G.D., Konradi, A., Braby, L.A., Atwell, W., Cucinotta, F.A., Measurements of Trapped Protons and Cosmic Rays from Recent Shuttle Flights. Adv. Space. Res. 14(10) 67-72 1994b.

Badhwar,G.D., Konradi, A., Atwell, W., Golightly, M.J., Cucinotta, F.A., Wilson, J.W., Petrov, V.M., Tchernykh, I.V., Shurshakov, V.A., Labakov, A.P., Measurements of the Linear Energy Transfer Spectra on the MIR Orbital Station and Comparison With Radiation Transport Models. Radiat. Meas. 26(2), 147-158 1996.

Badhwar,G.D., Patel, J.U., Cucinotta, F.A., Wilson, J.W. Measurements of the Secondary Particle Energy Spectra in the Space Shuttle. Radiat. Meas. 24, 129-138 1995.

Badhwar, G.D. The Radiation Environment in Low-Earth Orbit. Radiat Res. 148, S3-S10 1997.

Badhwar,G.D., Huff,H., Wilkins,R., Alterations in Dose and Lineal Energy Spectra under Different Shieldings in the Los Alamos High-Energy Neutron Field. Radiat Res. 154, 697-704 2000a.

Badhwar,G.D., Cucinotta,F.A., A Comparison of Depth Dependence of Dose and Linear Energy Transfer Spectra in Aluminum and Polyethylene. Radiat Res. 153, 1-8 2000b.

Benton, E.V., Collver,M.M, Registration of Heavy Ions During the Flight of Gemini VI. Health Phys. 13, 495-500 1967.

Benton, E.V., Peterson, D.D., Bailey, J.V., Parnell, T., High-LET Particle Exposure of Skylab Astronauts. Health Phys. 32, 15-19 1977.

Benton, E.V., Summary of Radiation Dosimetry Results on U.S. and Soviet Manned Spacecraft. Adv. Space Res. 6, 315-328 1986.

Chapman, P.L., "Applied Regression Methods." Applications of Probability and Statistics in Health Physics. Ed. T. Borak. Medical Physics Publishing, Madison, WI 2000.

Cucinotta, F.A., Katz, R., Wilson, J.W., Dubey, R.R., Heavy Ion Track-Structure Calculations for Radial Dose in Arbitrary Materials. NASA Technical Paper 3497. Hampton, VA. February 1995.

Cucintotta, F.A., Nikjoo, H., Goodhead, D.T., Model for Radial Dependence of Frequency Distributions for energy Imparted in Nanometer Volumes from HZE Particles. Radiat. Res. 153, 459-468 2000.

Cucinotta,F.A., Schimmerling,W.,Wilson,J.W., Peterson,L.E., Badhwar,G.D., Saganti,P.B., Dicello,J.F. Space Radiation Cancer Risk Projections For Exploration Missions: Uncertainty Reduction and Mitigation. JSC-29295. January 2001.

Dicello, J.F., Amols, H.I., Zaider, M., Tripard, G., A Comparison of Microdosimetric Measurements with Spherical Proportional Counters and Solid-State Detectors. Radiat Res. 82, 441-453 1980.

Dicello, J.F., Wasiolek, M., Measured Microdosimetric Spectra of Energetic Ion Beams of Fe, Ar, Ne, and C: Limitations of LET Distributions and Quality Factors in Space Research and Radiation Effects. IEEE Trans. Nucl. Sci. 38, 1203-1209 1991.

Doke, T., Hayashi, T., and Borak, T.B., Comparisons of LET Distributions Measured in Low Earth Orbit Using Tissue-Equivalent Proportional Counters and the Position Sensitive Si-Detector Telescope (RRMD-III). Accepted for publication Radiat Res. March 2001.

Gersey, B., Borak, T., Guetersloh, S., Zeitlin, C., Miller, J., Heilbronn, L., Murakami, T., Iwata, Y., The Response of a Spherical Tissue-Equivalent Proportional Counter to ^{56}Fe Particles from 200-1000 MeV/nucleon. Radiat Res. 157, 350-360, 2002.

Glass, W., Braby, L., A Wall-Less Detector for Measuring Energy Deposition Spectra. Radiat Res. 39, 230-240 1969.

International Commission on Radiation Units and Measurements, ICRU Report 16, Linear Energy Transfer, International Commission on Radiation Units and Measurements, Washington, 15 June 1970.

International Commission on Radiation Units and Measurements, ICRU Report 36, Microdosimetry, International Commission on Radiation Units and Measurements, Maryland, 31 December 1983.

International Commission on Radiation Units and Measurements, ICRU Report 51, Quantities and Units in Radiation Protection Dosimetry, International Commission on Radiation Units and Measurements, Maryland, 1 September 1993.

International Commission on Radiological Protection, ICRP Report 60, 1990 Recommendations of the ICRP, Annals of the ICRP 21 (1-3), Pergamon Press, New York, 1991.

Ito, A., Henkelman, R., Microdosimetry of the Pion Beam at TRIUMPH. Radiat. Res. 116. 183-195. 1988.

Johnson, A.S., Badhwar, G.D., Golightly, M.J., Hardy, A.C., Konradi, A.,Yang, T., Spaceflight Radiation Health Program at the Lyndon B. Johnson Space Center. NASA Technical Memorandum 104782. (1993).

Kliauga, P., Colvett, R.D., Goodman, L.J., Lam Y.M., Microdosimetry of 400 MeV/AMU ^{12}C and 450 MeV/AMU ^{40}Ar Beams. In Proceedings of the Sixth Symposium on Microdosimetry, (H.G. Ebert and J. Booz, Eds.), pp. 1173-1183. Harwood Academic Publishers Ltd., London, 1978.

Knoll G.F. "Radiation Detection and Measurement", John Wiley & Sons, New York 1979.

Kobetich, E.J., Katz, R., Electron Energy Dissipation. Nucl. Instr. And Meth. 71, 226-230 1969.

Luxton, G., Fessenden, P., Microdosimetric Measurements of Pretherapeutic Heavy Ion Beams. Radiat. Res. 79, 256-272 1979.

Metting, N.F., Rossi, H.H., Braby, L.A., Kliauga, P.J., Howard, J., Zaider, M., Schimmerling, W., Wong, M., Rapkin, M., Microdosimetry near the Trajectory of High-Energy Heavy Ions. Radiat Res. 116, 183-195 1988.

NCRP, Guidance on Radiation Received in Space Activities. Report 98, National Council on Radiation Protection and Measurements, Bethesda, MD, 1989.

NCRP, Radiation Protection Guidance for Activities in Low Earth Orbit. Report 132, National Council on Radiation Protection and Measurements, Bethesda, MD, 2000.

Rademacher, S.E., Borak, T.B., Zeitlin, C., Heilbronn, L., Miller, J., Wall Effects Observed in Tissue-Equivalent Proportional Counters from 1.05 Gev/nucleon Iron-56 Particles. Radiat Res. 149, 387-395 1998.

Rodgers, R.C., Dicello, J.F., Gross, W., The Biophysical Properties of 3.9-GeV Nitrogen Ions. Radiat Res. 54, 12-23 1973.

Rossi, H.H, Zaider, M., "Microdosimetry and Its Applications", Springer-Verlag, New York 1996.

Rudd, M.E., Differential Cross Sections for Secondary Electron Production by Proton Impact. Phys. Rev. A 38, 6129-6137 1988.

Rudd, M.E., User-Friendly Model for the Energy Distribution of Electrons from Proton or Electron Collisions. Nucl.Tracks Radiat. Meas., 16, 213-218 1989.

Rust, D.M. Solar Flares, Proton Showers, and the Space Shuttle. Science. 216, 939-946 1982.

Sakaguchi, T., Doke, T., Hasebe, N., Hayashi, T., Kashiwagi, T., Kikuchi, J., Kono, S., Nagaoka, S., Nakano, T., Takagi, T., Takahashi, K., Takahashi, S. LET Distribution Measurement with a New Real-Time Radiation Monitoring Device-III Onboard the Space Shuttle STS-84. Nucl. Instr. And Meth. A 437, 75-87 1999.

Shaefer, H.J., Sullivan, J.J., Richmond, R.G., Dosimetry of Proton Radiation Fields in Space with Nuclear Emulsions. Health Phys. 19, 663-670 1970.

Shinn, J.L., Badhwar, G.D., Xapsos, M.A., Cucinotta, F.A., Wilson, J.W., An Analysis of energy Deposition in a Tissue Equivalent Proportional Counter Onboard the Space Shuttle. Radiat, Meas., 30, 19-28 1999a.

Shinn, J.L., Wilson, J.W., Singleterry, R.C., Xapsos, M.A., Implications of Microdosimetry in Estimation of Radiation Quality in Space Environment. Health Phys. 76(5), 510-515 1999b.

Taylor, J.R., Zafiratos, C.D., "Modern Physics for Scientists and Engineers", Prentice- Hall, Englewood Cliffs, New Jersey 1991.

Turner, J.E., "Atoms, Radiation, and Radiation Protection," McGraw-Hill Inc., New York, 1992.

Wilson, J.W., Townsend, L.W., Schimmerling, W., Khandelwal, G.S, Khan,F., Nealy, J.E., Cucinotta, F.A., Simonsen, L.C., Shinn, J.L., Norbury, J.W. Transport Methods and Interactions for Space Radiations. NASA Reference Publication 1257, Washington D.C. 1991.

Wilson, J.W., Miller, J., Konradi, A., Cucinotta, F.A., Shielding Strategies for Human Space Exploration. NASA Conference Publication 3360. December 1997.

Wilson, J.W., Kim,M., Schimmerling,W., Badavi,F.F., Thibeault,S.A., Cucinotta,F.A., Shinn,J.L., Kiefer,R. Issues in Space Radiation Protection: Galactic Cosmic Rays. Health Phys. 68(1), 50-58 1995.

Wilson, W.E., Paretzke, H.G., A Stochastic Model of Ion Track Structure. Radiat. Prot. Dosim. 52(1-4), 249-253 1994.

Wong, M., Schimmerling, W., Phillips, M. H., Ludewigt, B. A., Landis, D.A., Walton, J.T., Curtis, S.B., The Multiple Coulomb Scattering of Very Heavy Charged Particles. Med. Phys. 17(2),163-171 Mar/Apr 1990.

Xapsos, M.A., A Spatially Restricted Linear Energy Transfer Equation. Radiat. Res. 132, 282-287 1992.

Xapsos, M.A., Burke, E.A., Shapiro, P., Summers, G.P., Energy Deposition and Ionization Fluctuations Induced by Ions in Small Sites-An Analytical Approach. Radiat. Res. 137, 152-161 1994.

Xapsos, M.A., Burke, E.A., Shapiro, P., Summers, G.P., Probability Distributions of Energy Deposition and Ionization in Sub-Micrometer Sites of Condensed Media. Radiat. Meas. 26, 1-9 1996.

Yasuda, H., Badhwar, G.D., Komiyama, T., Kazunobu, F., Effective Dose Equivalent on the Ninth Shuttle-Mir Mission (STS-91). Radiat. Res. 154, 705-713 2000.

APPENDIX A

HEALTH PHYSICS AND MICRODOSIMETRY TERMINOLOGY

According to International Commission on Radiation Units and Measurements (ICRU) report 51 titled Quantities and Units in Radiation Protection Dosimetry, the fundamental dosimetric quantity is the absorbed dose, D.

Absorbed dose, D, is the quotient of $d\bar{\varepsilon}$ by dm, where $d\bar{\varepsilon}$ is the mean energy imparted by ionizing radiation to matter of mass dm (ICRU, 1993).

$$D = \frac{d\bar{\varepsilon}}{dm} \quad \text{Unit: J kg}^{-1} \qquad \text{Equation A.1}$$

The name for the unit of absorbed dose is gray (Gy).

ICRU Report 16 defines Linear Energy Transfer (LET) as the unrestricted stopping power of a particle traversing a medium of interest. LET is calculated as the quotient of dE by dx, where dE is the average energy lost by the particle, due to collisions with electrons in the medium of interest, and dx is the distance traversed in the medium of interest by the particle.

$$L = \frac{dE}{dx} \quad \text{Unit: J m}^{-1} \qquad \text{Equation A.2}$$

Commonly used units for LET are keV μm^{-1}. LET is an averaged quantity and can be approximated using the Bethe-Bloch formula.

The quality factor, Q, is used to weight the absorbed dose for the biological effectiveness of the charged particles producing the absorbed dose (ICRU, 1993). The product of Q and D is called the dose equivalent (H).

Q is defined as a function of the linear energy transfer (LET) of the incident radiation that produced the absorbed dose (ICRP, 1991). Figure A-1 illustrates the defined relationship between Q and incident particle LET.

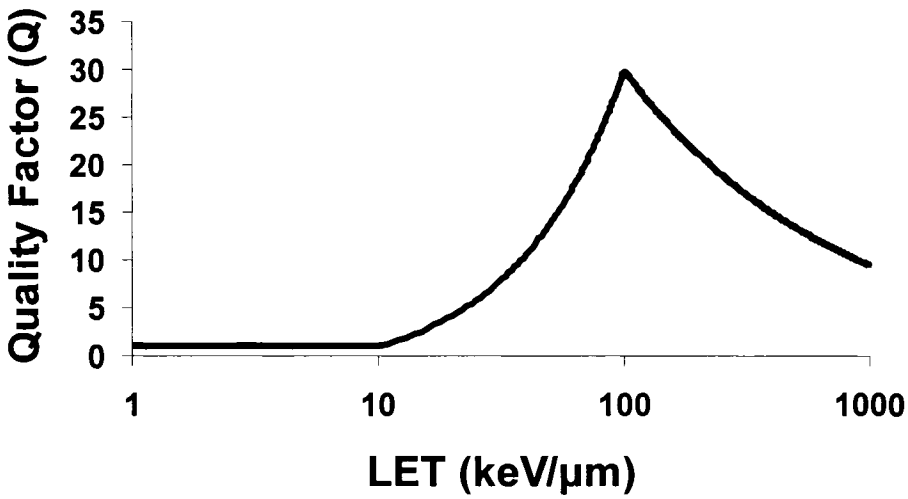

Figure A-1. Illustration of relationship between quality factor and LET as defined by ICRP 60.

The dose equivalent, H, is the product of Q and D at a point in tissue, where D is the absorbed dose and Q is the quality factor at that point (ICRU, 1993).

$$H = Q * D \quad \text{Unit: J kg}^{-1} \qquad \text{Equation A.3}$$

The name for the unit of dose equivalent is sievert (Sv).

The gray equivalent, G_T , (unit name is gray equivalent) is the product of R_i and D_T , where (ICRU, 1993):

$$G_T = R_i * D_T \quad \text{Unit: J kg}^{-1} \qquad \text{Equation A.4}$$

Where:

R_i = The recommended value of the relative biological effectiveness for a particle type *i* (unitless).
D_T = The mean absorbed dose in a tissue (T) or organ (Gray).

Table A-1
R_i Values Used to Convert D_T to G_T

Particle Type	R_i (range for value)
1 to 5 MeV neutrons	6.0 (4-8)
5 to 50 MeV neutrons	3.5 (2-5)
Heavy ions (*e.g.* , helium, carbon, neon, argon)	2.5 (1-4)
Protons > 2 MeV	1.5 (---)

The equivalent dose, H_T , (unit name is the sievert) is the product of W_R and $D_{T,R}$ (ICRU, 1993). The radiation weighting factors, W_R , are based on the type and the quality of the external radiation field (ICRP 1990). The assignment of a W_R value based on the type and energy of the external radiation field is in contrast to the assignment of a quality factor for a radiation field (Equation A.3) defined by the LET of the radiation at a point in tissue. Values of these radiation weighting factors are found in Table A-2. The quantity $D_{T,R}$ is the absorbed dose averaged over a tissue (T) resulting from the external radiation field (R) incident upon the tissue. The quantity of absorbed dose found in Equation A.1 (and used in Equation A.3) by contrast is defined at a point in tissue.

$$H_T = W_R * D_{T,R} \quad \text{Unit: J kg}^{-1} \qquad \text{Equation A.5}$$

Where:

W_R = Radiation weighting factor (unitless).

$D_{T,R}$ = The absorbed dose averaged over a tissue (T) or organ resulting from incident radiation (R) (Gray).

Table A-2
Radiation Weighting Factors

Type and Energy Range		W_R
Photons, all energies		1
Electrons, positrons and muons, all energies		1
Neutrons, energy	<10 keV	5
	10 keV to 100 keV	10
	>100 keV to 2 MeV	20
	>2 MeV to 20 MeV	10
	>20 MeV	5
Protons, other than recoil protons, energy > 2MeV		2
Alpha particles, fission fragments, nonrelativistic heavy nuclei		20

The type and energy range of radiation found in Table A-2 is not comprehensive. For example, half of the six different energies of ^{56}Fe particles used in this work are considered to be relativistic and therefore not assigned a radiation weighting factor in Table A-2. Also, in Low Earth Orbit (LEO) there exists a multipart mixture of the types and energies of radiation described in Table A-2. In the LEO radiation environment it is not possible to accurately determine the quantities necessary to calculate the equivalent dose (H_T) as described in Equation A.5. In cases such as this where either the radiation type and energy of interest has not been assigned a radiation weighting factor, or it is not possible to accurately determine the quantities necessary to calculate the equivalent dose (H_T), the quantity $\overline{H}_T$ may be substituted for H_T. The quantity $\overline{H}_T$ (units of Sievert) was determined to approximate

the quantity H_T to an acceptable degree for radiation protection purposes (NCRP 2000). The following formula describes how $\overline{H}_T$ is measured and calculated.

$$\overline{H}_T = M_T^{-1} * \int_x \int_L Q(L)D(L)\rho(x)dLdx \quad \text{Unit: J kg}^{-1} \qquad \text{Equation A.6}$$

Where:

M_T = The mass of tissue (kg).
Q(L) = The quality factor (Q) for radiation of LET (L) (unitless).

D(L) = The absorbed dose to tissue (D) from radiation of LET (L) (J kg^{-1})

ρ(x) = The density of the tissue (kg $(cm^3)^{-1}$).

The effective dose, E , (units of sievert) is the sum of the weighted $H_T \approx \overline{H_T}$ for all of the tissues irradiated (ICRU, 1993). The value of the tissue weighting factor, W_T, depends on the tissue (T) and the risk to this tissue of radiation induced stochastic detriment. "The values of W_T are chosen so that a uniform equivalent dose over the whole body gives an effective dose numerically equal to that uniform equivalent dose. The sum of the tissue weighting factors is then unity" (ICRP 1990). The types of detriment include mortality and morbidity risks from cancer (including length of life lost) and the possibility of hereditary effects. Values for W_T may be found in Table A-3

$$E = \sum_T W_T * H_T \quad \text{Unit: J kg}^{-1} \qquad \text{Equation A.7}$$

Where:

W_T = Tissue weighting factor (unitless).

H_T = Equivalent dose received by tissue T (Seivert).

Table A-3
Tissue Weighting Factors W_T

0.01	0.05	0.12	0.20
Bone surface	Bladder	Bone marrow	Gonads
Skin	Breast	Colon	
	Liver	Lung	
	Esophagus	Stomach	
	Thyroid		
	Remainder		

Lineal Energy, y, is the quotient of the energy imparted to the volume of interest ε, and the mean chord length through the volume of interest, $\bar{l}$ (ICRU, 1983).

$$y = \frac{\varepsilon}{\bar{l}} \qquad \text{Unit: J m}^{-1} \qquad \text{Equation A.8}$$

Commonly used units for lineal energy are keV μm^{-1}. Lineal energy is a stochastic quantity.

Mean free path randomness (μ-randomness) is defined in ICRU 36 as (ICRU, 1983):

"A chord of a convex body is defined by a point in Euclidian space and a direction. The point and the direction are from independent uniform distributions. This randomness results if the convex body is exposed to a uniform isotropic field of straight infinite tracks."

Commonly used units were used in the following derivation. The distribution of chord lengths, l, in a sphere of diameter, d, for a μ-random irradiation of particles is:

$$t(l) = \frac{2l}{d^2} dl \ , \ 0 < l < d \qquad \text{Equation A.9}$$

Units: l, d, are μm.

The first moment (expected value) of this distribution is:

$$\bar{l} = \frac{2}{3} d \qquad \text{Units: } \mu m \qquad \text{Equation A.10}$$

The *idealized* lineal energy, y, distribution begins with the assumption that the energy deposited ε in the sphere by any given particle traversal from the μ-random radiation field of chord length l and LET, L. This is the case when all of energy related to L is deposited locally in the sphere.

$$\varepsilon = l * L \quad \text{Units: keV} \qquad \text{Equation A.11}$$

Equation A.11 is substituted into equation A.8.

$$y = \frac{l * L}{\bar{l}} \quad \text{Units: keV } \mu m^{-1} \qquad \text{Equation A.12}$$

When $l = d$ (maximum chord length through the sphere) in equation A.5, then by equations A.10 and A.12:

$$y = \frac{3L}{2} \quad \text{Units: keV } \mu m^{-1} \qquad \text{Equation A.13}$$

Equation A.9 is transformed with equations A.10, A.12, and A.13 into a function of y.

$$f(y) = \frac{8y}{9L^2} dy \ , \ 0 < y < \frac{3}{2} L \quad \text{Units: keV } \mu m^{-1} \qquad \text{Equation A.14}$$

The frequency mean lineal energy, $\bar{y}_F$, is the first moment of this distribution.

$$\bar{y}_F = \int_0^{\frac{3}{2}L} y \bullet f(y)dy \quad \text{Units keV } \mu m^{-1} \qquad \text{Equation A.15}$$

Integrating A.15

$$\bar{y}_F = L \quad \text{Units keV } \mu m^{-1} \qquad \text{Equation A.16}$$

The dose mean lineal energy, $\bar{y}_D$, is the second moment of equation A.14.

$$\bar{y}_D = \frac{1}{\bar{y}_F} \bullet \int_0^{\frac{3}{2}L} y^2 \bullet f(y)dy \quad \text{Units: keV } \mu m^{-1} \qquad \text{Equation A.17}$$

Solving A.17

$$\bar{y}_D = \frac{8}{9}L \quad \text{Units: keV } \mu m^{-1} \qquad \text{Equation A.18}$$

The active gas volume of the TEPC used in this work was in the shape of a sphere with a diameter equal to 12.7-mm. This gas volume simulated a sphere of tissue with a diameter equal to 1- μm. A propane based tissue equivalent (TE) gas

was used in the active volume to simulate tissue. The 1- μm diameter sphere was simulated by application of the following equality (ICRU, 1983).

$$\Delta E_T = \left(\frac{S}{\rho}\right)_T \bullet \rho_T \bullet D_T = \left(\frac{S}{\rho}\right)_g \bullet \rho_g \bullet D_g = \Delta E_g \qquad \text{Equation A.19}$$

Where:

$\Delta E_T = \Delta E_g$ is equal to the energy loss by the incident particle in the simulated volume of tissue (ΔE_T) and the gas volume (ΔE_g).

$\left(\frac{S}{\rho}\right)_T$ is the mass stopping power of the incident particle in the simulated tissue.

$\left(\frac{S}{\rho}\right)_g$ is the mass stopping power of the incident particle in the gas volume.

ρ_T is the density of the simulated tissue.

ρ_g is the density of the TE gas.

D_T is the diameter of the simulated volume of tissue.

D_g is the diameter of the TE gas volume.

Underlying assumptions of this equality are that the gas volume and the simulated volume of tissue have the same atomic composition, and that the mass stopping powers are independent of density.

APPENDIX B

SPATIALLY RESTRICTED LET EQUATION

Calculating the amount of energy deposited by HZE particles in small volumes of interest can be a computationally intensive procedure. Attempts have been made to develop a simple analytical model that was capable of calculating this quantity. Achieving this goal was one of the primary motivations for the development of the spatially restricted LET equation.

The spatially restricted LET equation is a modification of an energy restricted LET equation (Xapsos, 1992). Energy restricted LET equations are constructed to neglect contribution to energy deposition in small volumes of interest by delta rays ejected from an HZE particle track that have energy above a cutoff value. The delta ray energy cutoff value is calculated as a function of the range of the delta rays and the dimensions of the volume of interest. Assumptions of the spatially restricted LET equation are:

1. The density and composition of the volume of interest and the surrounding medium were homogeneous.
2. Particle tracks (paths) through a volume of interest were restricted to be straight lines.
3. A particle must traverse the volume of interest in order to deposit energy. When particles were outside the volume of interest they could not deposit energy inside the volume.
4. Energy was deposited by delta rays in the direction normal to the HZE track.

5. The delta ray energy cutoff value was defined to be the energy of an electron with a range equal to the average chord length for μ-random irradiation through the volume of interest.
6. Energy loss straggling by the HZE particle through the volume of interest was approximated using a lognormal distribution.

Figure B-1 illustrates an HZE particle track surrounded by a cylindrical volume with radius R_c and length L_c. The tracks of three delta rays (e_1, e_2, e_3) are shown after being ejected in a direction normal to the HZE track. The energy of e_1, $E(e_1)$, is such that the range of e_1 is equal to the radius of the cylindrical volume R_c. The energies of e_2 and e_3 are greater than $E(e_1)$, and consequently their range is greater than R_c.

The spatially restricted LET model can be used in this example to calculate the energy deposited in the spherical volume of interest by delta rays ejected from the HZE particle track. In this example, $E(e_1)$ would be considered to be the cutoff value. Delta rays with energy less than $E(e_1)$ would be used in the calculation of energy deposition in the spherical volume. In an energy restricted LET model the contribution to energy deposited in the spherical volume of delta rays with energy greater than $E(e_1)$ (including e_2 and e_3) would be entirely ignored. When applied to this example the spatially restricted LET equation also uses the delta ray energy cutoff value of $E(e_1)$. The radius of the cylinder (R_c) is chosen to be equal to the average chord length of a μ-random irradiation of the spherical volume of interest. R_c is therefore equal to $\frac{2}{3}D$ where D is the diameter of the sphere (equation A.6, Appendix A).

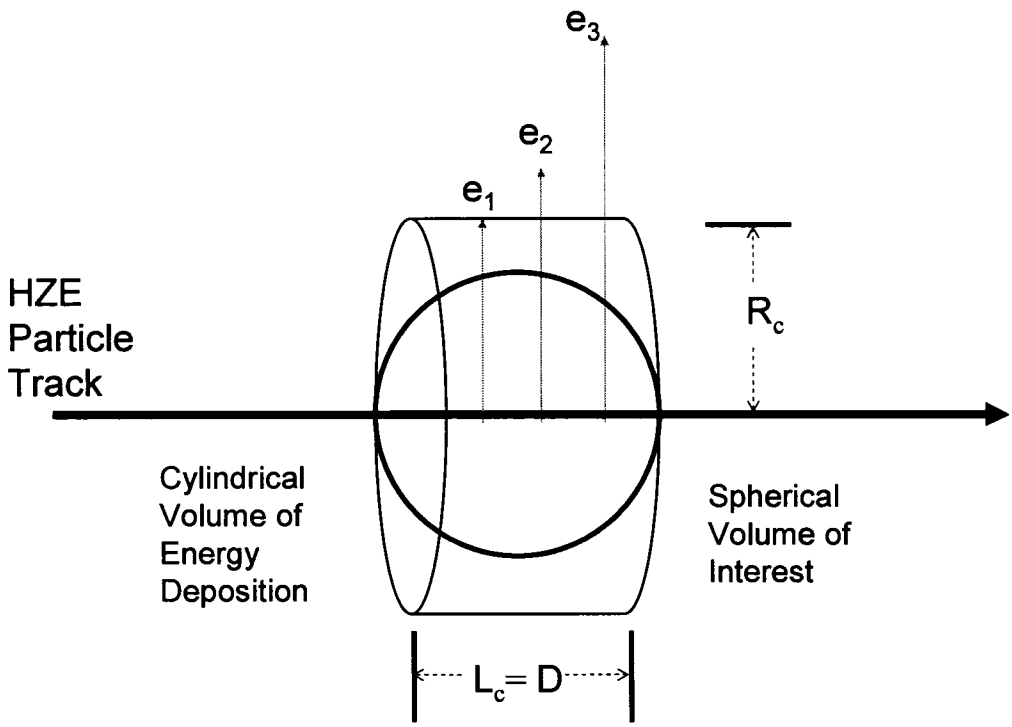

Figure B-1. Diagram illustrating an HZE particle track surrounded by a cylindrical volume of energy deposition and a spherical volume of interest. The thick black line represents an HZE particle track. The black cylinder with radius R_c and length L_c represents the volume of energy deposition. Units of R_c and L_c are in μm. The gray arrows labeled e_1, e_2, and e_3 represent delta rays ejected normally from the particle track. Units of the energies e_1, e_2, and e_3 are keV. The black circle represents the spherical volume of interest with diameter D (μm). The HZE particle track traverses the spherical volume of interest at impact parameter equal to 0-μm.

The spatially restricted LET equation used to calculate the energy deposited in the spherical volume of interest by the HZE charged particle track as illustrated in Figure B-1 follows (Xapsos, 1992; Xapsos et al., 1996).

$$f_{ion} = \frac{\ln\left[\frac{T_{e\max} * (\Delta + \Delta_1 + \Delta_2)}{I^2}\right]}{2 * \ln\left[\frac{T_{e\max}}{I^2}\right]}$$ Unitless Equation B.1

Where:

$0 \le f_{ion} \le 1$

$T_{e\max}$ = the maximum energy of an electron that can be ejected from the HZE particle track (keV)

Δ = the energy of an electron with a range equal to the average chord length through the volume of interest (keV).

I = the mean excitation energy of the medium in the volume of interest (keV).

$$\Delta_1 = \Delta * \left(1 - \frac{\Delta}{T_{e\max}}\right)$$ Units: keV

$$\Delta_2 = I * \left(1 - \frac{\Delta}{T_{e\max}}\right)$$ Units: keV

$\varepsilon_{L_c} = f_{ion} * L * L_c$ Units: keV Equation B.2

Where:

$0 \le f_{ion} \le 1$ (unitless)

L = The LET of the HZE particle (keV μm^{-1}).

L_c = The chord length of the HZE particle track through the volume (μm).

In the example illustrated in Figure B-1, Δ is the cutoff energy denoted $E(e_1)$.The parameters Δ_1 and Δ_2, are added to Δ in equation B.1. The term Δ_1 adds energy to Δ to account for the energy transferred within the volume of interest by delta rays with energy greater than $E(e_1)$. The term Δ_2 adds energy to Δ to account for the energy of ionization and excitation contained in atoms which experience the primary ionization and produce delta rays with energy greater than $E(e_1)$. Accounting for these two missing fractions of LET transform the energy restricted LET equation into a spatially restricted LET equation.

Continuing with the example in Figure B-1, equation B.2 illustrates the calculation of the amount of energy deposited (ε_{L_c}) in the spherical volume by the HZE particle track. This energy is calculated as the product of the LET of the particle, the chord length of the particle through the volume of interest (L_c) and the fraction (f_{ion}) of LET calculated with equation B.1.

To account for energy loss straggling of the HZE particle as it traverses any chord length l through the volume of interest, the energy deposited ε_l is distributed using a lognormal distribution. The lognormal probability density function as applied in the spatially restricted LET equation is represented by $p_l(\varepsilon)$.

$$\int p_l(\varepsilon)d\varepsilon = 1 \quad \text{Unitless} \qquad \text{Equation B.3}$$

Where:

ε = The energy deposited in the volume of interest (keV)
l (subscript) = denotes that the distribution represents energy deposition of a particle for one chord length l through the volume of interest.

The parameters of the lognormal distribution are related to the energy deposited ε_l and the relative variance of ionizations in the volume of interest. Further details of these calculations may be found in Xapsos 1996.

Figure 4-9 illustrates the distribution of energy deposited in a 1-μm sphere of tissue by 360 MeV/nucleon ^{56}Fe particles with impact parameters equal to 0-mm as calculated by the spatially restricted LET equation. The energy deposited ε_l was distributed using the lognormal distribution as previously described.

Both the LET of the incident HZE particle and the calculated value for f_{ion} are independent of the chord length of the HZE particle traversal. Consequently, calculations performed with the spatially restricted LET equation for one HZE particle traversal in a volume of interest may be easily extended to calculate the distribution of energy deposited in a volume of interest by a μ-random radiation field. In the case of a spherical volume of interest, the chord length distribution for a μ-random irradiation is calculated using equation A.5 (Appendix A). The lognormal energy distribution described by equation B.3 is convoluted with equation A.5 (Xapsos et al., 1996):

$$f(\varepsilon) = \int_l p_l(\varepsilon) \cdot t(l) dl = 1 \quad \text{Unitless} \qquad \text{Equation B.4}$$

Where:

ε = energy deposited (keV).

l = chord length (μm).

The probability density function $f(\varepsilon)$ is the energy deposition distribution in a spherical volume of interest by a μ-random monoenergetic HZE radiation field as calculated by the spatially restricted LET equation. Distributions of $f(\varepsilon)$ (in the form of CDFs) of energy deposited in a 1-μm diameter spherical volume of tissue by μ-random irradiations of ^{56}Fe at six different energies are presented in Figure B-2.

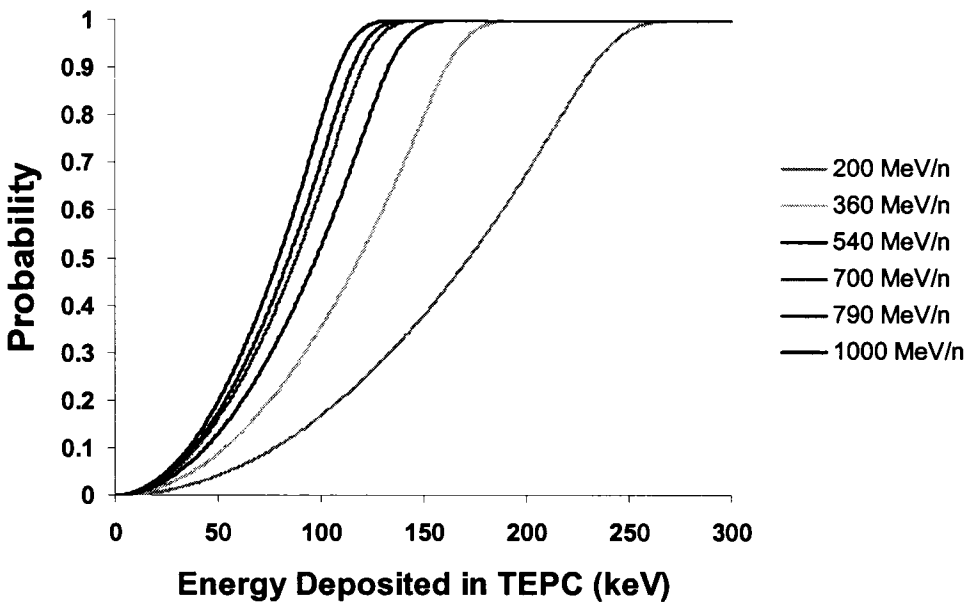

Figure B-2. Probability distributions of energy deposited in a 1-μm diameter spherical volume of tissue by μ-random irradiations of ^{56}Fe at six different energies as calculated by the spatially restricted LET equation. Distributions are presented in the form of Cumulative Distribution Functions (CDFs).

APPENDIX C

RADIAL DOSE MODEL

Cucinotta et al. developed a radial dose distribution model for HZE particles traversing water (Cucinotta et al., 1995). Input parameters for this model were the energy (in MeV/nucleon), charge number, and the mass number of the HZE particle. The output of this model was in the form of dose to water (Gy) at 100 discrete distances radial from the HZE track (Figure C-1). Radial dose distribution calculations were performed with a FORTRAN computer code furnished by Dr. Cucinotta.

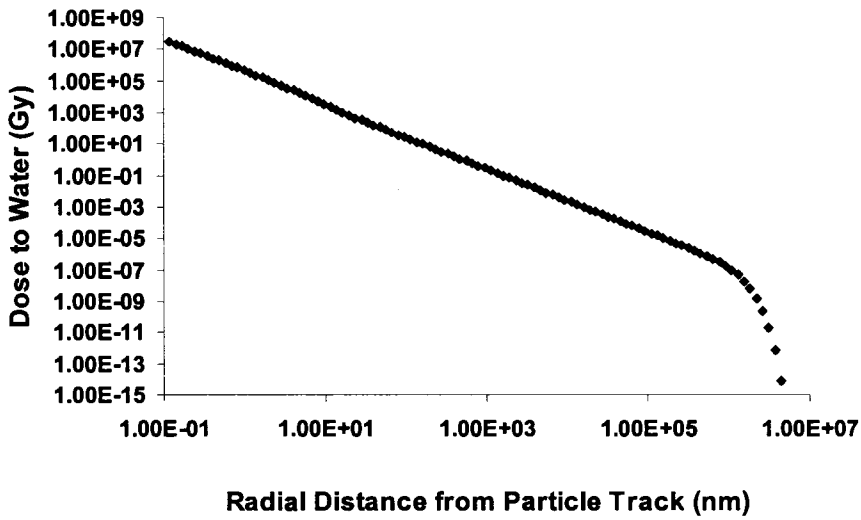

Figure C-1. The radial dose distribution from a 363 MeV/u ^{56}Fe particle track traversing water as calculated by the radial dose model Cucinotta et al. 1995.

Information concerning the underlying mechanisms of this model may be found in Cucinotta et al. 1995.

The results from this model were used to calculate the amount of energy deposited in a 1- μm diameter water sphere by particle tracks traversing the sphere at 23 different impact parameters. In these calculations the 1- μm diameter water sphere was surrounded by a spherical water shell.

This calculation was performed twice. In the first calculation (homogeneous conditions), the density of water inside the 1- μm diameter water sphere and in the spherical water shell was equal. In the second calculation (heterogeneous conditions), the 1- μm diameter water sphere was held constant, but the density of the spherical water shell was increased by a factor of 14000 times. This difference between the densities of the 1- μm diameter water sphere and the spherical water shell were chosen to correspond to the difference in density between the tissue equivalent wall and the gas cavity of the TEPC.

In both cases a numerical integration was performed using the radial dose model output in order to determine the amount of absorbed dose (and subsequently the energy) deposited in the 1-um diameter water sphere. The numerical integration was performed by dividing the TEPC active volume into 1000 circular slices transverse to the direction of the beam of particles (Figure C-2). Absorbed dose to each of these slices was determined by integrating the dose to concentric arcs radiating in a radial direction from the point of intersection of the particle track and

the plane of the slice in question. Figures C-3 and C-4 show representative arcs of integration for two of the integration configurations (Figure C-2, points 1 and 2).

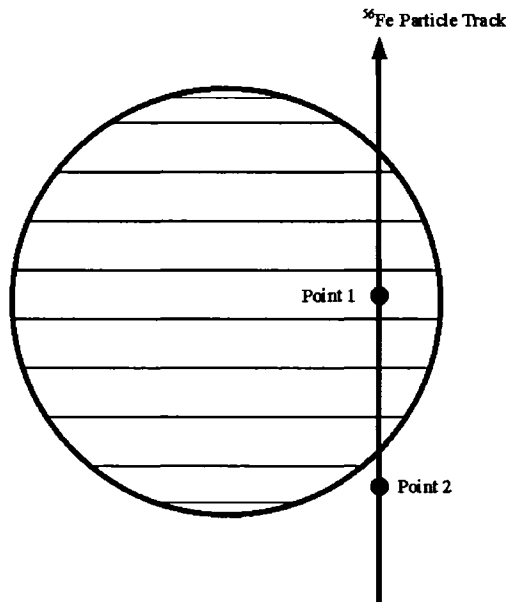

Figure C-2. Diagram of ^{56}Fe particle traversing TEPC active volume with point 1 and point 2 highlighted. Horizontal lines denote boundaries of areas of interest used in numeric integration (circular slices).

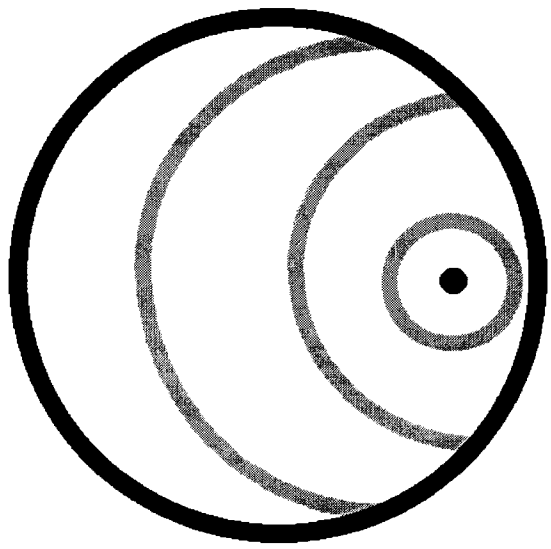

Figure C-3. Viewpoint is in direction of the beam. The outer black ring represents the boundary of the 1- μm diameter water sphere. The black filled circle

represents point 1 from Figure C-2. The gray filled arcs are representative volumes of integration in calculation.

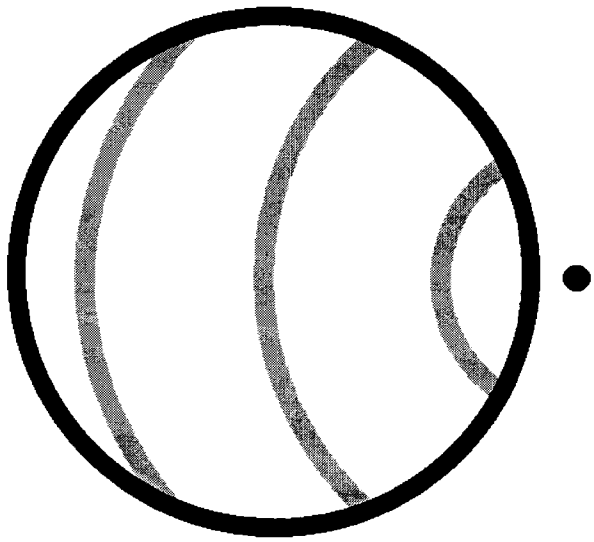

Figure C-4. Viewpoint is in direction of the beam. The outer black ring represents the boundary of the 1- μm diameter water sphere. The black filled circle represents point 2 from Figure C-2. The gray filled arcs are representative volumes of integration in calculation.

The steps of the calculation follow.

1. Begin at impact parameter of 0- μm.
2. Start at first circular slice of the 1- μm diameter water sphere (bottom of diagram Figure C-2).
3. Use the radial dose model to calculate the absorbed dose to water in concentric cylindrical shells with depth equal to the depth of the circular slice, and thickness equal to the change in radial distance from the particle track. The radial dose distribution model provided absorbed dose to 100 discrete radial distances from the particle track (Figure C-1).
4. Determine the fraction of the volumes of these concentric cylindrical shells that was inside of the boundaries of the circular slice.
5. Calculate the dose, and subsequently the energy deposited in the 1- μm diameter water sphere attributable to the volumes determined in step 4.
6. Proceed to the next circular slice (move up the diagram in Figure C-2) and repeat steps 3-5 until last circular slice of integration.

7. Total the absorbed dose and energy deposited by the particle to all of the circular slices.
8. Change impact parameter of particle track to the 2nd of 23 values.
9. Repeat steps through 2-8 until absorbed dose and energy deposited to the 1- μm diameter water sphere for all 23 impact parameters have been calculated.

The calculations for the homogeneous conditions and heterogeneous conditions proceeded in the manner described in steps 1-9. In the heterogeneous condition, the density of the spherical water shell was 14000 times greater than the 1- μm diameter water sphere it surrounded. For integration configurations illustrated in Figure C-4 (particle track in spherical water shell) this increase in density of the medium led to a change in the dimensions of both the length of the track, and the radial distance of the track from the 1- μm diameter water sphere. The change in these dimensions was governed by the equality in equation A-16. This made it possible to calculate the increase in absorbed dose and energy deposited in the 1- μm diameter water sphere by the particle track traversing a high density wall. Results from these calculations are shown in Figure C-5.

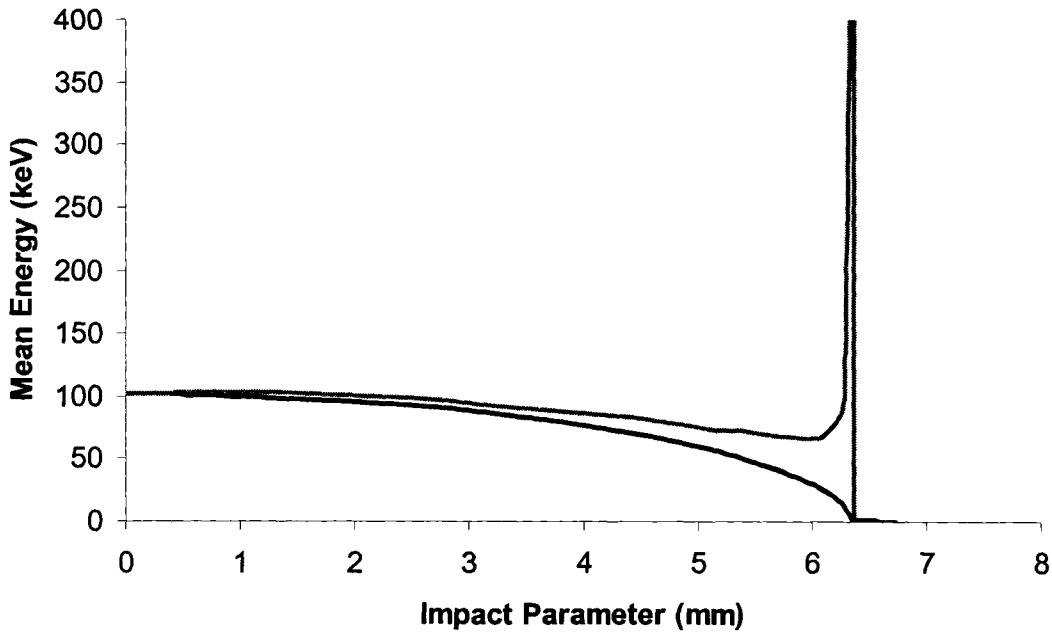

Figure C-5. Results from numeric integration technique using output from the radial dose model for different TEPC impact parameters. Incident particle was 360 MeV/u ^{56}Fe. The black line represents results from the calculation assuming homogeneous conditions. The gray line represents results from the calculation assuming heterogeneous conditions.

APPENDIX D

BTC4 MODEL

Experiments were performed at particle accelerator facilities that exposed a ½" TEPC simulating a 1-μm diameter sphere of tissue to ^{56}Fe particles at six different energies.

The TEPC had a tissue equivalent wall 2.54-mm thick and an active gas volume 12.7-mm in diameter. Models were used to calculate energy deposition in the TEPC active volume and the results of these calculations were compared to experimental results. The direction of energy deposition in both the spatially restricted LET equation (Appendix B) and the radial dose distribution model (Appendix C) were restricted to be in only the radial direction perpendicular to the ^{56}Fe particle track.

When HZE particles pass though the TE wall, there is a forward component of electrons ejected from the track that cannot be calculated by these two models. The BTC4 model was developed to allow calculation of energy deposition by electrons ejected from an ^{56}Fe particle track in directions other than (and including) the radial direction from the track. This model also accounted for the heterogeneity of the density of the TEPC wall and gas cavity in the calculations. The BTC4 model

calculated energy deposition in the TEPC active volume only for ^{56}Fe particle tracks with an impact parameter equal to 0-mm (particles that traversed the entire diameter of the TEPC).

BTC4 Model Assumptions

Assumptions of this model were:

1. The volume of interest was a sphere of TE gas 12.7-mm in diameter.
2. The volume of interest was surrounded by a spherical shell of TE plastic 2.4-mm thick called the wall.
3. One particle track from a monogenergetic ^{56}Fe particle traversed the entire volume of interest and the spherical TE plastic shell at an impact parameter equal to 0-mm. .
4. The LET of the ^{56}Fe particle did not change as it traversed the volume.
5. The only energy deposition in the volume of interest from the ^{56}Fe particle track was by delta rays.
6. The particle track was restricted to be a straight line.

One input parameter was necessary for the BTC4 model to calculate energy deposition by an ^{56}Fe particle in the TEPC active volume, and this was the energy of the incident particle in units of MeV/nucleon. The illustration in Figure D-1 shows (as the thick black line) an ^{56}Fe particle track with impact parameter equal to 0-mm. The particle track was defined to begin at the outer edge of the wall (point A in Figure D-1), traverse the entire diameter of the volume of interest, and end at the outer edge of the wall (point B in Figure D-1) opposite the beginning point. This particle track length was divided into 1-μm segments. The model calculated the amount of energy deposited in the volume of interest by delta rays originating at the particle track every 1-μm of track length between point A and point B in Figure D-1.

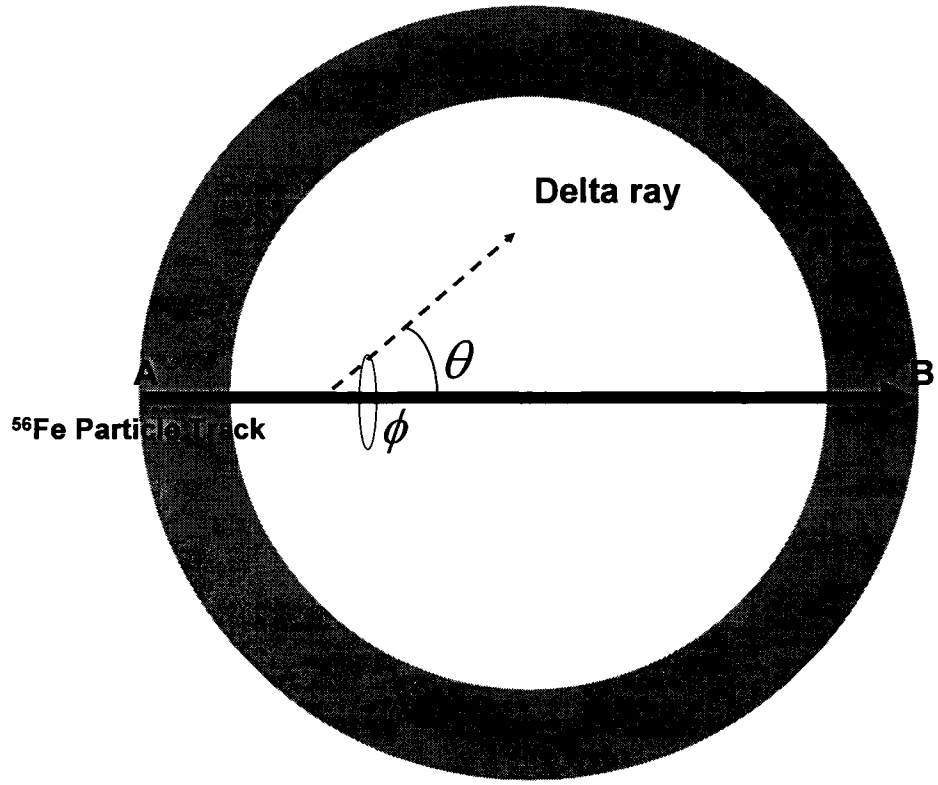

Figure D-1. Diagram of TEPC wall (gray ring) surrounding TEPC active volume. The thick black line represents an ^{56}Fe particle track. Point A is denoted to represent the starting point of the ^{56}Fe particle track. Point B is denoted to represent the starting point of the ^{56}Fe particle track. The dashed black line is a delta ray being ejected from the particle track at angles θ and Φ.

The procedure for the calculation of energy deposition in the volume of interest by delta rays from each 1-μm segment of ^{56}Fe particle track length proceeded in the following fashion.

1. The LET of the incident ^{56}Fe particle was calculated using the Bethe-Bloch formula (ICRU, 1970).

2. Calculations of delta ray energy deposition began in first 1-μm segment of ^{56}Fe particle track length illustrated as point A in Figure D-1.
3. The energy spectrum of delta rays produced by the particle track was calculated using the Rudd model (Rudd, 1988; Rudd, 1989). The delta ray energy spectrum was divided into 200 logarithmically spaced energy bins.
4. Distributions of the angular ejection (θ and Φ in Figure D-1) of the delta rays from the particle track were calculated for each of the 200 delta ray energy bins (bins determined in step 3). A secondary electron (delta ray) angular ejection distribution model was used in these calculations (Cucinotta et al., 1995). Vectors for the ejected delta rays were then calculated.
5. Energy deposition in the wall and the volume of interest by the delta rays along the individual delta ray vectors was calculated using an electron energy dissipation model (Kobetich and Katz, 1969). If the delta ray vector did not intersect the volume of interest, or if the energy of the delta ray was dissipated before it reached the volume of interest it was removed from the calculation.
6. Steps 3 through 5 were repeated for the second 1-μm segment of ^{56}Fe particle track length.
7. Steps 3 through 6 were repeated until energy deposition to the volume of interest by delta rays produced in the final 1-μm segment of ^{56}Fe particle track length (point B in Figure D-1) were calculated.

Results from the calculations performed with the BTC4 model are found in Table 4-2 and Figure 4-8. The model calculates energy deposition to within 13% of the experimental results for each of the six energies of ^{56}Fe.

Models Used in BTC4 Model

I. Rudd Model

The Rudd model is an analytical equation that calculates the energy distribution of secondary electrons produced by a proton track in a medium of interest

(Rudd, 1988; Rudd, 1989). Input parameters for the Rudd model are the incident proton energy and the binding energies of the electrons in the medium of interest. The distribution of secondary electron energies calculated by the Rudd model may be scaled by Z^2 to produce the distribution of secondary electrons from an HZE particle track. At ^{56}Fe particle energies from 200-1000 MeV/nucleon, results from the Rudd model are consistent with other secondary electron energy distribution models including Bethe theory (Rudd, 1988).

An example of a probability density function of secondary electron energy spectrum as calculated using the Rudd model is illustrated in Figure D-2. Further details of the Rudd model may be found in Rudd 1988, and Rudd 1989.

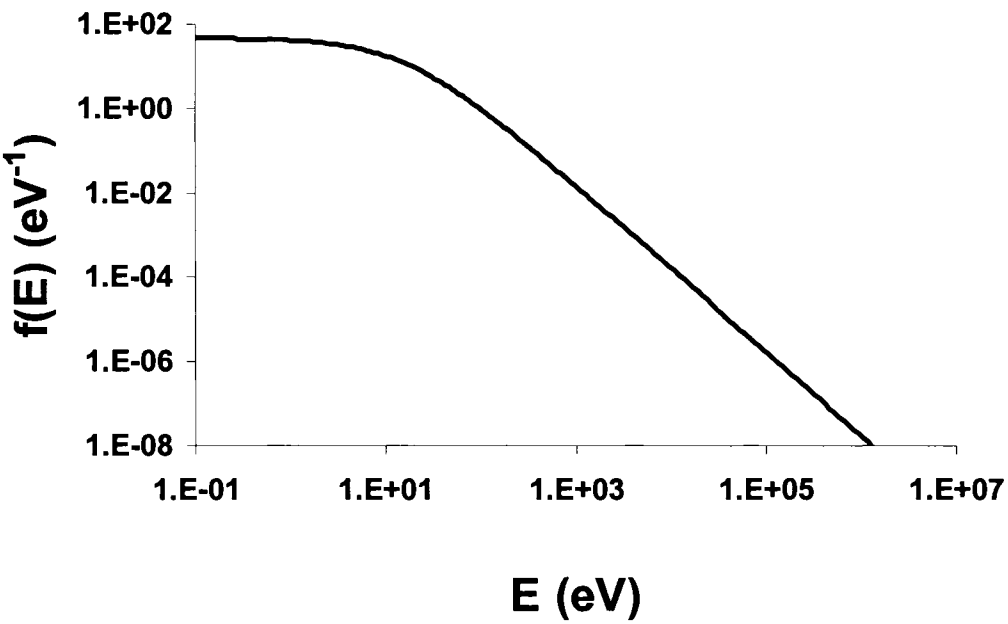

Figure D-2. A probability density function of secondary electron energy spectrum as calculated using the Rudd model. The incident particle in this calculation was a 540 MeV/nucleon ^{56}Fe ion. The medium traversed by the particle was water.

II. Secondary Electron Angular Ejection Distribution Model

Collisions between charged particles and electrons in the medium of interest cause these electrons to be ejected from the particle track. The angle of the secondary electrons (delta rays) ejection relative to the direction of the particle track is defined as θ (Figure D-1). Classical kinematics can describe the angle θ with the following formula (Cucinotta et al., 1995):

$$\cos^2\theta = \frac{\omega}{\omega_m} \qquad \text{Units: Radians} \qquad \text{Equation D.1}$$

Where:

θ = the angle (in radians) of the delta ray ejection from the particle track relative to the direction of the particle.
ω = the energy imparted to the secondary electron (eV).
ω_m is the maximum energy imparted to an electron (eV) by the incident charged particle.

The angle θ was calculated using equation D.1 for each of the 200 energy bins of secondary electrons as calculated by the Rudd model. For each energy bin of secondary electrons, the angle θ was distributed using the secondary electron (delta ray) angular ejection distribution model (Cucinotta et al., 1995). The distribution of θ in this model was a Wiegner probability density function. Input parameters for the

secondary electron angular ejection distribution model were the value of θ calculated with equation D.1, and ω the energy of the secondary electron for a given energy bin. The peak of this distribution was centered at the value of θ calculated with equation D.1. These data are shown in Figure D-3.

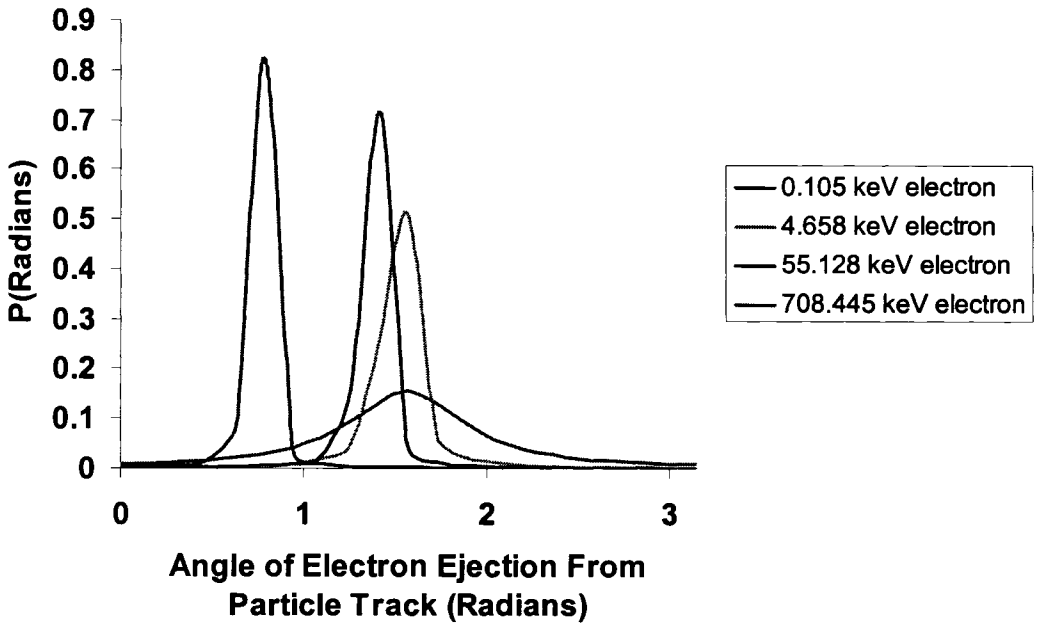

Figure D-3. Probability density functions of electron ejection angles in radians from particle track for 4 electron energies as calculated by the secondary electron angular ejection distribution model.

III. Electron Energy Deposition Model

Energetic electrons ejected from a charged particle track travel a convoluted path through the medium surrounding the track (Knoll, 1979). The mass of the energetic electrons are equal to the mass of the orbital electrons in the surrounding

medium. This allows large transfers of energy (and resulting change in direction of travel) during collisions of the energetic electrons and orbital electrons. Monte Carlo calculations designed to model the complex path of delta rays are very computationally intensive.

The electron energy deposition model (Kobetich and Katz, 1969) is a simple analytical equation that calculates the amount of energy deposited by an energetic electron in a medium of interest. This model has input parameters of the initial energy of the electron, and the weighted average of the atomic number of the medium of interest. There is no attempt in this model to follow the complex path of the electron through the medium of interest. This model ignores electron scattering and back scattering in the medium of interest, and assumes that the energetic electrons move in a straight line through the medium of interest. The model calculates the dissipation of energy by the electron over straight line distance of penetration through the medium of interest. Results from the electron energy deposition model were compared by E.J. Kobetich and R. Katz in Electron Energy Dissipation (Kobetich and Katz, 1969) over a wide range of materials and electron energies to experimental data. An average deviation of 10% was found between the model results and the experimental data.

APPENDIX E

BEAM NORMALIZATION AND DETERMINATION OF CHARGED PARTICLE EQUILIBRIUM (CPE) IN TEPC

Beam Normalization

In the six experiments, ^{56}Fe ions were extracted from the particle accelerator, and this beam of ions irradiated the experimental setup. The fluence of Fe ions through the TEPC and the rest of the experimental setup were not spatially uniform as measured in the plane transverse to the beam. In order to obtain the complete response function of the TEPC for a spatially uniform beam (in the plane transverse to the beam), the data for all incident Fe particles were sorted into a grid consisting of 196 separate 1-mm^2 bins (Figure E-1). The X and Y coordinates of the Fe ions in the plane of the TEPC transverse to the beam were used to sort the data into the correct 1-mm^2 bin.

Once the data was sorted, a TEPC response function was calculated for each of the 196 separate 1-mm^2 bins. The 196 separate response functions were then combined and normalized to form the response function for uniformly incident Fe

ions. This distribution was referred to as the response function for the spherical TEPC. This process was repeated for each of the six experiments.

The response functions of the spherical TEPC were used to calculate, frequency averaged lineal energy, $\overline{y}_f$, dose averaged lineal energy, $\overline{y}_D$, and the average quality factor, Q, for each of the six experiments.

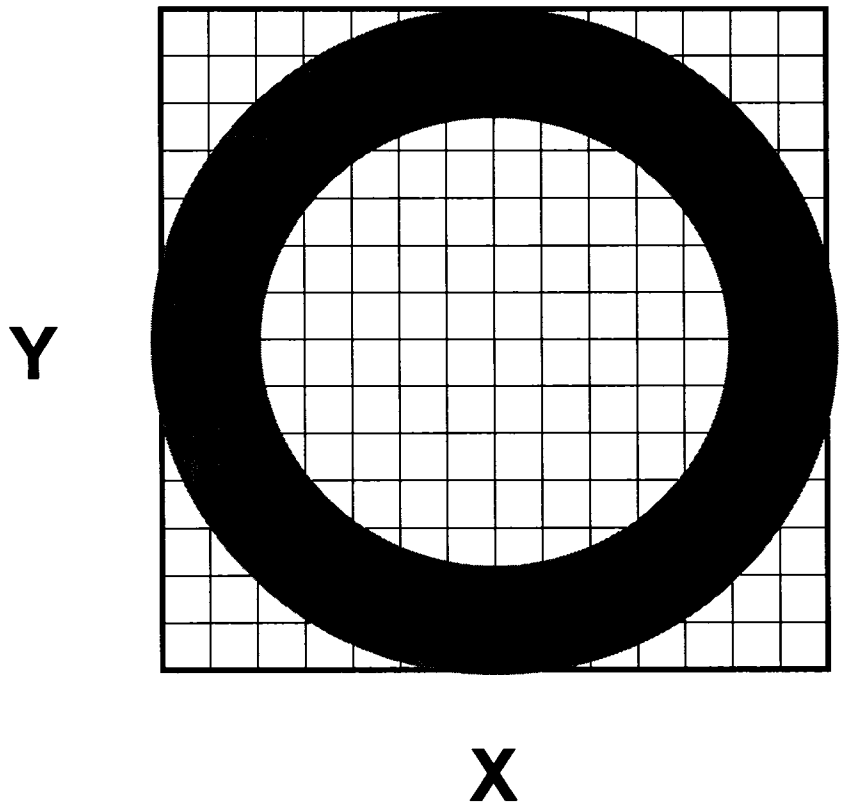

Figure E-1. Representation of 196-mm^2 grid used to produce a response function for the TEPC under conditions of spatially uniform irradiation. X and Y Cartesian coordinates of particle events in the TEPC plane. The gray circle represents the TEPC wall.

Charged Particle Equilibrium Determination

Under the conditions of charged particle equilibrium, the absorbed dose to the TEPC can be calculated using two different methods.

I. Utilization of the response function for the spherical TEPC to calculate absorbed dose.

$$\text{Absorbed Dose} = \frac{\sum \varepsilon \bullet N(\varepsilon) d\varepsilon}{\rho_g \bullet V_g} \qquad \text{Units: keV kg}^{-1} \qquad \text{Equation E.1}$$

Where:

ε = energy deposited in the TEPC (keV).
$N(\varepsilon)d\varepsilon$ = the number of particle events depositing energy ε within the 196-mm^2 area. .
ρ_g = the density of the TE gas in the TEPC gas cavity (kg cm^{-3}).
V_g = the volume of the TEPC gas cavity (cm^3).

II. Utilization of the assumption of CPE in the TEPC to calculate absorbed dose.

$$\text{Absorbed Dose} = L \bullet \frac{\phi}{\rho_T} \qquad \text{Units keV kg}^{-1} \qquad \text{Equation E.2}$$

Where:

L = the LET of the incident particle (keV μm^{-1}).
ϕ = the fluence of the incident particles (particles μm^{-2}).
ρ_T = the density of tissue (kg cm^{-3}).

III. Formula to calculate Λ.

If the TEPC was in CPE when irradiated by the Fe particles, then results calculated with equations E.1 and E.2 were equal in value. To test whether the TEPC was in charged particle equilibrium in each of the six experiments equations E.1 and E.2 were set equal to each other and simplified. The resulting equality was then algebraically manipulated to set the term LET equal to the rest of the equation. Data from each of the six experiments was then used to calculate a value for this LET, and this data derived value of LET was termed Λ. This process follows:

Setting these two equations equal:

$$L \bullet \frac{\phi}{\rho_T} = \frac{\sum \varepsilon \bullet N(\varepsilon) d\varepsilon}{\rho_g \bullet V_g} \qquad \text{Equation E.3}$$

To simplify:

$$\phi = \frac{N_{particles}}{Area} \quad \text{Units: particles } \mu m^{-2} \qquad \text{Equation E.4}$$

Where:

$N_{particles}$ = the total number of particles traversing the TEPC plane in the 196, 1-mm^2 bins (Figure E.1).
$Area$ = area of the 196, 1-mm^2 bins in units of μm^2.

Using equation A.16:

$$\rho_T \bullet D_T = \rho_g \bullet D_g \qquad \text{Equation A.16}$$

Where:

ρ_T = the density of tissue (kg cm^{-3}).
ρ_g = the density of the TE gas (kg cm^{-3}).
D_T = the diameter of the simulated volume of tissue (μm).
D_g = the diameter of the TE gas volume (μm).

Solve equation A.16 for the density of the TE gas.

$$\rho_g = \frac{\rho_T \bullet D_T}{D_g} \quad \text{Units: kg cm}^{-3} \qquad \text{Equation E.5}$$

Also:

$$N_{particles} \bullet \hat{N}(\varepsilon)d\varepsilon = N(\varepsilon)d\varepsilon \qquad \text{Equation E.6}$$

Units: number of particles

Where:

$\hat{N}(\varepsilon)d\varepsilon$ is a probability density function where $\sum \hat{N}(\varepsilon)d\varepsilon = 1$

$$V_g = \frac{\pi}{6} \bullet D_g^3 \quad \text{Units: } \mu\text{m}^3 \qquad \text{Equation E.7}$$

Substitute equations E.4, E.5, E.6, and E.7 into equation E.3.

$$L \bullet \frac{N_{particles}}{Area \bullet \rho_T} = \frac{\sum \varepsilon \bullet N_{particles} \bullet \hat{N}(\varepsilon) d\varepsilon}{\frac{\rho_T \bullet D_T}{D_g} \bullet \frac{\pi}{6} \bullet D_g^3} \qquad \text{Equation E.8}$$

Solve for LET, L.

$$L = \frac{\sum \varepsilon \bullet \hat{N}(\varepsilon) d\varepsilon \bullet Area}{D_T \bullet \frac{\pi}{6} \bullet D_g^2} \quad \text{Units: keV } \mu m^{-1} \qquad \text{Equation E.9}$$

For calculations with experimental data, the value for LET has been defined to be Λ. Equation E.9 becomes:

$$\Lambda = \frac{\sum \varepsilon \bullet \hat{N}(\varepsilon) d\varepsilon \bullet Area}{D_T \bullet \frac{\pi}{6} \bullet D_g^2} \quad \text{Units: keV } \mu m^{-1} \qquad \text{Equation E.10}$$

Since:

$$\overline{y_F} = \frac{\sum \varepsilon \bullet \hat{N}(\varepsilon) d\varepsilon}{\frac{2}{3} D_T} \quad \text{Units: keV } \mu m^{-1} \qquad \text{Equation E.11}$$

Equation E.10 becomes:

$$\Lambda = \frac{\overline{y_F} \bullet Area}{\frac{3}{2} \bullet \frac{\pi}{6} \bullet D_g^2} \quad \text{Units: : keV } \mu m^{-1} \qquad \text{Equation E.12}$$

Also:

$$\text{Area of the TE gas volume} = A_g = \frac{\pi}{4} \bullet D_g^2 \qquad \text{Equation E.13}$$

Units: of μm^2

Equation E.12 becomes:

$$\Lambda = \frac{\overline{y_F} \bullet Area}{A_g} \quad \text{Units: : keV } \mu m^{-1} \qquad \text{Equation E.14}$$

If the data derived value Λ (for each experiment) was equal to the known value of LET for each ^{56}Fe ion as calculated using bethe-bloch formula (Appendix A), then CPE existed in the TEPC for that experiment. Results from these calculations are found in Table 4-1.

APPENDIX F

TIMING AND SIGNAL PATHWAY

Data from approximately 2 million particle events were recorded for each of the six experiments conducted. The data acquisition system was triggered by a coincidence between the TEPC signal and one of the PSD signals upstream of the TEPC. Figure F-1 illustrates the pathway of the electronic signal generated following a particle traversal through the TEPC and PSD2. The signals from both detectors were first transmitted to a pre-amplifier, and were then transmitted to shaping amplifiers. The fast timing signal from each of the shaping amplifiers was used in the logic pathway, while the unipolar output was sent to the analog to digital conversion (ADC) gate. The two fast timing signals from the shaping amplifiers became input signals for constant fraction discriminators (CFDs) that determined if the incoming signals were above a preset threshold. The trigger threshold in the CFD for PSD2 was set so that only primary beam ions and fragments within a few charge units of the primary fired the trigger. The trigger threshold in the CFD for the TEPC was set (for the majority of the experiment) to allow events depositing more than 3 keV in the TEPC to fire the trigger. During each experiment the TEPC trigger threshold was adjusted down to allow events depositing more than 0.5 keV in the TEPC to fire the trigger. The data acquisition system operated with this lower TEPC trigger threshold

until 2 X 10^5 events were recorded. After 2 X 10^5 were recorded with this lower TEPC trigger threshold, the TEPC trigger threshold was raised again to allow only events depositing more than 3 keV in the TEPC to fire the trigger. The outputs of the CFDs were logic pulses, and they became inputs for a coincidence detector. If the two logic pulses overlapped in time within the coincidence detector, a coincidence signal was issued from the coincidence detector. This coincidence signal denoted a valid particle event that traversed both the TEPC and PSD2.

The next step in the signal logic pathway involved the acceptance of data from a valid particle event, or the rejection of the data if the data taking system was busy. The coincidence out signal split at this point and one branch of the signal became the pre-trigger, while the other branch became input to a signal delay generator. The pre-trigger signal proceeded uninterrupted into a coincidence generator. The output from the delay generator became input for a start gate generator. This start gate generator had two outputs. The first was a signal called busy, and the second was the logical inverse of the first signal called not-busy. The busy signal was sent to a scaler that maintained a count of valid particle event coincidences between the TEPC and PSD2. The not-busy signal was transmitted to the same coincidence unit as the pre-trigger. Figure F-2 shows the timing of the pre-trigger and the not-busy signal. Because the not-busy signal was transmitted through the signal delay generator, it arrived at the coincidence unit 100 nanoseconds later than the pre-trigger. This allowed a coincidence to take place between the pre-trigger and the not-busy signals before the not-busy signal arrived in the coincidence unit. Once the not-busy signal arrived at the coincidence unit, another coincidence with the pre-trigger could not occur until

the not-busy signal turned off again. A logical coincidence is illustrated in Figure F-2 occurring between the first pre-trigger signal and the not-busy signal before the not-busy signal had arrived. The second pre-trigger signal in Figure F-2 arrived in the logic during the time that the not-busy signal had arrived and was in active state, and so a logical coincidence did not take place.

This final coincidence unit had three output signals. The first output signal was transmitted to the CAMAC ADC gate generator to begin conversion of the analog data signals to digital information. In each of the six experiments completed there were between 20 and 28 data channels that needed to be converted. The second output signal was transmitted to the list processor (LP). This LP was alerted by this signal to begin (after a suitable delay in time) the process of reading the data into a computer software program (via SCSI connection). The third signal was transmitted to a scaler that tallied the number of pre-trigger and not-busy coincidences.

The amount of time that the busy and not-busy signals maintained an activated state was 160 microseconds (Figure F-2). This was the amount of time that it took to complete taking and storing the data generated by one particle event. The ADC conversions of the data channels accounted for the majority of this time (100 microseconds). The CAMAC reading of the ADC data channels took 2 microseconds per channel and accounted for the rest of the 160 microseconds.

Live time of the system was calculated by dividing the number of pre-trigger and not-busy coincidences by the total number of pre-triggers. Under optimal running conditions the system had a live time of 40%-90%. With a system dead time of 160 microseconds, the data taking electronics had the potential to process and record 6000

particle events per second. In practice, processing this number of particles per second was unachievable. At the particle accelerator facilities where these experiments took place, particles were accelerated and extracted from the accelerator in groups (called spills). Each spill was normally several seconds in duration, but the particles were only extracted during a fraction of that total time. This limited the number of particles that could be processed per spill to approximately 6×10^3. A further limitation in the processing rate occurred because the particles were not extracted from the accelerator in an evenly distributed flow. This meant that often times more than one particle traversed the experimental apparatus within the 160 microsecond dead time of the data taking equipment. Because of these limitations, normally 500 particles per spill was the maximum data taking rate achievable by the particle spectrometer.

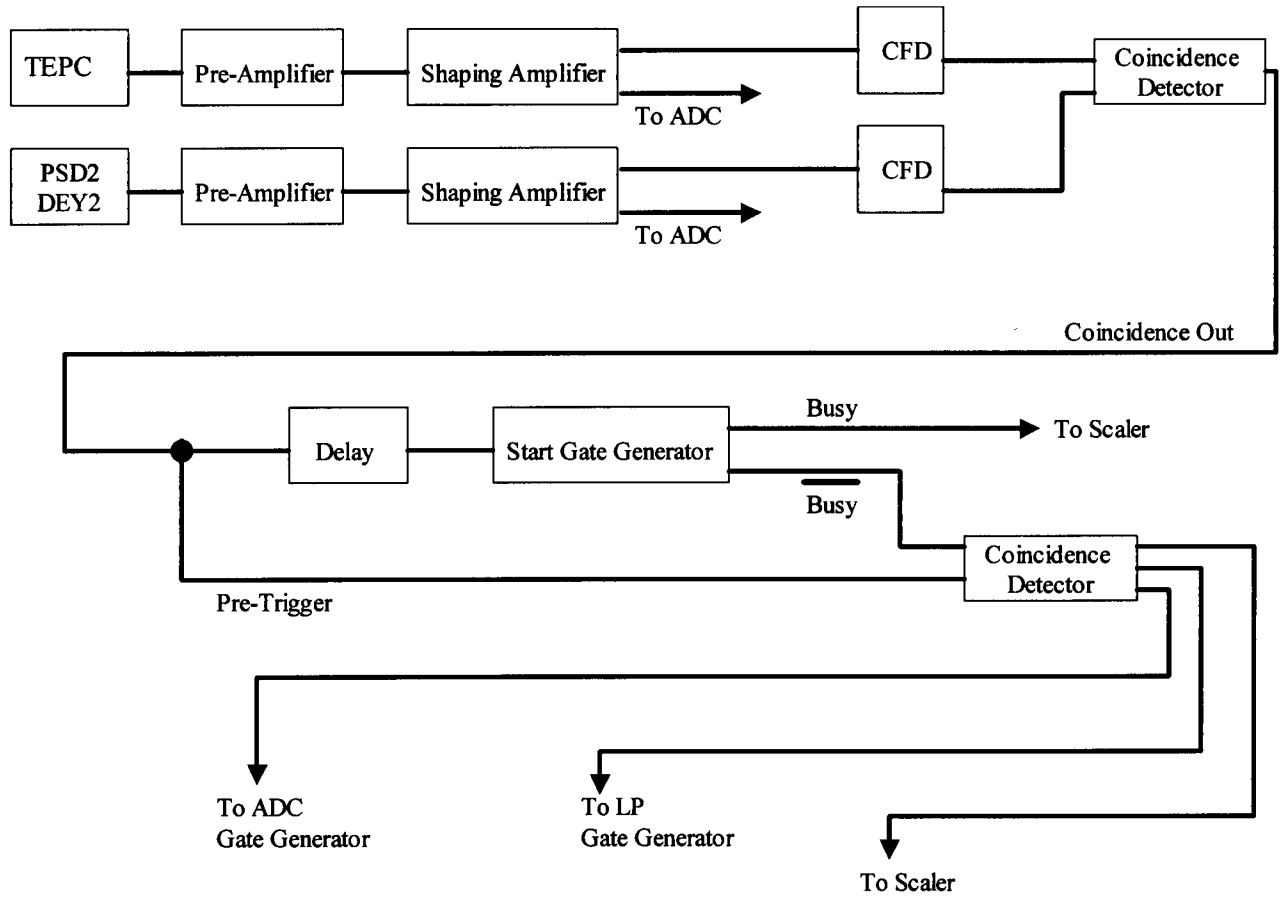

Figure F-1. An illustration of the electronic signal pathway logic produced by a particle traversal of the TEPC and PSD2.

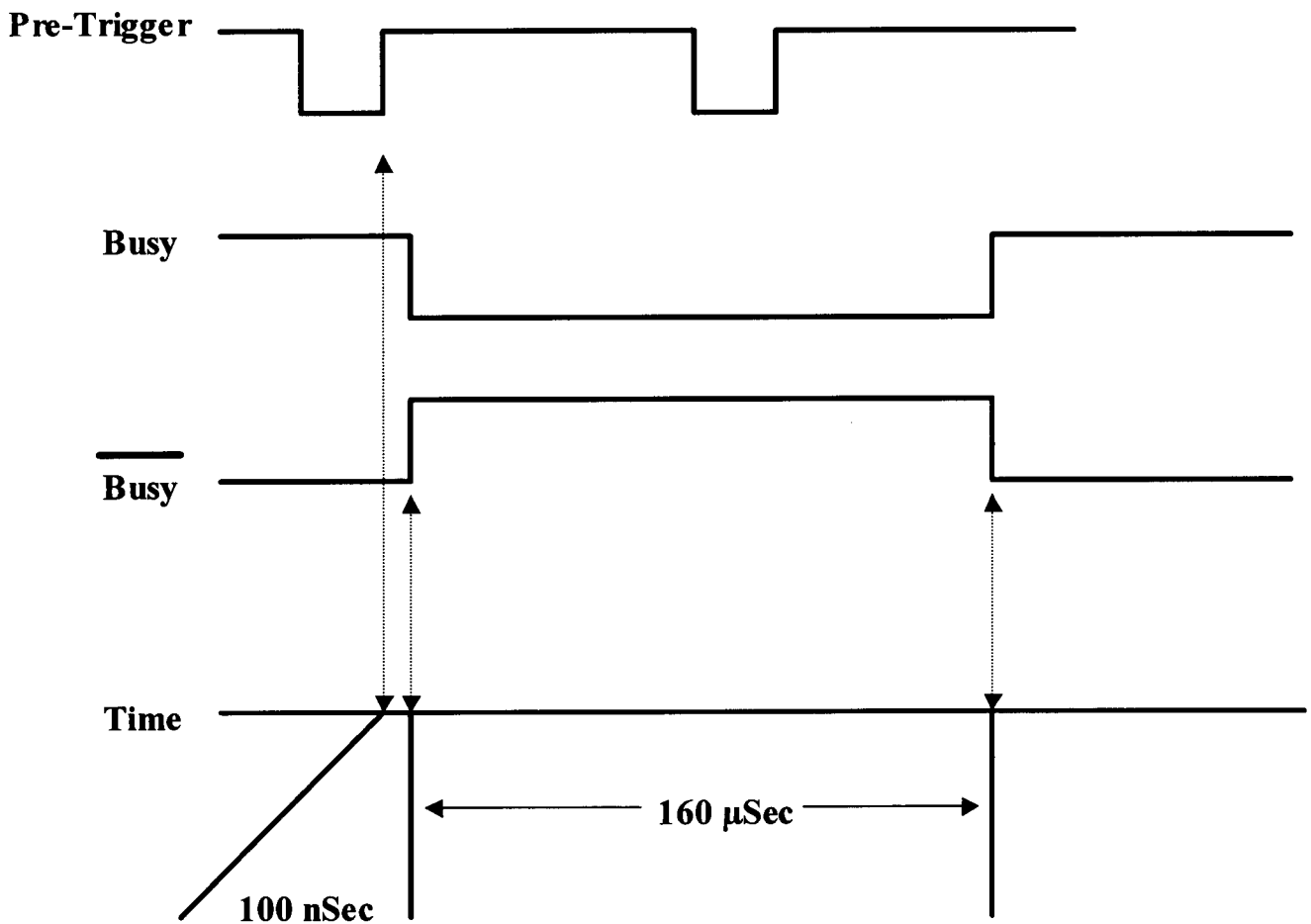

Figure F-2. Diagram illustrating the timing of the coincidence between the pre-trigger signal and the not-busy and busy signals.

APPENDIX G

RESPONSE FUNCTIONS OF TEPC

Experiments were performed at particle accelerator facilities that exposed a ½" TEPC simulating a 1-μm diameter sphere of tissue to ^{56}Fe particles at six different energies. The response functions for the six experiments are presented in this appendix. The response functions were produced using the normalization technique described in Appendix E. Also presented in this appendix are the distributions of energy deposited in the TEPC for Fe particles with impact parameters less than 0.5-mm for the six experiments.

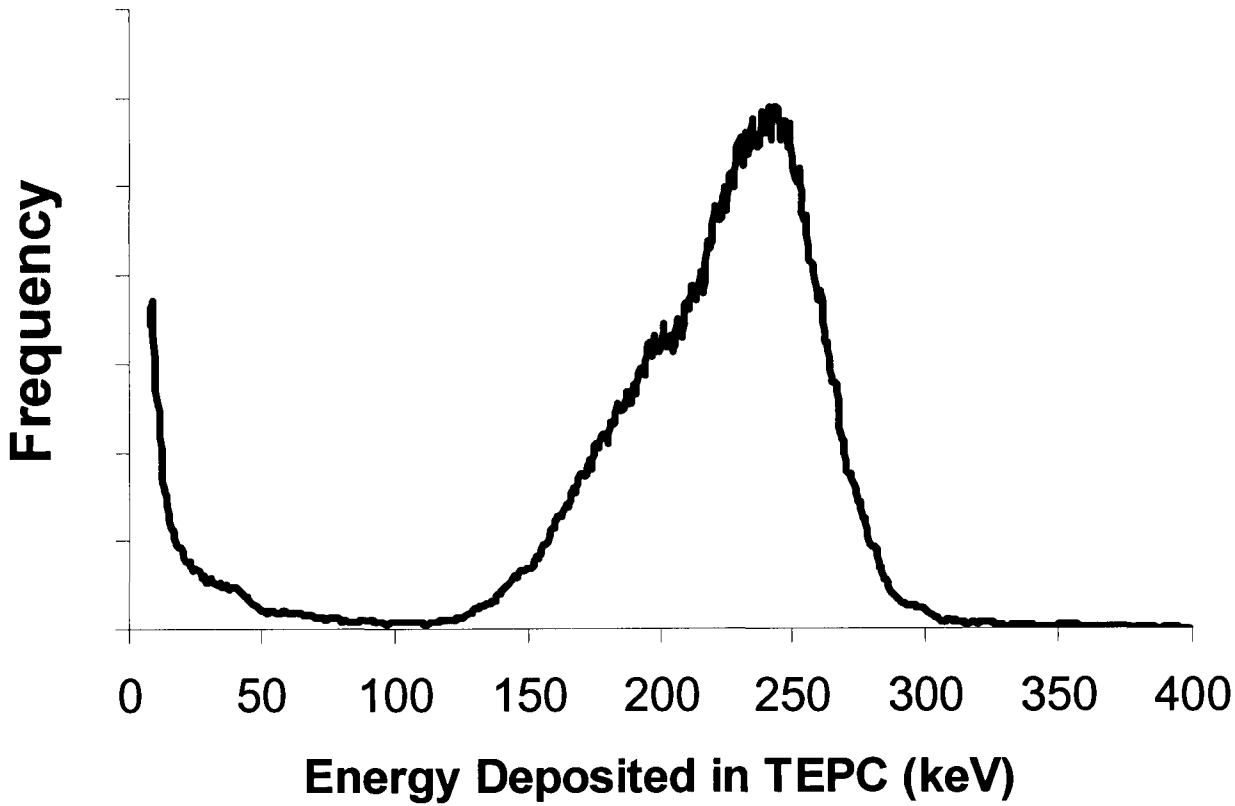

Figure G-1. Probability distribution of energy deposited in the TEPC by 200 MeV per nucleon Fe particles.

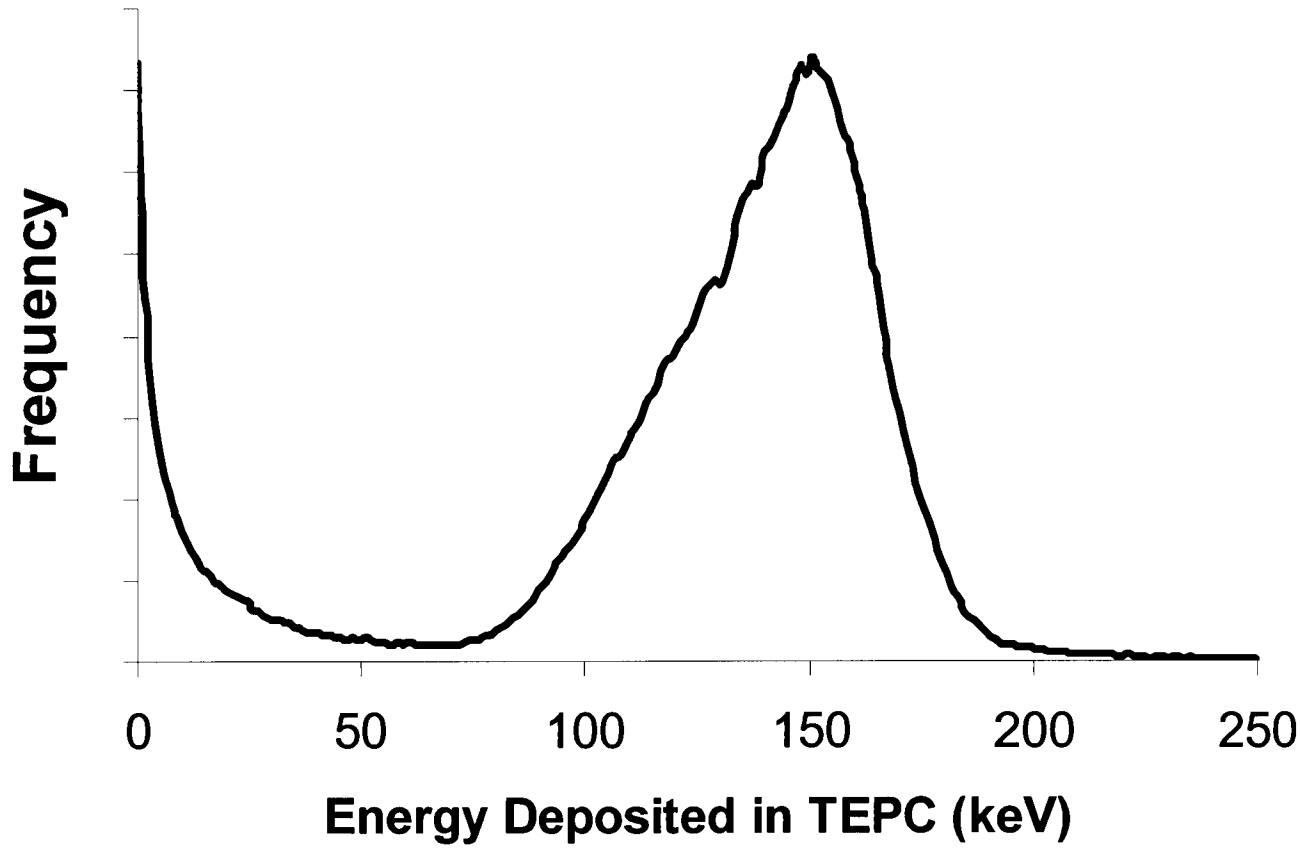

Figure G-2. Probability distribution of energy deposited in the TEPC by 360 MeV per nucleon Fe particles.

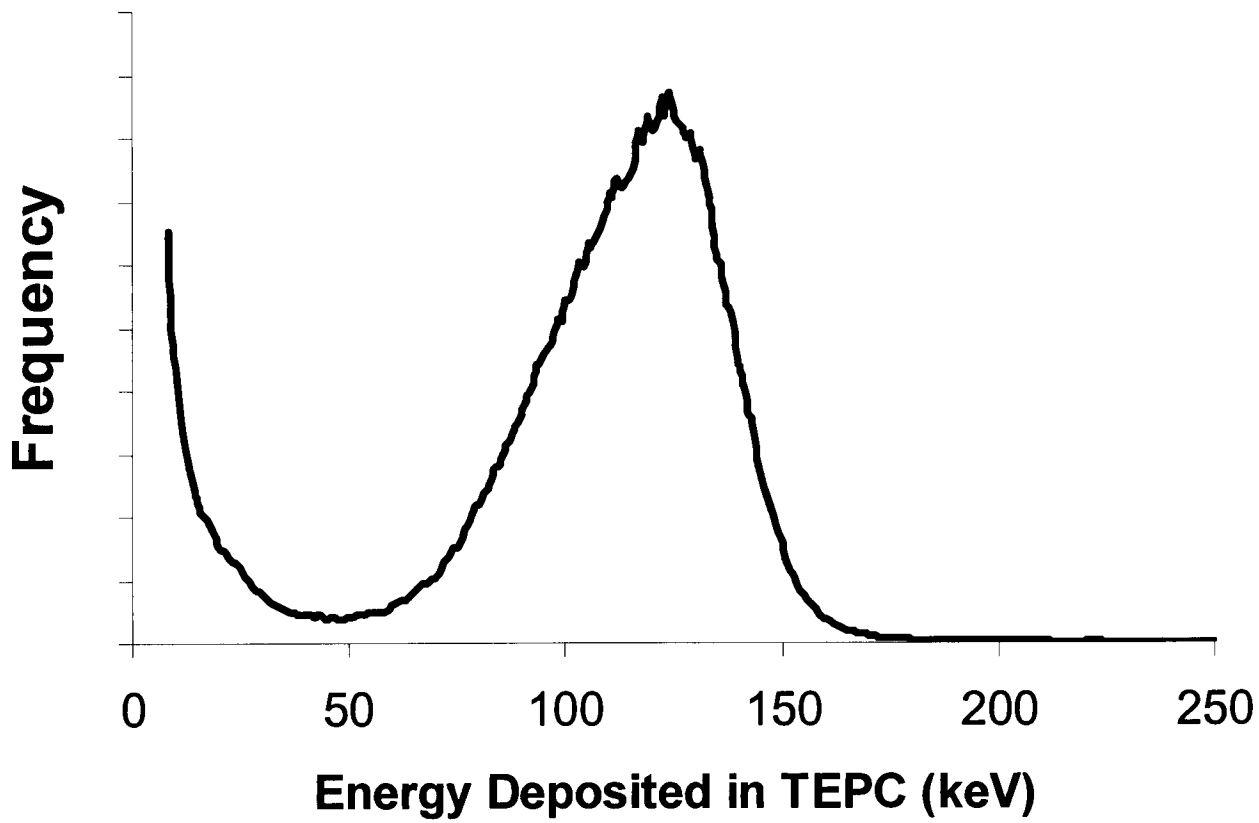

Figure G-3. Probability distribution of energy deposited in the TEPC by 540 MeV per nucleon Fe particles.

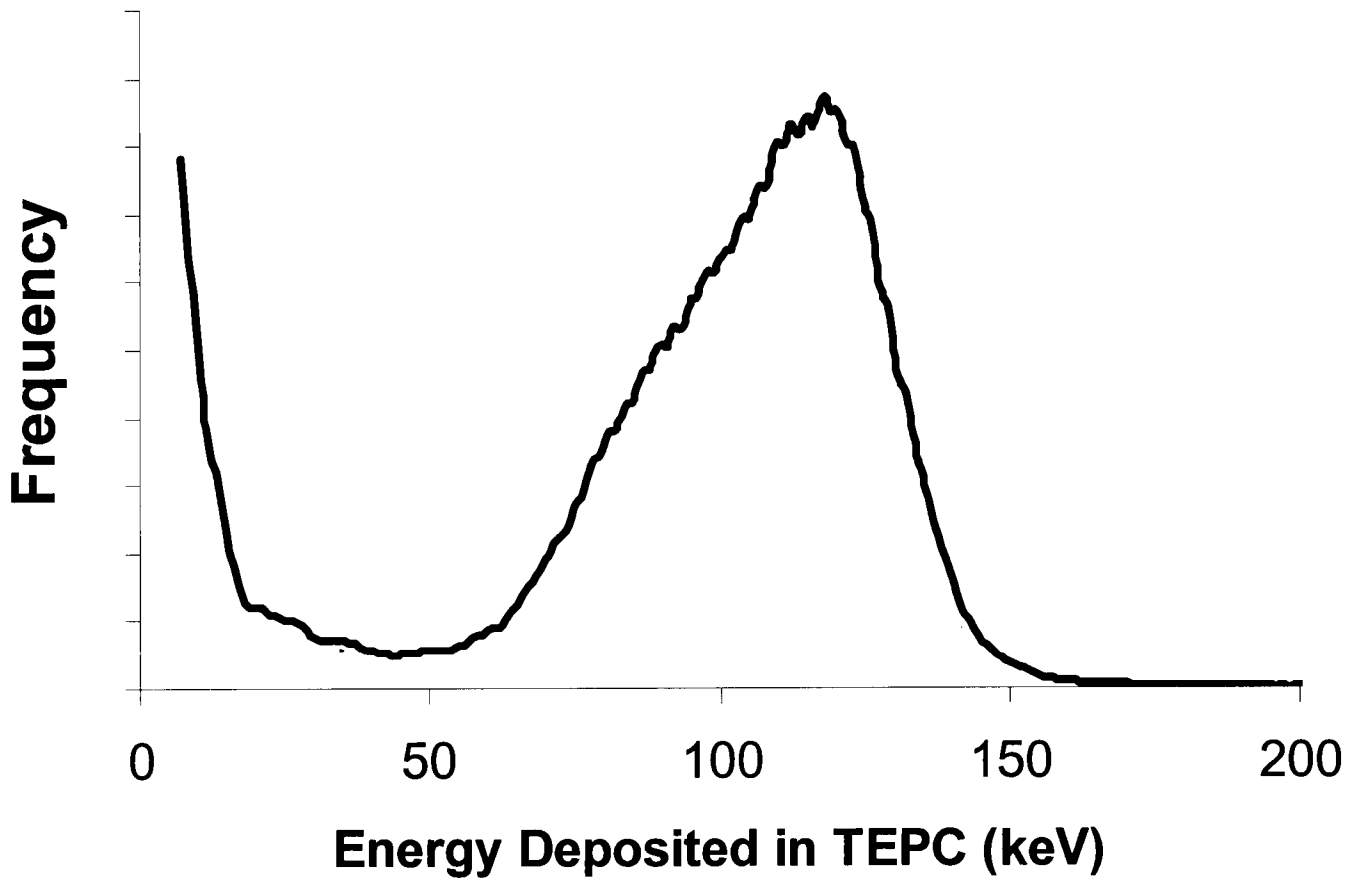

Figure G-4. Probability distribution of energy deposited in the TEPC by 700 MeV per nucleon Fe particles.

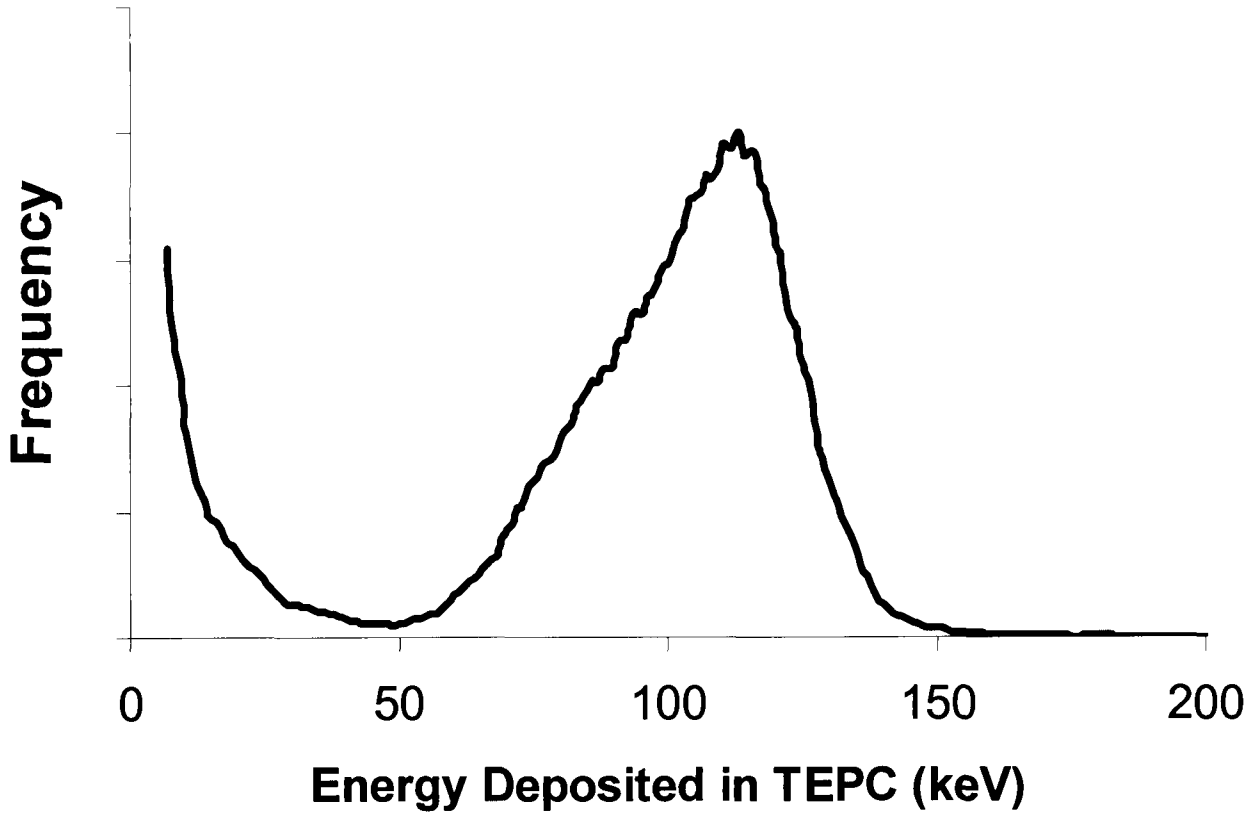

Figure G-5. Probability distribution of energy deposited in the TEPC by 790 MeV per nucleon Fe particles.

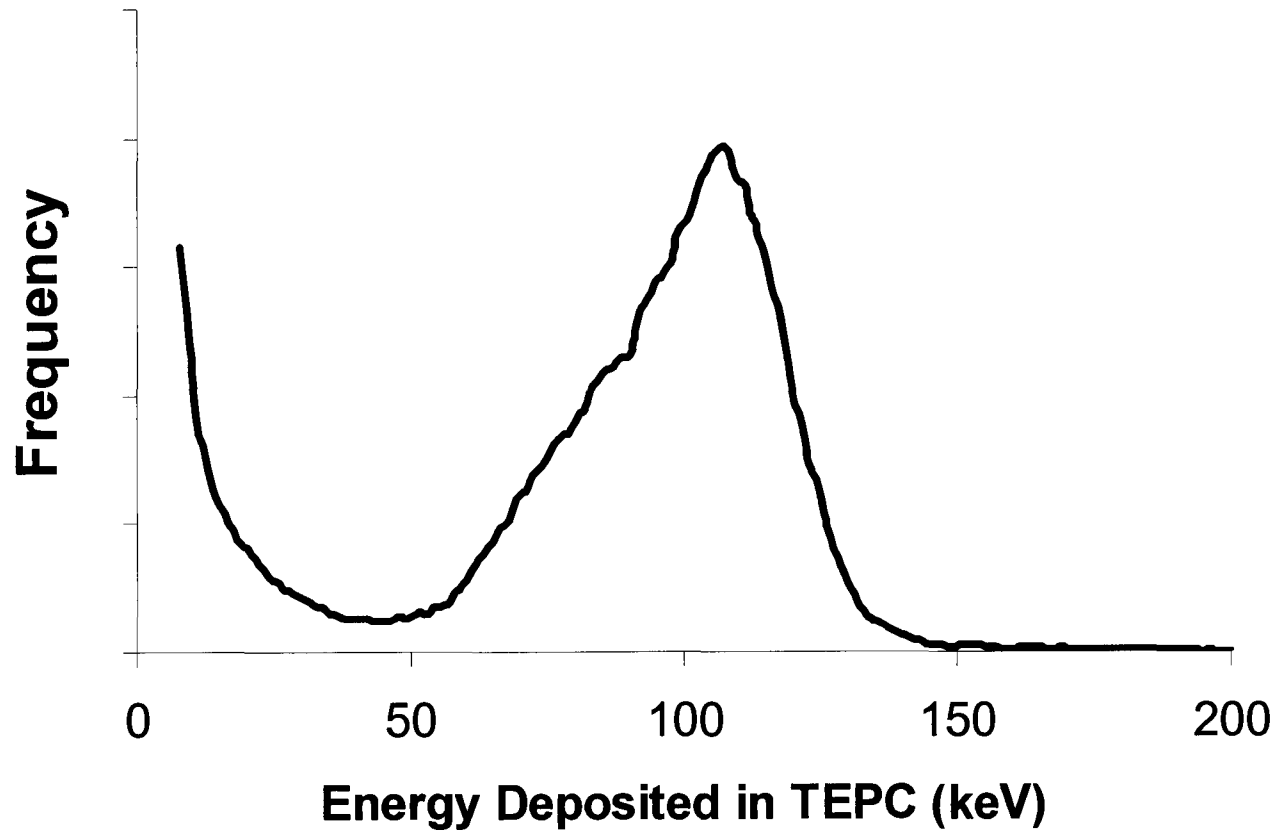

Figure G-6. Probability distribution of energy deposited in the TEPC by 1000 MeV per nucleon Fe particles.

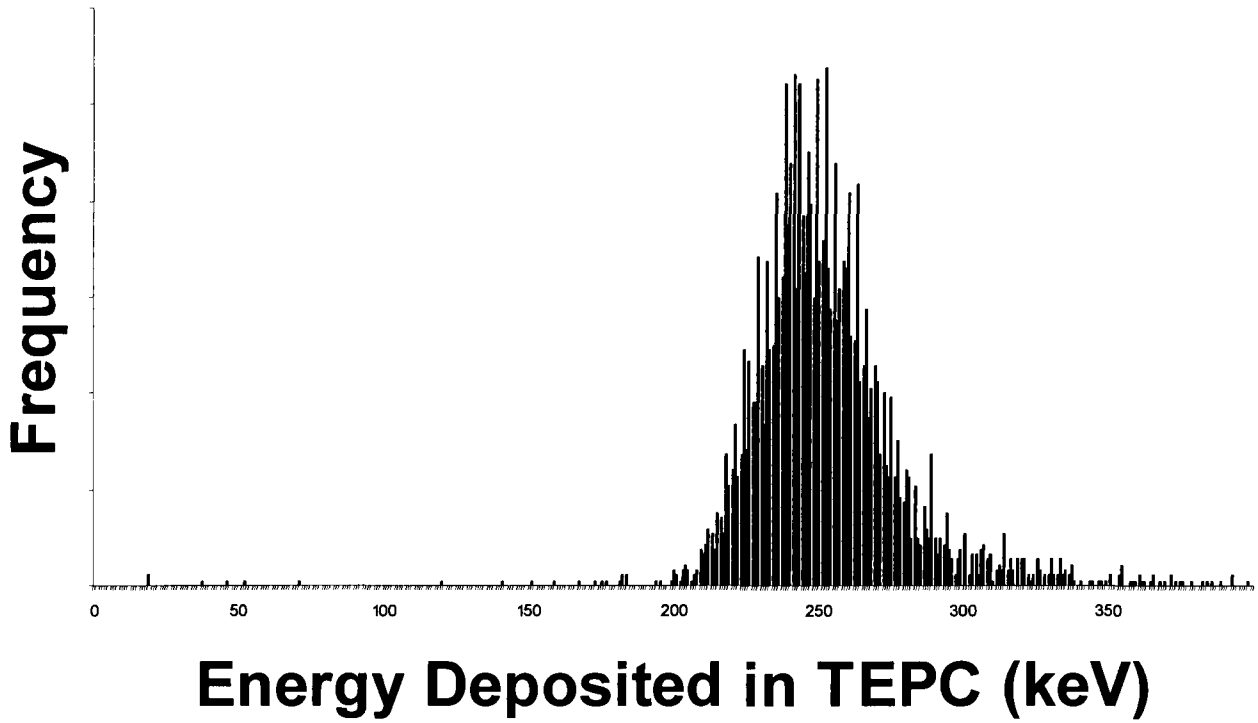

Figure G-7. Distribution of energy deposited in the TEPC by 200 MeV per nucleon Fe particles with impact parameters less than 0.5-mm.

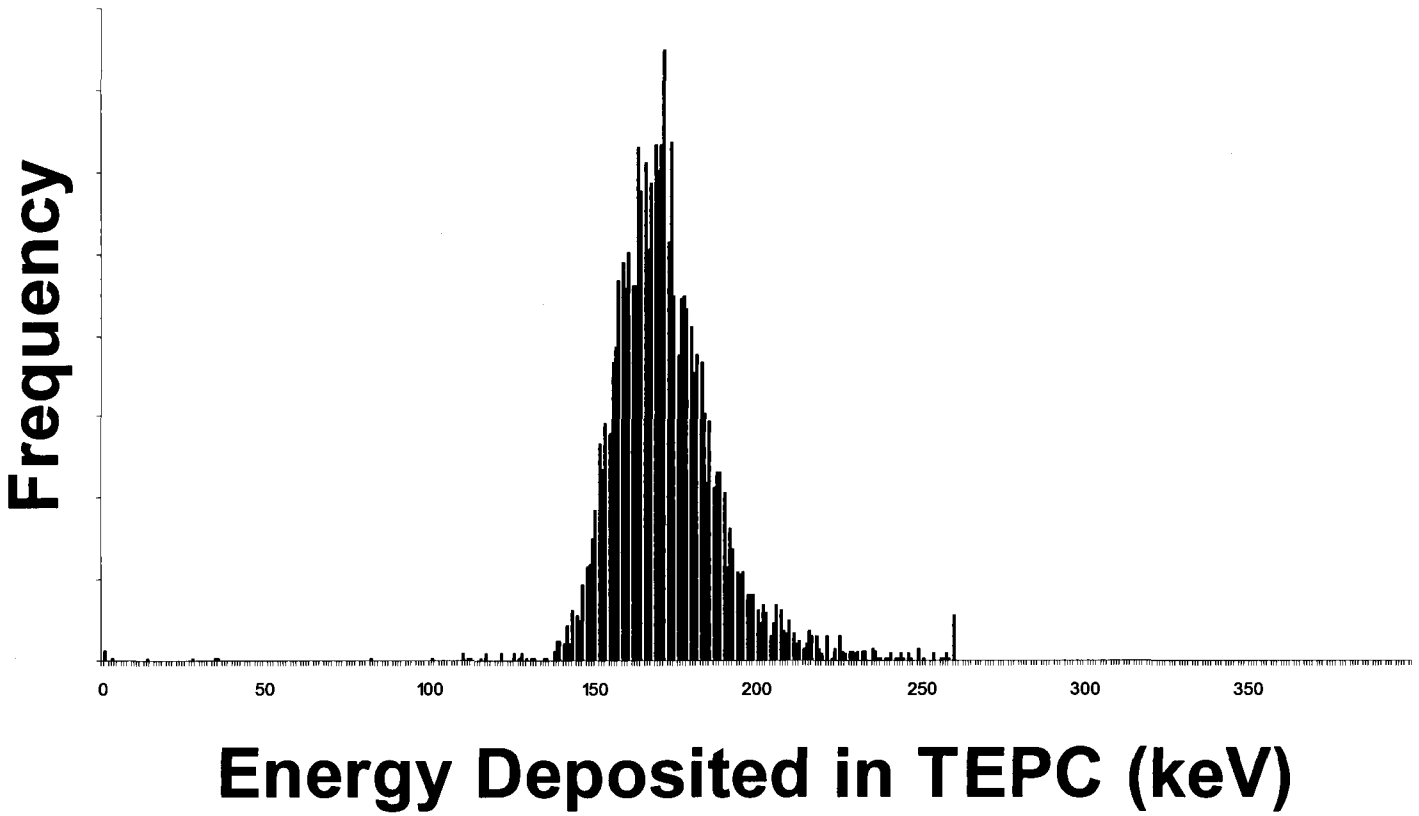

Figure G-8. Distribution of energy deposited in the TEPC by 360 MeV per nucleon Fe particles with impact parameters less than 0.5-mm.

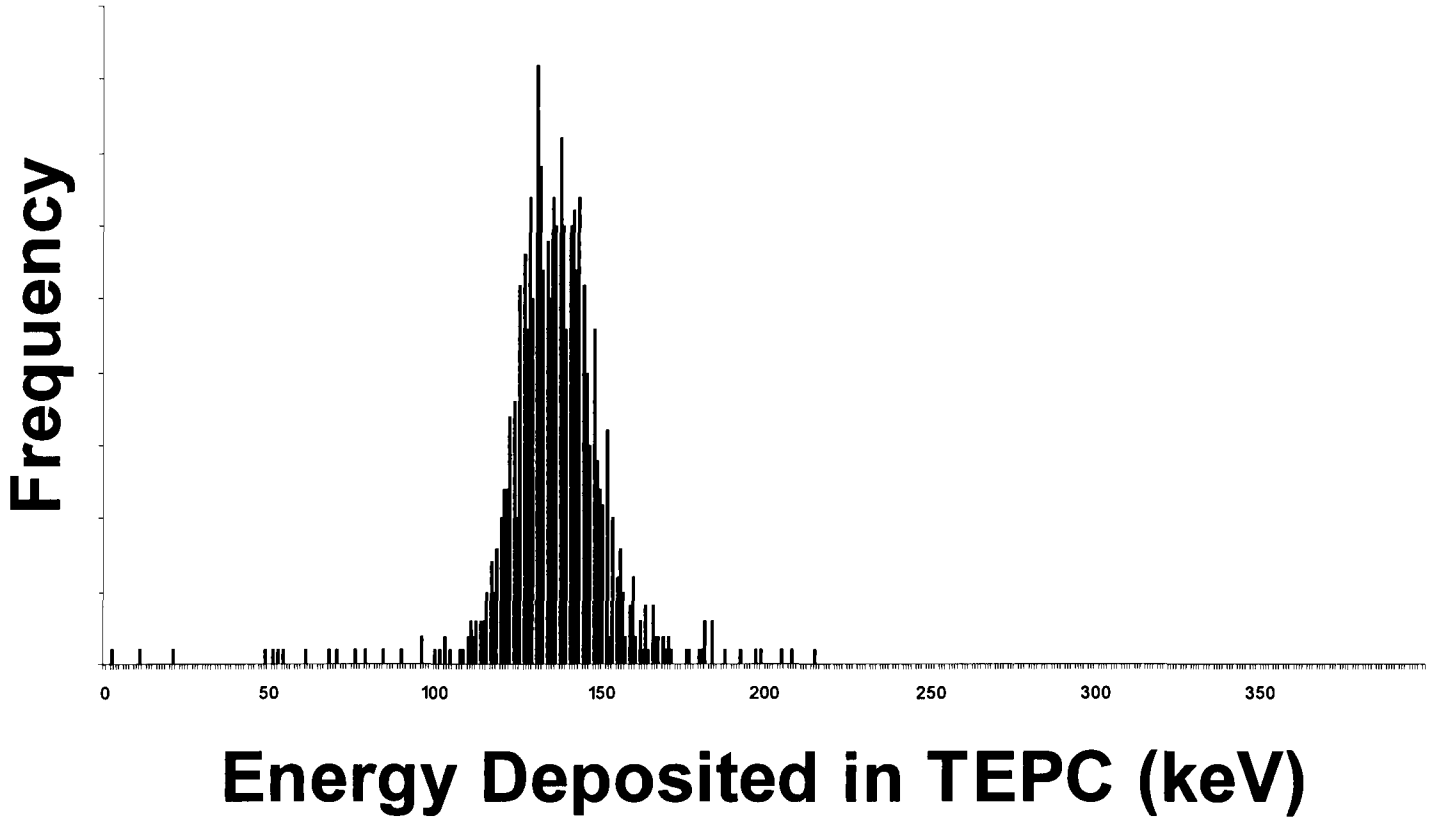

Figure G-9. Distribution of energy deposited in the TEPC by 540 MeV per nucleon Fe particles with impact parameters less than 0.5-mm.

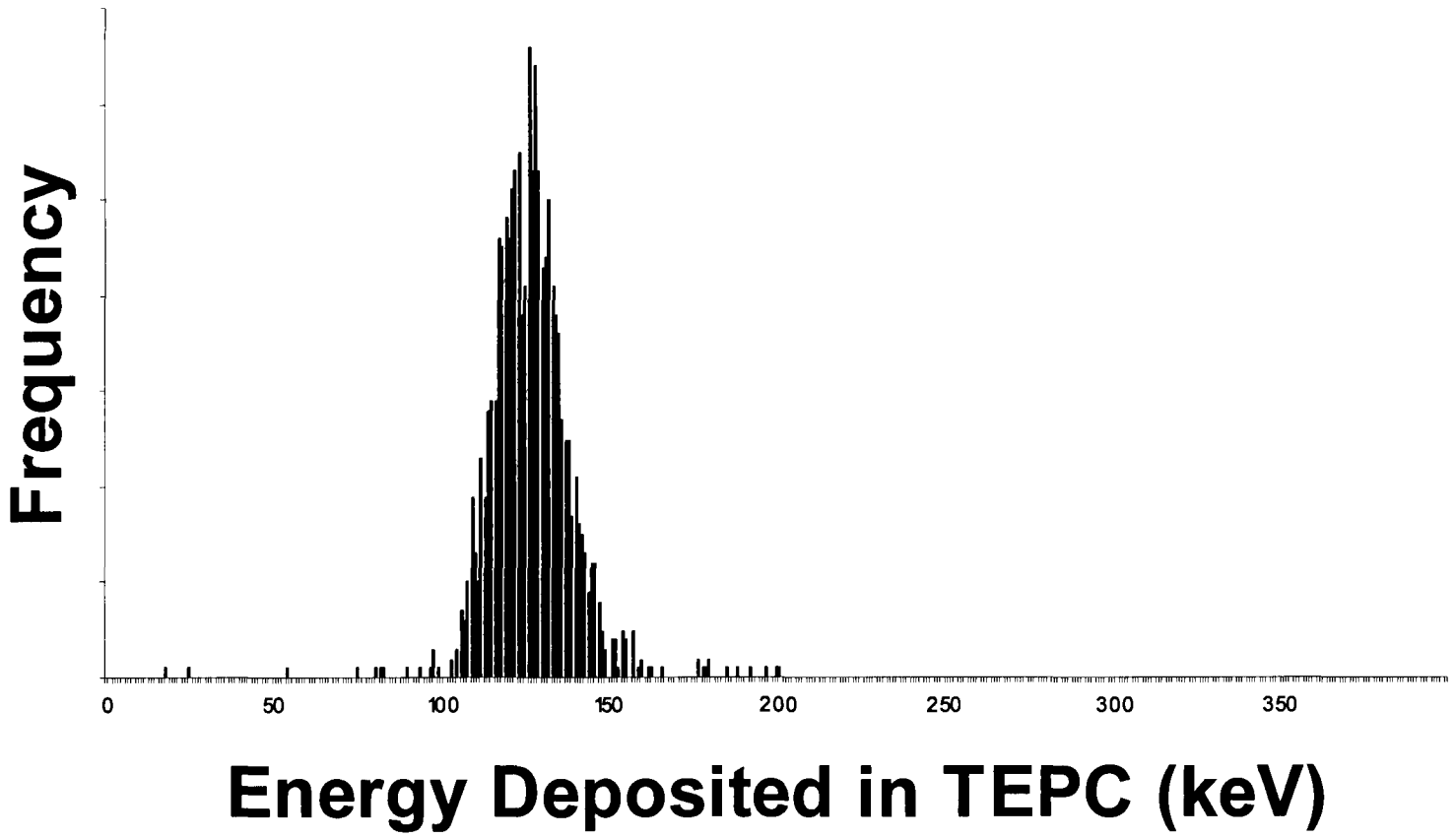

Figure G-10. Distribution of energy deposited in the TEPC by 700 MeV per nucleon Fe particles with impact parameters less than 0.5-mm.

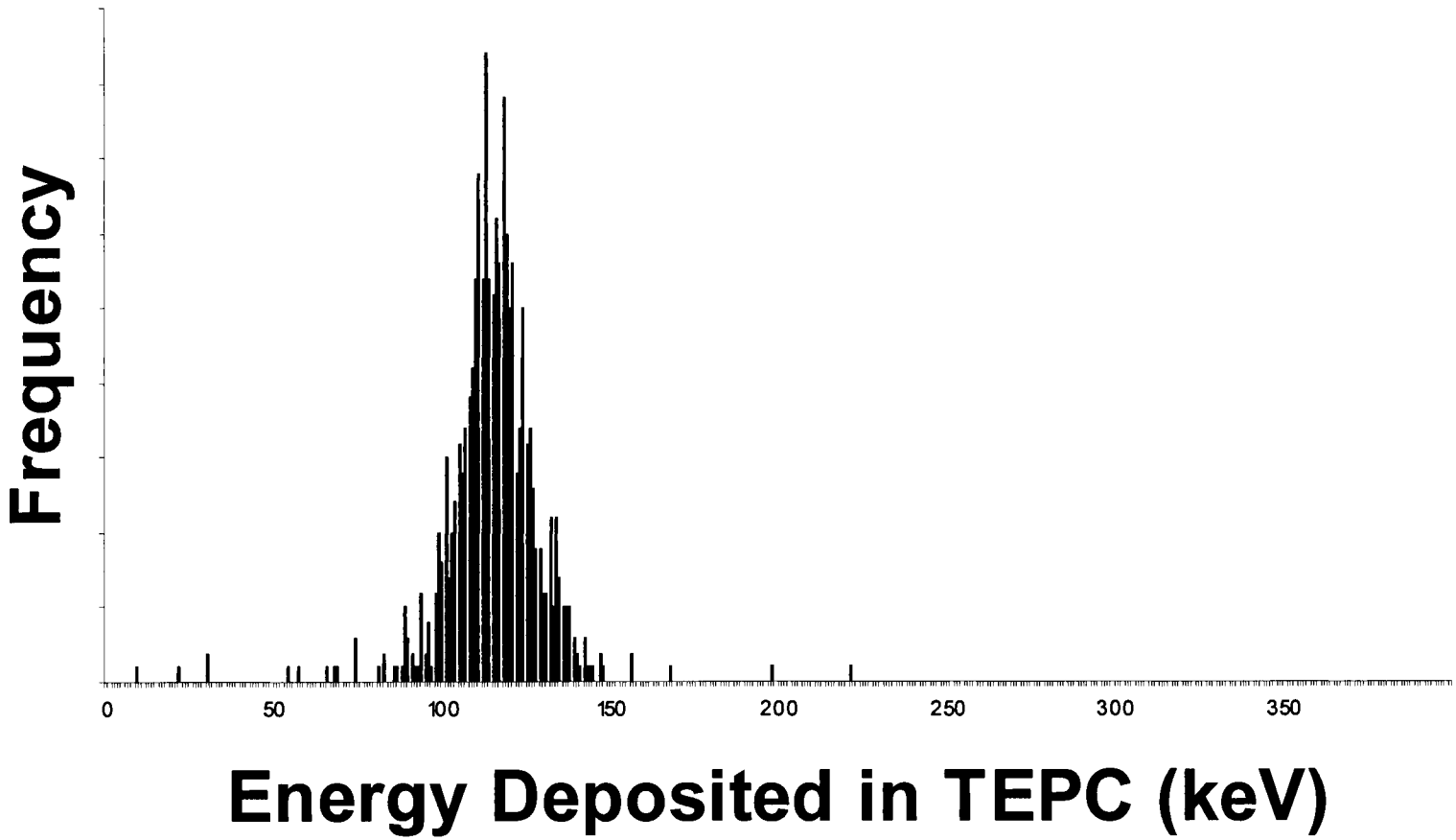

Figure G-11. Distribution of energy deposited in the TEPC by 790 MeV per nucleon Fe particles with impact parameters less than 0.5-mm.

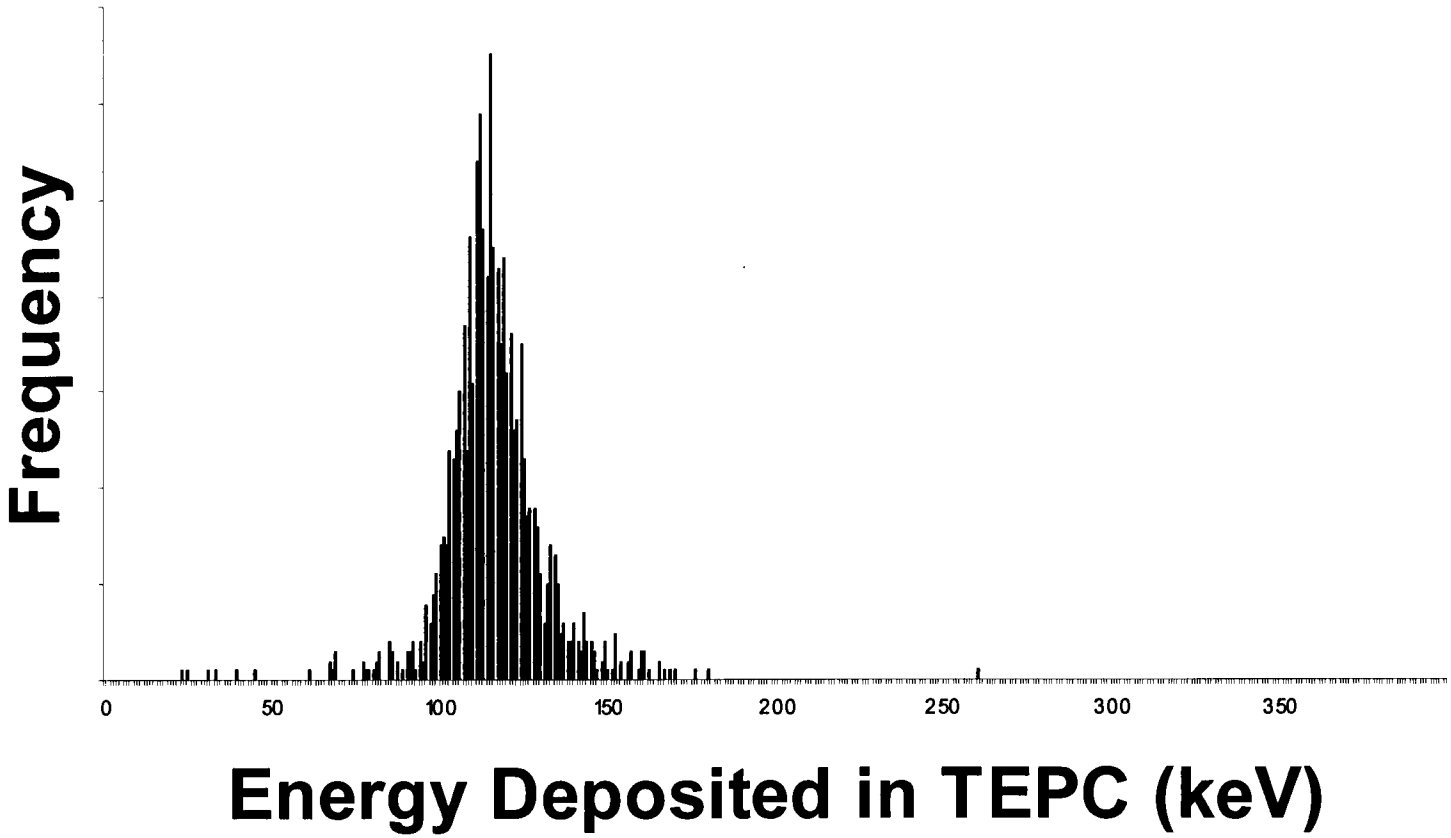

Figure G-12. Distribution of energy deposited in the TEPC by 1000 MeV per nucleon Fe particles with impact parameters less than 0.5-mm.